Dissertation zur Erlangung des Doktorgrades
der Fakultät für Chemie und Pharmazie
der Ludwig-Maximilians-Universität München

Insights into the Amine Intercalation Behavior of Layered Antimony Phosphate Thin Films and their Application in One-Dimensional Photonic Crystals

Marie Linda Däntl

aus

München, Deutschland

2022

Erklärung

Diese Dissertation wurde im Sinne von § 7 der Promotionsordnung vom 28. November 2011 von Frau Prof. Dr. Bettina V. Lotsch betreut.

Eidesstattliche Versicherung

Diese Dissertation wurde eigenständig und ohne unerlaubte Hilfe erarbeitet.

München, 14.09.2022

(Marie Däntl)

Dissertation eingereicht am:	22.09.2022
1. Gutachterin:	Prof. Dr. Bettina V. Lotsch
2. Gutachter:	Prof. Dr. Robert E. Dinnebier
Mündliche Prüfung am:	24.10.2022

„The scientist is not a person who gives the right answers, he is one who asks the right questions”

— Claude Lévi-Strauss

Danksagung

Zuallererst möchte ich mich bei meiner Doktormutter Prof. Dr. Bettina V. Lotsch für die Möglichkeit bedanken meine Dissertation auf diesem interessanten und vielversprechenden Forschungsgebiet in ihrer Arbeitsgruppe anfertigen zu dürfen, sowie für ihre Betreuung, Unterstützung in jeglicher Hinsicht, und die mir gewährte wissenschaftliche Freiheit.

Des Weiteren danke ich Prof. Dr. Robert E. Dinnebier für die Übernahme des Zweitgutachtens. Außerdem danke ich dem Rest der Prüfungskommission bestehend aus Prof. Dr. Achim Hartschuh, Prof. Dr. Emiliano Cortés, Prof. Dr. Don C. Lamb, und Prof. Dr. Philip Tinnefeld für die Bereitschaft an meiner Doktorprüfung teilzunehmen.

Bei Rotraut Merkle möchte ich mich für die externe Betreuung sowie die hilfreichen Gespräche im Rahmen der Sitzungen des Doktorandenkomitees bedanken.

Mein besonderer Dank gilt all meinen Co-Autoren, ohne die ich meine Forschungsprojekte nicht hätte realisieren können. Dabei möchte ich Dr. Alberto Jiménez-Solano für die day-to-day Betreuung, die unzähligen Diskussionen, und sein Matlab-„magic“ danken. Außerdem danke ich Hugo A. Vignolo-González und vor allem Johannes Maschita für ihre Mithilfe während der spannenden und unvergesslichen Zeit am Synchrotron. Allen voran möchte ich mich bei Dr. Sebastian Bette sowohl für die hervorragende Kollaboration beim Synchrotron Projekt als auch für zahlreichen internal Revisions sowie für das kritische Korrekturlesen dieser Arbeit herzlich bedanken. Du hast mich nicht nur mit deiner wissenschaftlichen Expertise unterstützt, sondern auch eine Mentor-Funktion für mich eingenommen.

Meinen Praktikanten Susanna Guderley und Patrick Born danke ich für ihre selbstständige und tatkräftige Unterstützung und die daraus resultierenden spannenden Ergebnisse.

Viola Duppel möchte ich für die vielen schönen SEM cross-section Bilder danken, sogar von Proben bei denen ich es nicht für möglich gehalten hätte. Des Weiteren bedanke ich mich für die organisatorische Unterstützung von Claudia Kamella und Sigrid Fuhrmann. Selbst wenn ihr mal nicht die richtigen Ansprechpartner wart, wusstet ihr immer genau an wen ich mich wenden muss und habt mir damit das Leben am Institut leichter gemacht. Für die technische Assistenz - von der Planung, über den Umbau des Gerätes bis zur tatsächlichen Umsetzung am ANKA (selbst aus der Ferne und mitten in der Nacht) - bedanke ich mich herzlich bei Dr. Peter Wochner. Es war unglaublich spannend, ich habe viel gelernt und bin dankbar, dass ich diese Erfahrung machen durfte. Für zahlreiche TOF-SiMS Messungen möchte ich mich bei

Tolga Acartürk bedanken. Willi Hölle möchte ich für die schnelle und hilfsbereite Unterstützung bei allen technischen Anliegen danken.

Außerdem möchte ich Johannes Maschita, Alexander Pütz und Willi Hölle für die freundschaftliche Atmosphäre in unserem Büro danken. Ich hätte mir keine besseren „Büro-Mitbewohner“ wünschen können! Der ganzen Arbeitsgruppe danke ich für die angenehme Arbeitsatmosphäre, die wissenschaftlichen Diskussionen, die unzähligen Kaffeepausen und Barbecues und für all die schönen Erlebnisse innerhalb und außerhalb des Institutes. Ich schätze es sehr, dass während dieser Zeit so viele gute Freundschaften entstanden sind!

Ich möchte mich natürlich auch bei allen meinen Freunden bedanken, die mich auf dem Weg zur Promotion begleitet haben und mir Rückhalt gegeben haben. Vor allem bei Charlotte Koschnick, die mir immer mit Rat und Tat zur Seite stand.

Mein größter Dank gilt jedoch meiner Familie und meinem Partner, die mich jederzeit bedingungslos unterstützt haben und mich mit gutem Essen verwöhnt haben. Danke, dass ihr immer für mich da seid!

Summary

Sensors have become an integral part of our everyday lives, and especially since the rise of the Internet of Things, it is of utmost importance to meet the ever-growing demand for smart, miniaturized sensors. In particular, finding new pathways for the non-electrical readout of sensors is in high demand, as this may play an important role in the progressive miniaturization which sensors have been undergoing in the recent past. In this regard, colorimetric sensors are a promising detection platform as they can provide label-free readout without additional wiring. They exhibit color changes in response to external stimuli, which can be detected optically (i.e. qualitatively) with the naked eye. As amine intercalation is known to alter the selectivity of colorimetric $H_3Sb_3P_2O_{14}$ nanosheet-based *Fabry-Pérot* sensors towards vapors, the main goal of this thesis was to enhance their future application in sensing devices by developing new techniques to further improve the post-synthetic rational design and fine-tuning of the properties.

One approach towards this goal was the application of a soft, post-synthetic vapor-phase amine modification to an amine-intercalated $H_3Sb_3P_2O_{14}$ thin film, which allowed continuous replacement of one intercalated amine by another one (Chapter 4). The verification of this method with a series of primary alkylamines demonstrated the exquisite control over the properties of the thin film on demand, and confirmed the reversibility of the amine exchange process. Depending on the amine used, a continuous change of the average *d*-spacing and polarity of the thin films was observed, which allows fine-tuning of the sensing properties. In addition, the amine exchange was exploited to pattern thin films by using masks of different sizes. This allowed a high degree of spatial control over the sensor properties and added a new technique to the toolbox of soft lithography-type patterning.

Another goal towards the practical application of nanosheet-based sensors is the possibility to transfer them to arbitrary substrates. For these studies (Chapter 5), 1DPC sensors, comprised of $H_3Sb_3P_2O_{14}$ nanosheets and TiO_2 nanoparticles, were chosen, because they exhibit a high stability when removed from the substrate. By intercalating *n*-octylamine either in the whole sample or in a spatially resolved manner by using a mask, the hydrophobization of the 1DPC was ensured, which acts as a protection against water during the transfer step. In combination with a water-soluble sacrificial layer, the 1DPC or patterns thereof could be detached from their original substrate in a quick and facile manner by immersing the samples in water. In a second step, the freestanding sensor which was swimming on the surface of the water could

be picked up with arbitrary substrates. By applying the amine exchange approach from Chapter 4, the sensing response of the transferred sample could be tailored. The transfer method, therefore, combines control over the sensor and substrate shapes with control over the selectivity of the sensor, providing a versatile platform for adaptable sensors.

Although the projects discussed in Chapters 4 and 5 illuminated the numerous possibilities of amine intercalation and exchange for the custom design of nanosheet-based sensors, the intercalation process has not yet been fundamentally understood. With respect to the future application of amine intercalation and exchange to other layered systems, a deeper understanding of the mechanisms should facilitate the development of novel sensors. Peak broadening and shifting in *in situ* X-ray diffraction (XRD) patterns are commonly observed phenomena when studying the intercalation of a guest species into a layered host. Chapter 6 introduces a novel approach to quantitatively analyze changes in the peak profile and peak position during the intercalation of *n*-butylamine (3M in ethanol) in the $H_3Sb_3P_2O_{14}$ thin film. The applied method includes a state-of-the-art recursive supercell approach that accounts for peak broadening and shifting, which is caused by randomly occurring intercalation of solvent, amine, or solvent-amine double intercalation. This enabled quantitative Rietveld refinements for the collected XRD patterns and elucidation of the kinetics of the amine uptake and the formation of intermediates. Since ethanol is never fully removed from the material, the intercalation of ethanol and amine appears to be a competing process.

In summary, this thesis explored the use of amine intercalation in $H_3Sb_3P_2O_{14}$-based photonic devices to lay the groundwork for future practical applications in the field of miniaturized vapor sensors, with a focus on increasing the adaptability and versatility of the sensors.

Table of Contents

1 Introduction Thin Films

Sensors have become an indispensable part of our everyday lives. Applications range from autonomous car parking[1] over clinical diagnosis[2] and food packaging[3] to domestic air conditioning.[4] Various measuring methods are available to determine response to physical or chemical stimuli, with humidity being one of the most commonly measured stimuli.[5] So far, various sensing methods based on capacitance or resistance have been explored. However, it is of utmost importance to meet the ever-growing demand for smart, miniaturized sensors by finding new pathways for the electricity-free readout of sensors. Therefore, the work carried out in this thesis aims to pave the way for the application of adaptable colorimetric sensors based on structural color for gas and vapor sensing. To this end, the property tuning of nanosheet-based *Fabry-Pérot* interference thin films as well as nanosheet-based one-dimensional photonic crystals (1DPCs) was investigated. In both cases, antimony phosphate nanosheets were used as a highly responsive sensing component.

In order to give sufficient background information, the introduction is divided into two main parts. Chapter 1 focuses on the use of nanosheets in *Fabry-Pérot* interference thin film sensors, while Chapter 2 is an invited review article about stimuli-responsive 1DPCs. Regarding Chapter 1, the following subsections describe state of the art solvent-based exfoliation methods for obtaining nanosheets, approaches for tailoring their properties and their application in gas and vapor sensors. Particularly, the focus lies on the application of antimony phosphate nanosheets as *Fabry-Pérot* sensors for various vapors, considering the theoretical principles of a nanosheet-based *Fabry-Pérot* sensor and the fabrication methods.

1.1 Exfoliation of Layered Materials into Nanosheets

Nanosheets (also termed 2D materials) are crystalline materials, which can be obtained through exfoliation of layered bulk material by overcoming the weak van der Waals or ionic interlayer forces. In vertical dimension, they consist of a single layer of atoms and exhibit lateral dimensions of several hundred nanometers to microns. The first known 2D material was graphene, which Wallace[6] studied theoretically in 1947 and Boehm[7] and co-workers isolated experimentally in 1962. After Geim and Novoselov[8] experimentally discovered the exceptional electronic properties of graphene in 2004, an upsurge of research interest towards the properties and applications of graphene was sparked. Interestingly, graphene features excellent mechanical, thermal and optical properties, which are significantly different compared to their

bulk counterpart.[9-11] This is assigned to the inherent high surface area-to-volume ratio, which drastically increases the importance of surface states and the quantum size effects that arise from the dimensional confinement.[12] Following this revolutionary discovery, research interests turned to other classes of 2D materials with a broad chemical variety, opening the possibility of new applications as nanodevices[13] or hybrid artificial solids.[14,15]

To date, many different possibilities for the fabrication of nanosheets have been explored, ranging from bottom-up techniques such as expensive vapor growth methods[16,17], or synthesis from molecular precursors[18] to the top-down approach of exfoliation[19] of layered materials. Exfoliation is defined as the decomposition of the bulk material into single to few layer nanosheets. If the exfoliation leads to a complete separation of the individual layers of the bulk material, this process is termed delamination.[20] However, delamination depends on the nature (van der Waals or ionic) and strength of the interlayer interaction of the bulk material and hence, different chemical and physical procedures may need to be applied. Exfoliation methods can be divided into mechanical exfoliation such as the application of scotch tape or cleavage through rubbing a layered crystalline material on another surface,[8] and solvent-assisted approaches, which include redox-mediated delamination,[21] ion exchange[22] and agitation-assisted liquid phase exfoliation.[23]

Mechanical exfoliation has been applied for several materials including graphene[9] and inorganic van der Waals solids like MoS_2.[24] Although mechanical exfoliation is a very straightforward method, the scalability is limited and the main product consists of multilayered flakes, while single layered nanosheets are in the minority. Solvent-mediated exfoliation methods, on the other hand, are considered promising for commercial application as they provide high yields of single layered nanosheets, are inexpensive and scalable, and have high compatibility with current processing technologies like spin-coating or inkjet-printing.[25,26] Therefore, solvent-mediated exfoliation approaches, including redox-mediated delamination, ion exchange, and agitation-assisted liquid phase exfoliation, will be discussed in detail below.

The most straightforward solvent-mediated exfoliation approach is the liquid phase technique based on agitation-assisted exfoliation, which can be applied for van der Waals[23,27] and ionic layered materials[28] likewise. For exfoliation, the interlayer interactions between the layers of the bulk material need to be overcome by imparting energy.[29] To do so, the bulk material is immersed in an appropriate solvent depending on the surface tension as well as the chemical properties of the material. During the exfoliation process, the solvent molecules interact with

the layers at the liquid-nanosheet interface and intercalate in-between the layers of the bulk material, which leads to a swelling and thus weakened interlayer interactions. Agitation, such as sonication, stirring, or shaking, pries the layers apart, resulting in a nanosheet suspension (Fig. 1.1). Specifically, the solvent minimizes the net energetic cost of the exfoliation and additionally adsorbs to the nanosheet surface, which stabilizes them against reaggregation in the liquid.[29]

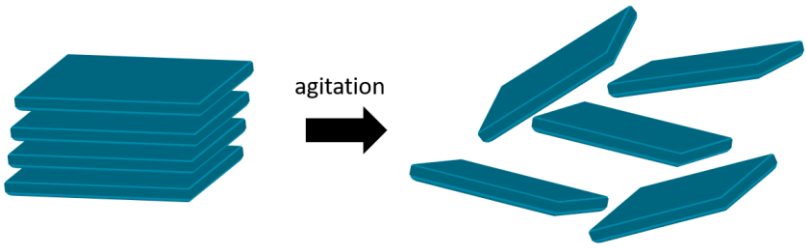

Fig. 1.1 Schematic description of the agitation-assisted exfoliation route. When the layered material is immersed in an appropriate solvent, it intercalates in between the layers, thereby weakening the attractive forces, and subsequent agitation delaminates the material.

For example, the lithium tin sulfide $Li_2Sn_2S_5$ phase can be exfoliated by stirring in pure water, which is also relevant for the work conducted in this thesis.[28,30] The main advantage of the agitation-assisted method is its inexpensiveness and the high throughput.[20] However, this method does not only yield single layer nanosheets but also non-exfoliated material and multilayer flakes. In order to separate the few to single layer nanosheets from the non-exfoliated material, several centrifugation steps are needed, which strongly influences the lateral size of the nanosheets.[29] Similar to the previously discussed methods, the addition of surfactants or polymers may be needed to prevent agglomeration.[31]

Layered materials, which are only held together by attractive van der Waals forces between the adjacent layers are often delaminated with the redox-mediated approach (Fig. 1.2).[20] In this case, treatment of the material with a reducing or oxidizing agent leads to a change in oxidation state and therefore modifies the properties of the interlayer gallery. Subsequent agitation, such as sonication, enables the exfoliation.

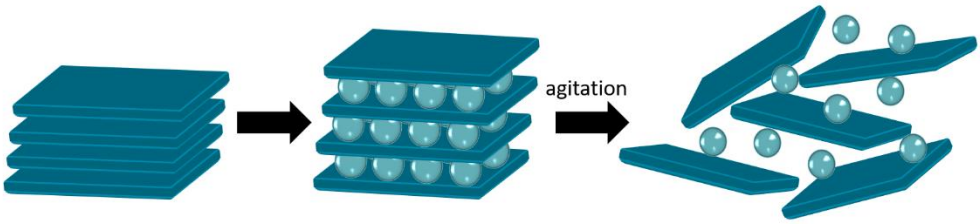

Fig. 1.2 Schematic description of the redox-mediated exfoliation approach. The layers are depicted in cyan, while the oxidizing or reducing agent is given as turquoise spheres. By treating the layered material with an oxidizing or reducing agent, the properties of the interlayer space are modified, and the following agitation enables the delamination of the layered material.

For example, transition metal dichalchogenides (TMDs) such as MoS_2, amongst others, can be exfoliated by intercalation of lithium, either by treating the bulk material with *n*-BuLi in hexane[21,32] or electrochemical intercalation.[33] After sonication in water, this procedure yields mainly single layer nanosheets with large lateral size. It is supposed that the reaction of the lithium-intercalated bulk material with water forms lithium hydroxide and H_2 gas. The evolution of H_2 gas between the layers breaks up the stacking and leads to a separation of the layers.[34] Furthermore, repulsive forces in the layered bulk material can be introduced, e.g. by the oxidation of graphite to graphene oxide, which enables its exfoliation in covalently modified negatively charged nanosheets in water.[11,35] However, the downside of the redox-mediated method is that the obtained nanosheets often need to be stabilized in suspension by electrostatic forces[36] or surfactants[21] to prevent agglomeration.

Ionic layered materials, which are comprised of negatively or positively charged layers along with charge compensating ions situated in the interlayer gallery, are commonly exfoliated with the ion-exchange method.[37,38] In a first step, soft chemical methods are applied to replace the interlayer ions with other, larger ions. This leads to an increased interlayer distance and therefore the attractive electrostatic forces in the material are weakened. In some cases, the addition of bulky intercalants, such as tetra(*n*-butyl)ammonium hydroxide (TBA^+OH^-) or tetramethylammonium hydroxide (TMA^+OH^-), may be needed to further weaken the attractive forces.[37,39] In the second step, mechanical force is introduced by stirring or shaking, which leads to an exfoliation into single to few layered nanosheets (Fig. 1.3). The driving force of the delamination is the hydration of the charge compensating ions that are situated in the interlayer gallery.

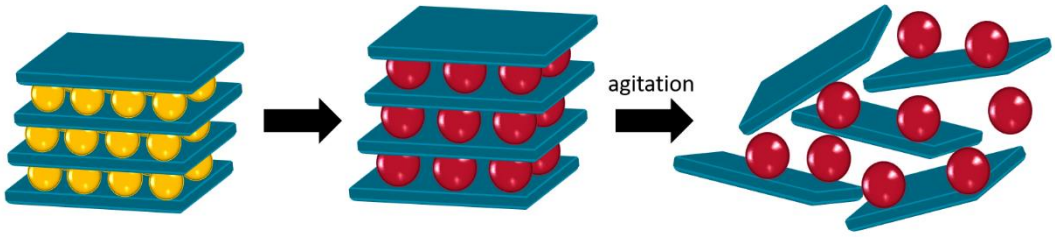

Fig. 1.3 Schematic description of the ion-exchange exfoliation process. The layers are depicted in cyan, while the counterions of the charged layered material are given as yellow spheres. The ions with which the pristine counterions are replaced are shown as red spheres. The replacement of the counterions with other, larger counterions reduces the interlayer interactions, and subsequent agitation leads to exfoliation of the layered material.

For example, the transition metal oxide $KCa_2Nb_3O_{10}$ has been exfoliated by cation-proton exchange by treating the bulk material with an acid solution and subsequent delamination with TBAOH.[40] Due to the Brønsted solid acidity of the proton-exchanged bulk material, the protons in the interlayer gallery can be exchanged with TBA^+ (in an aqueous solution), whereby an acid-base reaction between the protonated (acidic) layered material and the basic alkylammonium solution takes place. This in turn leads to the increased inflow of water molecules, which causes swelling and therefore reduction of the attractive forces between the nanosheet layers.[38] By applying a shearing force it is possible to exfoliate the swollen material. Further, it was discovered that the cation-proton exchange of $K_3Sb_3P_2O_{14}$ in HNO_3 results in the phosphatoantimonic acid $H_3Sb_3P_2O_{14}$, which spontaneously exfoliates under stirring in water due to the pronounced swelling upon water uptake.[41] This is particularly relevant for the work conducted in this thesis. Please note that an in depth discussion of the properties of the antimony phosphate can be found in Section 1.6. Even though the yield of single layer nanosheets is high when using the ion-exchange approach, the downside is that the time needed for sufficient exfoliation is much higher than for other exfoliation methods.[20] Moreover, if surfactants or alkylammonium salts are used for the facilitation of the exfoliation, they may alter the properties of the resulting nanosheets compared to those of the pristine bulk material since they mostly cannot be removed completely after the exfoliation process.[42]

1.2 Tailoring the Properties of Nanosheets

2D materials in their pristine form are described with many superlatives already, but in order to fully exploit their novel properties and customize them towards specific applications, it is highly desirable to tailor the physical and chemical properties of the nanosheets.[43] This can be achieved by common functionalization methods (Fig. 1.4), which include morphology

control,[44,45] elemental substitution,[46] intercalation and ion exchange,[47] nanoparticle (NP) decoration[48] as well as covalent modification.[49,50]

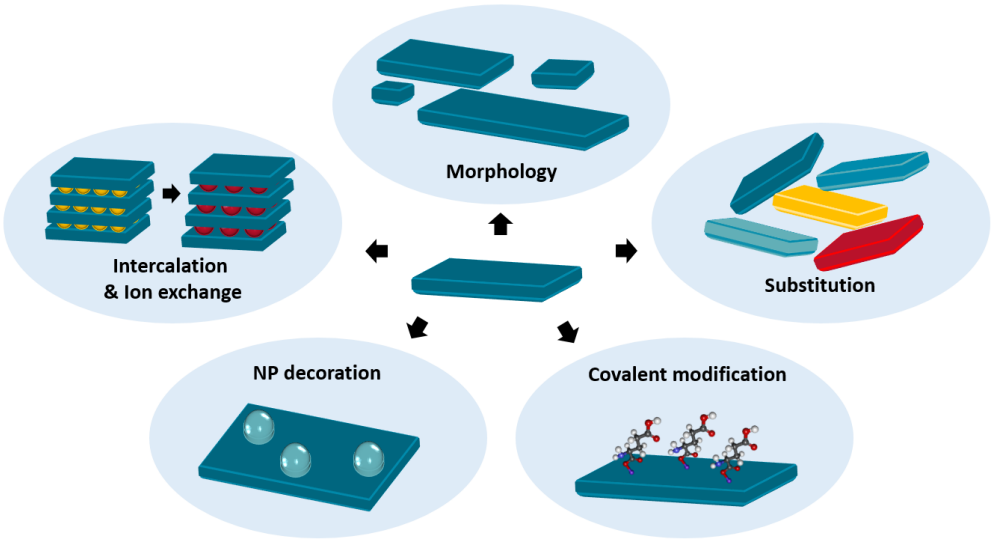

Fig. 1.4 Schematic description of the possibilities for tailoring of the nanosheet properties including morphology control, elemental substitution, covalent modification, NP decoration, as well as intercalation and ion exchange. The figure was redrawn and adapted from reference 51.

Ion exchange and intercalation are highly efficient methods for tuning the properties of layered bulk materials[52] or imparting them with new properties, but research interest was directed towards applying these methods to 2D materials only recently.[47] Since these methods comprise the central part of the work conducted in this thesis, the following discussion will focus solely on this aspect of property tuning in nanosheets. So far previous work was focused on tailoring the optical,[53] mechanical,[54] or electronic[55] properties amongst others by intercalation of different guest species. Most intercalation strategies are based either on electrochemical intercalation[56,57] or soft chemical intercalation *via* the liquid or the vapor phase.[53,58] In comparison to electrochemical intercalation, the soft chemical approach offers only a very limited control over the degree of intercalation.[47] On the other hand, electrochemical intercalation allows the usage of fewer guest and host materials, while chemical intercalation is applicable for a large library of materials.[47] Nevertheless, both methods are suitable for judiciously designing and fine-tuning the properties of nanosheet-based structures.

Recent publications have demonstrated that intercalation of guest species in nanosheet-based vapor sensors can be utilized to achieve a clear enhancement of the sensing performance. For example, TiO_2 nanoparticle intercalation in reduced graphene oxide (RGO) improved the sensitivity of the sensor towards NO_2 by over 400% compared to the pristine RGO sensor.

This is due to the fact that the TiO_2 acts as a nanospacer, which leads to more available surface area of the RGO sensor and therefore more active adsorption sites for the analyte.[59] Moreover, the intercalation of guest species cannot only be applied for enhanced sensitivity, but it can also be used to tune the sensing properties, e.g. the sensitivity towards certain analytes, which has been demonstrated by Koh and co-workers. They studied the gas-induced interlayer swelling of $Ti_3C_2T_x$ MXene (T represents surface termination (–O, –OH, and/or –F)) thin films and its influence on the gas sensing performance. Furthermore, they showed that the gas selectivity can be tuned by controlling the molecular intercalation behavior *via* metal ion intercalation. This is essential for enhancing the selective sensing of gas molecules.[60] As these examples underline that 2D materials are promising candidates for gas and vapor sensing applications and it is important background knowledge for the work conducted in this thesis, the next chapter will give more insights on this topic.

1.3 Nanosheets in Gas and Vapor Sensing Applications

Most of the nanosheet-based vapor sensors studied in literature rely on electronic changes (resistivity or conductivity) in the sample upon exposure to the analyte. Thereby, a charge transfer process occurs between the sensing material and the adsorbed gas molecules, and hence changes in the electrical properties are induced in the sample and can be measured. So far, many examples and readout schemes exist, whereby the main interest is focused on chemiresistors and field effect transistors (FETs), while the research field regarding photonic sensors is much smaller.[61,62] For example, in chemiresistors the resistivity is changed upon exposure to gaseous analytes such as water vapor (humidity),[63,64] triethylamine,[65] volatile organic compounds (VOCs),[66] methane,[67] or ammonia,[68] whereby typically applied materials include (functionalized) MoS_2, VS_2, BN, or GO.

In FET-based sensors the drain current, which flows from the source towards the drain, is modified upon interaction with the analyte and therefore functions as the sensing signal. Often MoS_2 or graphene is used as sensing component, and this type of sensor can be applied for environmental monitoring of ethanol,[69] NO_2[70] or H_2O_2.[71] Both of these sensor types exhibit high sensitivity, a low limit of detection, and the possibility for miniaturization, which makes them important candidates for wearables or medical diagnostics.[65,72] However, the disadvantages are slow response and recovery times as well as limited selectivity and lifetime.[61,73] Another downside of this approach is the complicated fabrication of the sensor and the need for a readout device. Hence, colorimetric sensors, such as interference based

Fabry-Pérot thin film sensors that can be fabricated in a facile manner and are read out with the naked eye or a commercially available webcam, are in high demand for future applications.

Compared to sensors, which operate with electronic changes as response to a stimulus, optical nanosheet-based *Fabry-Pérot* vapor sensors have clear advantages. Since they rely on film thickness changes during the sensing event, the used materials do not need to be conductive.[74] Furthermore, they do not require a power supply or a sophisticated readout mechanism and they provide fast response and recovery times.[74,75] For example, $H_3Sb_3P_2O_{14}$ nanosheet-based *Fabry-Pérot* devices have been utilized for sensing humidity and VOCs, showing changes in structural color as response to the stimulus due to their tremendous swelling capability upon intercalation.[76,77] Since this type of sensor was used in this thesis, the details on the working principle of a nanosheet-based *Fabry-Pérot* interference sensor are given in the following section.

1.4 Working Principle of Nanosheet-based Fabry-Pérot Interference Sensors

Fig. 1.5a depicts the condition for constructive interference under normal incidence of a *Fabry-Pérot* sensor, which is mathematically described as a combination of Bragg's and Snell's law (Eq. 1.1).

$$m\lambda = 2n_{eff}l \qquad \text{(Eq. 1.1)}$$

With m being the order of diffraction, λ the wavelength for constructive interference, n_{eff} the effective refractive index (RI), and l the layer thickness. From Eq. 1.1 it can be derived that a change in the optical thickness (product of layer thickness and RI) as response to external stimuli results in a change in the condition for constructive interference and therefore the color of the sensor. For a detailed discussion on the effects of the sensing event (thickness or RI change), please refer to Section 2.5. Since layered materials exhibit enormous swelling capabilities, nanosheet-based *Fabry-Pérot* sensors with a preferred orientation of the sheets parallel to the substrate are especially favorable. Materials that have been applied as stimuli-responsive thin films include $H_3Sb_3P_2O_{14}$,[58] $TBA_xH_{3-x}Sb_3P_2O_{14}$[77] and $TBA_xH_{1-x}TaP_2O_8$.[76] A schematic representation of such a nanosheet-based *Fabry-Pérot* device is given in Fig. 1.5d.

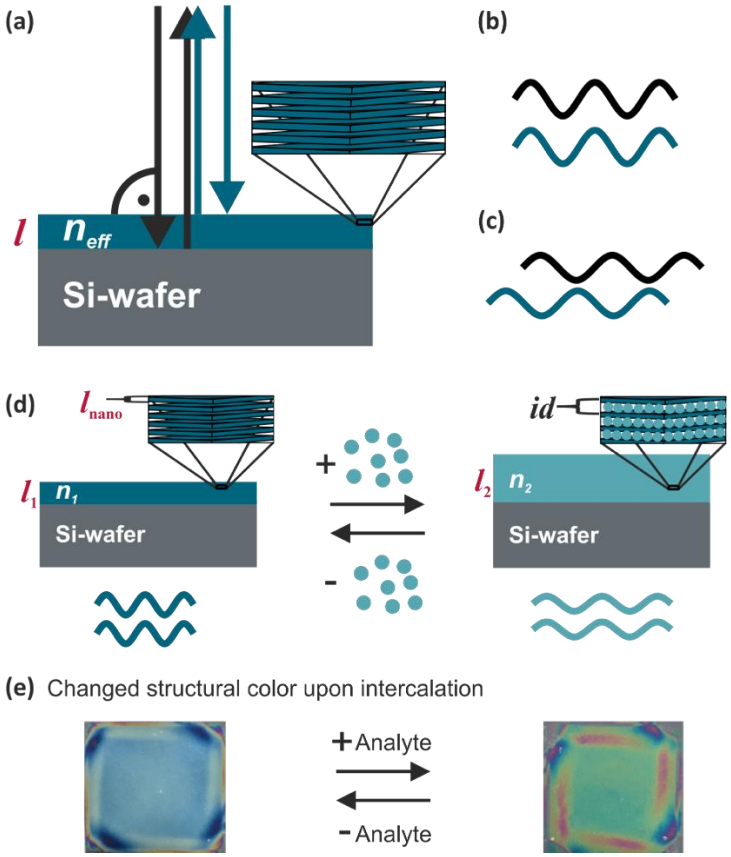

Fig. 1.5 (a) Schematic illustration of a nanosheet-based *Fabry-Pérot* photonic sensor under normal incidence. (b) Representation of the constructive interference of the outgoing beams for a wavelength λ_1. (c) Representation of the destructive interference of the outgoing beams for a wavelength λ_2. (d) Description of the sensing principle of a nanosheet-based *Fabry-Pérot* device. The layers of the thin film are depicted in cyan and the analyte is given in turquoise. (e) Photographs of the changed structural color upon intercalation with an analyte. The figure was redrawn and adapted from reference 77. n = refractive index, l = layer thickness, l_{nano} = thickness of a single nanosheet, and id = interlayer distance.

The total layer thickness l of the thin film device is characterized in Eq. 1.2, whereby k is the number of nanosheet layers stacked horizontally on the substrate, l_{nano} describes the thickness of a single nanosheet, and id stands for the interlayer distance.

$$l = k \cdot (l_{\text{nano}} + id) - id \qquad \text{(Eq. 1.2)}$$

Intercalation of an analyte in the interlayer space of the sensing material or ion exchange leads to an altered interlayer distance, which results in a changed overall film thickness l, resulting in a color change of the thin film, as described in Eq. 1.2 and Fig. 1.5d. Therefore, a sensing event can be detected through the change of the structural color (Fig. 1.5e) by the naked eye or a camera.

1.5 Fabrication Methods of Nanosheet-based Fabry-Pérot Sensors

In order to fabricate thin films with tailor-made properties, solution processed fabrication techniques are often the method of choice. Some common fabrication methods include spin- and dip-coating. Please note that the topic will not be discussed in depth here as a detailed description and schematic figure of both methods can be found in Section 2.3. Instead of alternately fabricating layers of two different materials (as it is done for 1DPCs), the thin film formation includes solely the deposition of one stable colloidal suspension. Similar to 1DPCs, when spin-coating is applied for the fabrication of thin films, the obtained film thickness can be influenced by variation of the acceleration speed, final rotation speed, concentration of the suspension, as well as the number of applied deposition steps. In the latter case, the deposition steps can be performed directly after each other, but more homogeneous results are achieved when an intermittent heating step is applied in order to remove the residual solvent from the sample. In this thesis, the $H_3Sb_3P_2O_{14}$ thin films were fabricated with the spin-coating technique.[77] The nanosheets were dispersed in an ethanol/water mixture with a ratio of 60:40 vol-% in order to ensure the fast evaporation of the solvent (ethanol) during the spinning and at the same time enable the sufficient exfoliation and stabilization (water) of the nanosheets in suspension.[78] During the spinning, the nanosheets order themselves out on the substrate, leading to a preferred stacking of the sheets parallel to the substrate and a random orientation, i.e. turbostratic disorder, of the sheets within the stack.[76]

To give a foundation for the better understanding of the $H_3Sb_3P_2O_{14}$-based thin films and 1DPCs used in this thesis, the next section will give a brief overview of the development of the material from past to present.

1.6 The Phosphatoantimonic Acid $H_3Sb_3P_2O_{14}$

In the late 1950s research in the field of layered metal phosphates experienced an upsurge as their use as cation exchangers for radioactive waste treatment was discovered.[79] However, they were only available as amorphous gels until the first crystalline material $H_2Zr(PO_4)_2$ was synthesized by Clearfield and co-workers in 1964.[80] They found that the compound can be applied for anion-exchange. A few years later, in 1966, Winkler and Thilo reported several layered structures similar to the zirconium phosphate and studied the ion-exchange properties of $HAsP_2O_8$ and $HSbP_2O_8$ amongst others.[81] Piffard and co-workers further investigated the structures and properties of $HSbP_2O_8$ along with several other metal(V) phosphates in the 1980s.[82-87] After the successful delamination of $H_2Zr(PO_4)_2$ in 1985,[88,89] research interest was

directed towards the exfoliation of other metal phosphates such as $HSbP_2O_8$ and $H_3Sb_3P_2O_{14}$.[41,90] Decades later, these nanosheets were applied as sensing component in optical vapor and humidity sensors.[58,76,77] Since $H_3Sb_3P_2O_{14}$ is the main material studied in this thesis, the following section will give insights into this material, especially regarding its chemical structure and the sensing characteristics that have been explored so far.

The layered potassium phosphatoantimonate $K_nSb_nP_2O_{5+3n}$ with $n = 1$, 3 are synthesized *via* solid state reactions from Sb_2O_3, $NH_4H_2PO_4$ and KNO_3.[86,87] In the case of $n = 3$, the compound crystallizes in the trigonal space group $R\bar{3}m$ (166) and the structure is built from $Sb_3P_2O_{14}^{3-}$ layers with K^+ ions in the interlayer gallery.[86]

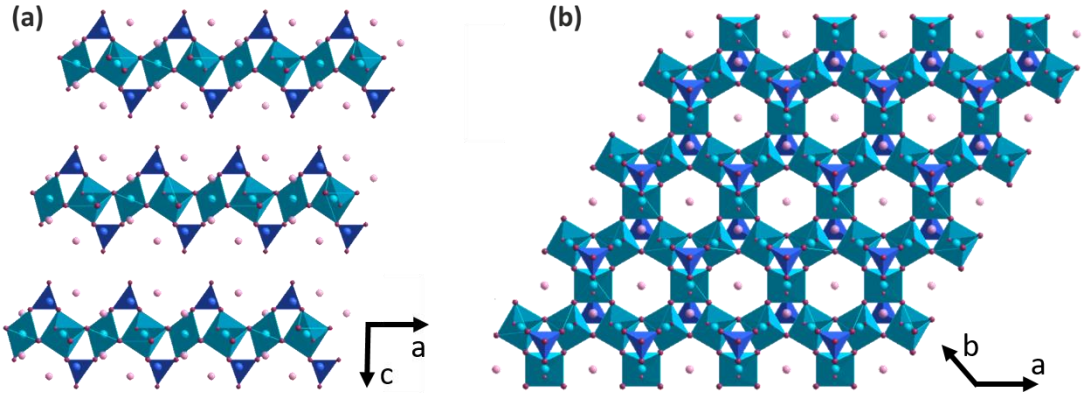

Fig. 1.6 Crystal structure of $K_3Sb_3P_2O_{14}$ along the (a) [010] and (b) [001] direction. K atoms are given in rose, Sb atoms in turquoise, P atoms in blue, and O atoms in plum. Note that for a better overview along [001] only one layer is depicted. The figure was reproduced from reference 91.

As depicted in Fig. 1.6, the layers are comprised of SbO_6 octahedra, which are each linked with four other SbO_6 octahedra.[86] Additionally, three SbO_6 units are connected over corner sharing PO_4 tetrahedra, whereby one of the phosphate ion related oxygens is situated on apical position.[92] $K_3Sb_3P_2O_{14}$ has the ability to intercalate water in between the layers, which leads to an increased interlayer distance.[93] Since the interlayer bonding is rather weak, the layers can be shifted relative to each other and the cations in the interlayer gallery can be exchanged.[94] By replacing the potassium ions with protons through ion-exchange, the phosphatoantimonic acid $H_3Sb_3P_2O_{14}$ is received.[94] In the presence of water, this compound exhibits large swelling capabilities and can easily be delaminated into intact 2D nanosheets by agitation since the weak interlayer bonding is reduced as it can be seen in Fig. 1.7.

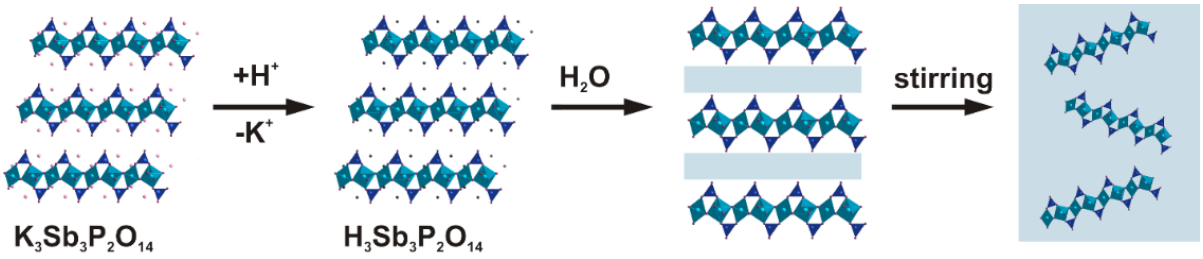

Fig. 1.7 Schematic description if the ion-exchange reaction in the layered antimony phosphates. Immersion of the material in water leads to swelling and subsequent complete delamination under agitation. The figure was reproduced from reference 91.

Furthermore, adding a soluble salt to the suspensions increases their ionic strength and therefore leads to flocculation. The addition of TBA^+OH^- enables a stabilization of the nanosheets against flocculation over a wide pH range.[41] Due to these interesting properties, versatile applications of this material in fuel cells (to increase ion conductivity)[95,96] and humidity sensors[76,77,97] have been realized.

Regarding the application of $H_3Sb_3P_2O_{14}$ nanosheets in humidity sensors, studies on the influence of relative humidity (RH) on the *c* lattice parameters (stacking distance) of the layered bulk phosphoantimonates have paved the way.[85] Compared to the potassium compounds, the capability of water intercalation driven by ambient RH changes is much larger and $H_3Sb_3P_2O_{14} \cdot x\ H_2O$ bulk material exhibits the behavior of defined hydration states.[85] Moreover, ellipsometry measurements gave a better understanding that nanosheet-based thin films of the antimony phosphate exhibit a smoother and less stepwise swelling than the layered bulk material upon exposure towards RH, which is highly desirable for sensing applications.[97] The reason for the smoother swelling is most likely the smaller domain size compared to the bulk, which enables an increased grain boundary absorption and the turbostratic disorder, which leads to less defined absorption sites between the sheets and therefore a more continuous water uptake.[97] For further details please refer to Section 2.7.3.

As mentioned before, the properties of the antimony phosphate thin films can be influenced by ion-exchange or intercalation. Therefore, the selection of appropriate species for intercalation allows for tailoring of the sensing properties in a rational manner. For example, it has been shown that the properties of the sensor can be modified by intercalation of primary and tertiary alkylamines over the vapor phase. Thereby, the amines are protonated to ammonium ions and are trapped between the negatively charged layers of the antimony phosphate ($H_{3-x}(NH_3(CH_2)_{n-1}CH_3)_xSb_3P_2O_{14}$), as indicated in Fig. 1.8. The interlayer distance

is enlarged and the structural color of the sensor is changed in dependence of the amine chain length, which leads to the possibility of using the thin film sensor to detect and distinguish different amines.[58]

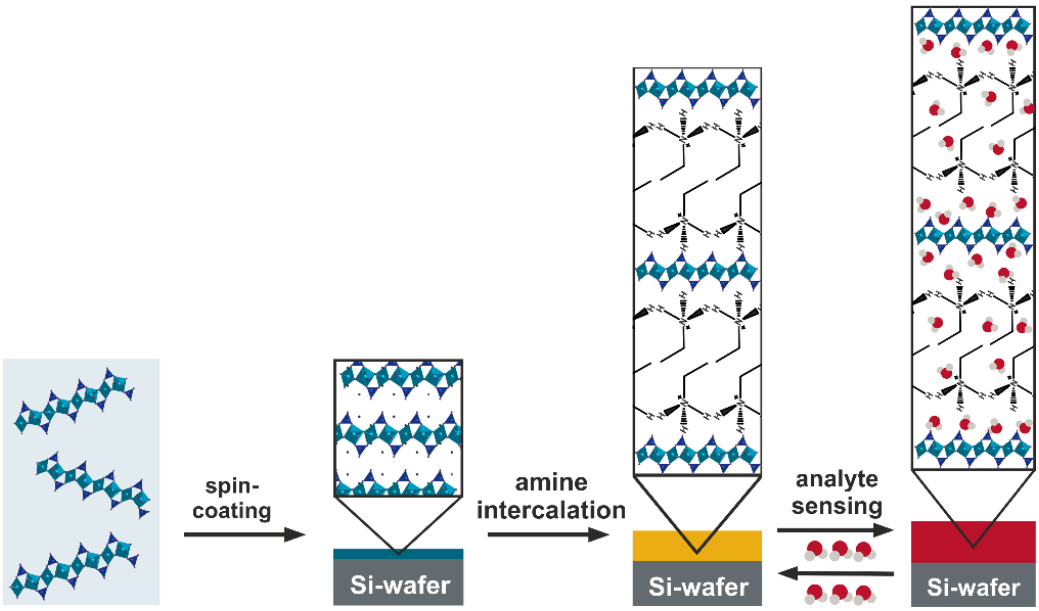

Fig. 1.8 Schematic description of the formation of a $H_3Sb_3P_2O_{14}$ thin film from the nanosheet suspension, the intercalation of ethylamine in between the nanosheets by protonation, and analyte sensing upon exposure towards humidity. The figure was reproduced from reference 91.

Moreover, the intercalated amines imbue the sensor with hydrophilic or hydrophobic properties. Therefore, it is not only possible to detect amines but these amine-intercalated $H_3Sb_3P_2O_{14}$ thin films can themselves be employed as sensors for e.g. humidity, VOCs, or alcohols. The sensing properties are tuned over a wide range as a function of the used amine and therefore the type of analyte the sensor is responsive to can be altered to meet the users' criteria. By utilizing the amine intercalation in combination with a mask, a single-chip array sensor can be fabricated, which shows a characteristic color pattern for each detected vapor.[58]

Even though there are various application possibilities for nanosheet-based thin films and the sensing performance is promising, it is desirable to further increase the versatility of these functional materials. This can be achieved by incorporating them into one-dimensional photonic crystals, which are comprised of alternating layers of two materials with different dielectric constants. A clear advantage of this architecture is that the properties of both materials can be exploited, which enables a broader range for tuning the sensors' properties and therefore makes 1DPCs more versatile than thin films. Additionally, compared to *Fabry-Pérot* thin films, 1DPCs can easily be fabricated on glass substrates and therefore they may be

applied as functional coatings, e.g. as smart coating for privacy glass windows.[98] Furthermore, the obtained reflectance exhibits a sharper signal compared to thin films and it is possible to integrate defect layers to create optical resonators, which results in enhanced sensitivity and facilitated readout. Due to the extraordinary sensing properties of $H_3Sb_3P_2O_{14}$ nanosheets, this material has not only been used in *Fabry-Pérot* devices but has also been applied in stimuli-responsive 1DPCs.[30,97,99,100]

In the second part of this introduction, the invited review written on stimuli-responsive 1DPCs gives further insight into the application of $H_3Sb_3P_2O_{14}$ nanosheets used as active material in different vapor sensing applications (Section 2.7.3), which is also of great importance for the work conducted in this thesis. Moreover, it provides general information on the role 1DPCs play in the field of sensing, theoretical background information, the underlying sensing principles, possible stimuli, and a conceptual overview of the state of the art of 1DPC sensors.

1.7 References

1. Y. Ma, Y. Liu, L. Zhang, Y. Cao, S. Guo, H. Li, *Symmetry* **2021**, *13*, 128.
2. S. Chen, Y. Wang, S. Choi, *Open J. Appl. Biosens.* **2013**, *2*, 39.
3. B. Kuswandi, Y. Wicaksono, Jayus, A. Abdullah, L. Y. Heng, M. Ahmad, *Sens Instrum Food Qual Saf.* **2011**, *5*, 137.
4. E. Traversa, *Sens. Actuators B Chem.* **1995**, *23*, 135.
5. Z. M. Rittersma, *Sens. Actuators A Chem. Phys.*, **2002**, *96*, 196.
6. P. R. Wallace, *Phys. Rev.* **1947**, *71*, 622.
7. H. P. Boehm, A. Clauss, G. O. Fischer, U. Hofmann, *Z. anorg. allg. Chem.* **1962**, *316*, 119.
8. K. S. Novoselov, A. K. Geim, S. V. Morozov, D. Jiang, Y. Zhang, S. V. Dubonos, I. V. Grigorieva, A. A. Firsov, *Science* **2004**, *306*, 666.
9. A. K. Geim, K. S. Novoselov, *Nat. Mater.* **2007**, *6*, 183.
10. A. K. Geim, I. V. Grigorieva, *Nature* **2013**, *499*, 419.
11. S. Park, R. S. Ruoff, *Nature Nanotechnol.* **2009**, *4*, 217.
12. M. Giersig, L. M. Liz-Marzán, *Low-Dimensional Systems: Theory, Preparation, and Some Applications*, Springer, Berlin, Germany, **2003**.
13. K. J. Koski, Y. Cui, *ACS Nano* **2013**, *7*, 3739.

14. C. Ziegler, S. Werner, M. Bugnet, M. Woersching, V. Duppel, G. A. Botton, C. Scheu, B. V. Lotsch, *Chem. Mater.* **2013**, *25*, 4892.

15. B. V. Lotsch, *Annu. Rev. Mater. Res.* **2015**, *45*, 85.

16. A. Reina, X. Jia, J. Ho, D. Nezich, H. Son, V. Bulovic, M. S. Dresselhaus, J. Kong, *Nano Lett.* **2009**, *9*, 30.

17. S. Z. Butler, S. M. Hollen, L. Cao, Y. Cui, J. A. Gupta, H. R. Gutierrez, T. F. Heinz, S. S. Hong, J. Huang, A. F. Ismach, E. Johnston-Halperin, M. Kuno, V. V. Plashnitsa, R. D. Robinson, R. S. Ruoff, S. Salahuddin, J. Shan, L. Shi, M. G. Spencer, M. Terrones, W. Windl, J. E. Goldberger, *ACS Nano* **2013**, *7*, 2898.

18. X. Chen, S. S. Mao, *Chem. Rev.* **2007**, *107*, 2891.

19. R. Mas-Balleste, C. Gomez-Navarro, J. Gomez-Herrero, F. Zamora, *Nanoscale* **2011**, *3*, 20.

20. V. Nicolosi, M. Chhowalla, M. G. Kanatzidis, M. S. Strano, J. N. Coleman, *Science* **2013**, *340*, 1226419.

21. P. Joensen, R. F. Frindt, S. R. Morrison, *Mater. Res. Bull.* **1986**, *21*, 457.

22. Y. Ebina, T. Sasaki, M. Watanabe, *Solid State Ion.* **2002**, *151*, 177.

23. J. N. Coleman, M. Lotya, A. O'Neill, S. D. Bergin, P. J. King, U. Khan, K. Young, A. Gaucher, S. De, R. J. Smith, I. V. Shvets, S. K. Arora, G. Stanton, H.-Y. Kim, K. Lee, G. T. Kim, G. S. Duesberg, T. Hallam, J. J. Boland, J. J. Wang, J. F. Donegan, J. C. Grunlan, G. Moriarty, A. Shmeliov, R. J. Nicholls, J. M. Perkins, E. M. Grieveson, K. Theuwissen, D. W. McComb, P. D. Nellist, V. Nicolosi, *Science* **2011**, *331*, 568.

24. B. Radisavljevic, A. Radenovic, J. Brivio, V. Giacometti, A. Kis, *Nat. Nanotechnol.* **2011**, *6*, 147.

25. F. Bonaccorso, A. Bartolotta, J. N. Coleman, C. Backes, *Adv. Mater.* **2016**, *28*, 6136.

26. K. Matsuba, C. Wang, K. Saruwatari, Y. Uesusuki, K. Akatsuka, M. Osada, Y. Ebina, R. Ma, T. Sasaki, *Sci. Adv.* **2017**, *3*, e1700414.

27. Y. Hernandez, V. Nicolosi, M. Lotya, F. M. Blighe, Z. Sun, S. De, I. T. McGovern, B. Holland, M. Byrne, Y. K. Gun'Ko, J. J. Boland, P. Niraj, G. Duesberg, S. Krishnamurthy, R. Goodhue, J. Hutchison, V. Scardaci, A. C. Ferrari, J. N. Coleman, *Nat. Nanotechnol.* **2008**, *3*, 563.

28. A. Kuhn, T. Holzmann, J. Nuss, B. V. Lotsch, *J. Mater. Chem. A* **2014**, *2*, 6100.

29. C. Backes, T. M. Higgins, A. Kelly, C. Boland, A. Harvey, D. Hanlon, J. N. Coleman, *Chem. Mater.* **2017**, *29*, 243.

30. K. Szendrei-Temesi, O. Sanchez-Sobrado, S. B. Betzler, K. M. Durner, T. Holzmann, B. V. Lotsch, *Adv. Funct. Mater.* **2018**, *28*, 1705740.

31. R. J. Smith, M. Lotya, J. N. Coleman, *New J. Phys.* **2010**, *12*, 125008.

32. C. N. R. Rao, H. S. S. Ramakrishna Matte, U. Maitra, *Angew. Chem. Int. Ed.* **2013**, *52*, 13162.

33. Z. Zeng, Z. Yin, X. Huang, H. Li, Q. He, G. Lu, F. Boey, H. Zhang, *Angew. Chem. Int. Ed.* **2011**, *50*, 11093.

34. H. S. S. Ramakrishna Matte, A. Gomathi, A. K. Manna, D. J. Late, R. Datta, S. K. Pati, C. N. R. Rao, *Angew. Chem. Int. Ed.* **2010**, *49*, 4059.

35. G. Eda, M. Chhowalla, *Adv. Mater.* **2010**, *22*, 2392.

36. C.-J. Shih, A. Vijayaraghavan, R. Krishnan, R. Sharma, J.-H. Han, M.-H. Ham, Z. Jin, S. Lin, G. L. C. Paulus, N. F. Reuel, Q. H. Wang, D. Blankschtein, M. S. Strano, *Nat. Nanotechnol.* **2011**, *6*, 439.

37. R. Ma, T. Sasaki, *Adv. Mater.* **2010**, *22*, 5082.

38. R. Ma, T. Sasaki, *Acc. Chem. Res.* **2015**, *48*, 136.

39. T. Maluangnont, K. Matsuba, F. Geng, R. Ma, Y. Yamauchi, T. Sasaki, *Chem. Mater.* **2013**, *25*, 3137.

40. R. E. Schaak, T. E. Mallouk, *Chem. Mater.* **2000**, *12*, 2513.

41. J.-C. P. Gabriel, F. Camerel, B. J. Lemaire, H. Desvaux, P. Davidson, P. Batail, *Nature* **2001**, *413*, 504.

42. F. Bonaccorso, A. Bartolotta, J. N. Coleman, C. Backes, *Adv. Mater.* **2016**, *28*, 6136.

43. S. S. Chou, M. De, J. Kim, S. Byun, C. Dykstra, J. Yu, J. Huang, V. P. Dravid, *J. Am. Chem. Soc.* **2013**, *135*, 4584.

44. Z. Wang, J. Xuan, Z. Zhao, Q. Li, F. Geng, *ACS Nano* **2017**, *11*, 11559.

45. C. Backes, B. M. Szydłowska, A. Harvey, S. Yuan, V. Vega-Mayoral, B. R. Davies, P.-l. Zhao, D. Hanlon, E. J. G. Santos, M. I. Katsnelson, W. J. Blau, C. Gadermaier, J. N. Coleman, *ACS Nano* **2016**, *10*, 1589.

46. M. Osada, T. Sasaki, *Int. J. Appl. Ceram. Technol.* **2012**, *9*, 29.

47. J. Wan, S. D. Lacey, J. Dai, W. Bao, M. S. Fuhrer, L. Hu, *Chem. Soc. Rev.* **2016**, *45*, 6742.

48. D. Sarkar, X. Xie, J. Kang, H. Zhang, W. Liu, J. Navarrete, M. Moskovits, K. Banerjee, *Nano Lett.* **2015**, *15*, 2852.

49. D. Voiry, A. Goswami, R. Kappera, E. SilvaCecilia de Carvalho Castro, D. Kaplan, T. Fujita, M. Chen, T. Asefa, M. Chhowalla, *Nat. Chem.* **2015**, *7*, 45.

50. W. L. B. Huey, J. E. Goldberger, *Chem. Soc. Rev.* **2018**, *47*, 6201.

51. P. Ganter, Ph.D. Thesis, LMU Munich, **2018**.

52. A. Clearfield, Intercalation Chemistry of Selected Layered Oxides and Phosphates. In *Progress in Intercalation Research. Physics and Chemistry of Materials with Low-Dimensional Structures*, Vol. 17; Springer, Berlin, Germany, **1994**.

53. J. Yao, K. J. Koski, W. Luo, J. J. Cha, L. Hu, D. Kong, V. K. Narasimhan, K. Huo, Y. Cui, *Nat. Commun.* **2014**, *5*, 5670.

54. S. Stankovich, D. A. Dikin, O. C. Compton, G. H. B. Dommett, R. S. Ruoff, S. T. Nguyen, *Chem. Mater.* **2010**, *22*, 4153.

55. F. Xiong, H. Wang, X. Liu, J. Sun, M. Brongersma, E. Pop, Y. Cui, *Nano Lett.* **2015**, *15*, 6777.

56. M. Kühne, F. Paolucci, J. Popovic, P. M. Ostrovsky, J. Maier, J. H. Smet, *Nat. Nanotechnol.* **2017**, *12*, 895.

57. M. Rajapakse, B. Karki, U. O. Abu, S. Pishgar, M. R. K. Musa, S. M. S. Riyadh, M. Yu, G. Sumanasekera, J. B. Jasinski, *npj 2D Mater. Appl.* **2021**, *5*, 30.

58. P. Ganter, L. M. Schoop, M. Däntl, B. V. Lotsch, *Chem. Mater.* **2018**, *30*, 2557.

59. Y. Song, Y. Xu, Q. Guo, Z. Hua, F. Yin, W. Yuan, *ACS Appl. Mater. Interfaces* **2021**, *13*, 39772.

60. H.-J. Koh, S. J. Kim, K. Maleski, S.-Y. Cho, Y.-J. Kim, C. W. Ahn, Y. Gogotsi, H.-T. Jung, *ACS Sens.* **2019**, *4*, 1365.

61. W. Yang, L. Gan, H. Li, T. Zhai, *Inorg. Chem. Front.* **2016**, *3*, 433.

62. S. Yang, C. Jiang, S.-h. Wei, *App. Phys. Rev.* **2017**, *4*, 021304.

63. S. Borini, R. White, D. Wei, M. Astley, S. Haque, E. Spigone, N. Harris, J. Kivioja, T. Ryhänen, *ACS Nano* **2013**, *7*, 11166.

64. J. Feng, L. Peng, C. Wu, X. Sun, S. Hu, C. Lin, J. Dai, J. Yang, Y. Xie, *Adv. Mater.* **2012**, *24*, 1969.

65. F. K. Perkins, A. L. Friedman, E. Cobas, P. M. Campbell, G. G. Jernigan, B. T. Jonker, *Nano Lett.* **2013**, *13*, 668.

66. J.-S. Kim, H.-W. Yoo, H. O. Choi, H.-T. Jung, *Nano Lett.* **2014**, *14*, 5941.

67. M. Sajjad, P. Feng, *Mater. Res. Bull.* **2014**, *49*, 35.

68. R. Gatensby, N. McEvoy, K. Lee, T. Hallam, N. C. Berner, E. Rezvani, S. Winters, M. O'Brien, G. S. Duesberg, *Appl. Surf. Sci.* **2014**, *297*, 139.

69. B. Chen, H. Liu, X. Li, C. Lu, Y. Ding, B. Lu, *Appl. Surf. Sci.* **2012**, *258*, 1971.

70. Q. He, Z. Zeng, Z. Yin, H. Li, S. Wu, X. Huang, H. Zhang, *Small* **2012**, *8*, 2994.

71. C. Zheng, X. Jin, Y. Li, J. Mei, Y. Sun, M. Xiao, H. Zhang, Z. Zhang, G.-J. Zhang, *Sci. Rep.* **2019**, *9*, 759.

72. S.-Y. Cho, Y. Lee, H.-J. Koh, H. Jung, J.-S. Kim, H.-W. Yoo, J. Kim, H.-T. Jung, *Adv. Mater.* **2016**, *28*, 7020.

73. K. Y. Ko, J.-G. Song, Y. Kim, T. Choi, S. Shin, C. W. Lee, K. Lee, J. Koo, H. Lee, J. Kim, T. Lee, J. Park, H. Kim, *ACS Nano* **2016**, *10*, 9287.

74. H. Chi, Y. J. Liu, F. Wang, C. He, *ACS Appl. Mater. Interfaces* **2015**, *7*, 19882.

75. E. R. Kleinfeld, G. S. Ferguson, *Chem. Mater.* **1995**, *7*, 2327.

76. P. Ganter, K. Szendrei, B. V. Lotsch, *Adv. Mater.* **2016**, *28*, 7436.

77. P. Ganter, L. M. Schoop, B. V. Lotsch, *Adv. Mater.* **2017**, *29*, 1604884.

78. K. Szendrei-Temesi, Ph.D. Thesis, LMU Munich, **2018**.

79. V. Veselý, V. Pekárek, *Talanta* **1972**, *19*, 219.

80. A. Clearfield, J. A. Stynes, *J. Inorg. Nucl. Chem.* **1964**, *26*, 117.

81. A. Winkler, E. Thilo, *Z. Anorg. Allg. Chem.* **1966**, *346*, 92.

82. S. Oyetola, A. Verbaere, D. Guyomard, Y. Piffard, M. Tournoux, *Eur. J. Solid State Inorg. Chem.* **1989**, *26*, 175.

83. S. Oyetola, A. Verbaere, Y. Piffard, M. Tournoux, *Eur. J. Solid State Inorg. Chem.* **1988**, *25*, 259.

84. L. J. J. Zah, P. Houenou, A. Verbaere, Y. Piffard, M. Tournoux, *Mater. Sci. Forum* **1994**, *152-153*, 255.

85. S. Deniard-Courant, Y. Piffard, P. Barboux, J. Livage, *Solid State Ion.* **1988**, *27*, 189.

86. Y. Piffard, A. Lachgar, M. Tournoux, *J. Solid State Chem.* **1985**, *58*, 253.

87. Y. Piffard, S. Oyetola, S. Courant, A. Lachgar, *J. Solid State Chem.* **1985**, *60*, 209.

88. G. Alberti, M. Casciola, U. Costantino, *J. Colloid Interface Sci.* **1985**, *107*, 256.

89. Q. Huang, W. Wang, Y. Yue, W. Hua, Z. Gao, *J. Colloid Interface Sci.* **2003**, *257*, 268.

90. F. Camerel, J. C. P. Gabriel, P. Batail, P. Panine, P. Davidson, *Langmuir* **2003**, *19*, 10028.

91. M. Däntl, New Insights into $H_3Sb_3P_2O_{14}$ Thin Films: Intercalation Behavior and In Situ Relative Humidity XRD Studies. LMU Munich, 2017.

92. C. S. Griffith, V. Luca, J. Cochrane, J. V. Hanna, *Microporous Mesoporous Mater.* **2008**, *111*, 387.

93. A. Lachgar, S. Deniard-Courant, Y. Piffard, *J. Solid State Chem.* **1988**, *73*, 572.

94. Y. Piffard, A. Verbaere, A. Lachgar, S. Deniard-Courant, M. Tournoux, *Rev. Chim. Miner.* **1986**, *23*, 766.

95. H. B. Attia, C. Iojoiu, J. C. Leprêtre, J. Guindet, N. Bellakhal, J. Y. Sanchez, *Energy Procedia* **2012**, *14*, 1717.

96. P. Genova-Dimitrova, B. Baradie, D. Foscallo, C. Poinsignon, J. Y. Sanchez, *J. Membr. Sci. Res.* **2001**, *185*, 59.

97. K. Szendrei, P. Ganter, O. Sànchez-Sobrado, R. Eger, A. Kuhn, B. V. Lotsch, *Adv. Mater.* **2015**, *27*, 6341.

98. M. N. Ghazzal, O. Deparis, J. De Coninck, E. M. Gaigneaux, *J. Mater. Chem. C* **2013**, *1*, 6202.

99. K. Szendrei-Temesi, A. Jiménez-Solano, B. V. Lotsch, *Adv. Mater.* **2018**, *30*, 6289.

100. K. Szendrei, A. Jiménez-Solano, G. Lozano, B. V. Lotsch, H. Míguez, *Adv. Opt. Mater.* **2017**, *5*, 1700663.

2 Introduction 1-Dimensional Photonic Crystals

Stimuli-Responsive One-Dimensional Photonic Crystals: Design, Fabrication and Sensing

The work in this Chapter was reproduced and adapted from:

*Marie Däntl, Alberto Jiménez-Solano, Bettina V. Lotsch**

Published in: *Materials Advances* **2022**, Advance Article.

DOI: 10.1039/D2MA00793B

https://pubs.rsc.org/en/content/articlelanding/2022/ma/d2ma00793b

Contributions: Marie Däntl and Alberto Jiménez-Solano defined the scope of the manuscript and edited the figures. Marie Däntl wrote the manuscript with the help of all contributing authors.

2.1 Abstract

A wide range of sensors, for example in healthcare, electronics or environmental monitoring, have become indispensable parts of our everyday life and smart sensing technologies, fueled by the Internet of Things, are in high demand. However, most sensors rely on a complex readout as they depend on additional electronics and hence the demand for sensors that can be read out optically with a camera or the naked eye has been growing significantly. Photonic crystals (PCs) and related sensing principles are promising candidates as they are responsive to different stimuli and their readout can be achieved optically. In addition, the properties of PCs can be tailored on-demand so as to meet the users' requirements. In this review, we present an overview of the state-of-the-art of stimuli-responsive PC sensors and delineate how stimuli-responsiveness can be created for desired applications based on optical design and nanoscale fabrication.

2.2 Introduction

In the past few decades, especially since the rise of the Internet of Things (IoT), there has been an ever-growing demand for sensors as they have become an integral part of everyday life, and novel applications keep emerging.[1] This is evident from the increasing number of publications (over half a million) found in an analysis of the Web of Sciencet core database for the term "sensor" taking into account the years 2013–2021. There are diverse applications for sensors such as in environmental monitoring,[2,3] food and water control,[4] medical devices,[5] wearables,[6,7] smartphones,[8] or optoelectronics.[9] In particular, gas sensor technologies have attracted great interest (45,770 publications for "gas sensor" from 2013–2021 in the Web of Sciencet core database), and the development of new applications leads to new technological challenges and economical requirements. For example, the stability, cyclability, selectivity and sensitivity, quick response, miniaturization, low power consumption, low cost and possibility for wireless communication are factors that should be taken into account.[10] Depending on the specific application, different readout and detection principles are favored. The most widely used gas sensing platforms are based on metal oxide semiconductor (MOS)[11] or electrochemical sensors,[12] which make use of changes in the resistance, capacitance or current within the active material upon exposure to a stimulus. Other possibilities include chromatography-based detection, or calorimetric elements, such as catalytic beads, which measure temperature or resistance shifts upon gas adsorption, and acoustic sensors that measure the change in velocity. However, the latter methods tend to be either costly, exhibit low sensitivity, or rely on a complex readout.[13] In contrast, colorimetric sensors, especially when combined with statistical data analysis techniques such as principal component analysis (PCA), are a promising detection platform as they can provide label-free readout without additional wiring due to color changes in response to an external stimulus, which can be detected qualitatively with the naked eye.[14–17] This is evident from the analysis of the number of publications (9796 from 2015–2021) and citations (161,540 from 2015–2021) found for the keyword "colorimetric sensor" in the Web of Science™ core database (see Fig. 2.1). The implementation of a naked eye readout may play an important role in the progressive miniaturization of sensors, especially for applications regarding the IoT.

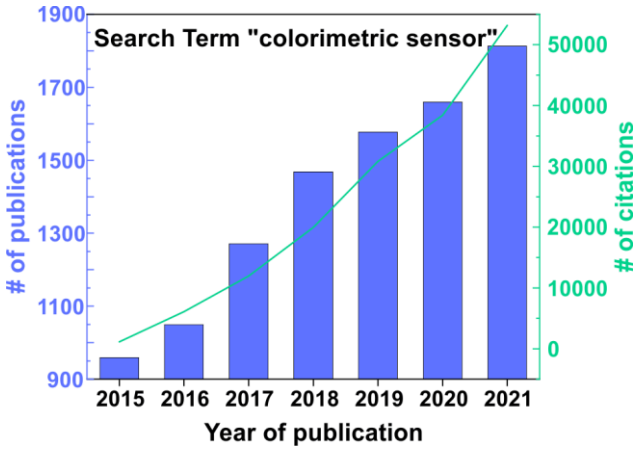

Fig. 2.1 Number of publications per year (left y-axis) and number of citations per year (right y-axis) for the keyword "colorimetric sensor" in the Web of Science™ core database. Accessed 27.06.2022.

Photonic crystals (PCs) are ideal candidates for the fabrication of such colorimetric sensors, as they can be used for gas sensing and the detection of other external stimuli alike.[18–20] They are label-free, can exhibit quick response times, and their fabrication as well as functionalization is facile.[21]

In general, PCs are comprised of two dielectric materials (including air) with different refractive indices (RIs) and show optical band structures characterized by photonic bandgaps. In terms of architectures, PCs can be divided into 1-, 2- or 3D periodic structures according to the dimensionality of their lattice.[22] Especially one-dimensional photonic crystals (1DPCs), also known as Bragg stacks (BSs), Bragg mirrors or distributed Bragg reflectors (DBRs), which are comprised of two materials with low and high RIs stacked alternatingly in one spatial direction, are interesting candidates for colorimetric sensing applications. This arises from the fact that the theory and sensing mechanism underlying 1DPCs is particularly straightforward, which enables the prediction of their properties and the rational design to meet the users' requirements.[23] For this reason, our review focuses on 1DPCs. Furthermore, a large library of materials, including nanoparticles, polymers, and nanosheets, has been explored for the fabrication (see Fig. 2.2) of stimuli-responsive 1DPCs, and their properties can be rationally tuned by intercalation or inclusion of defects, which makes them a uniquely versatile sensing platform.[18]

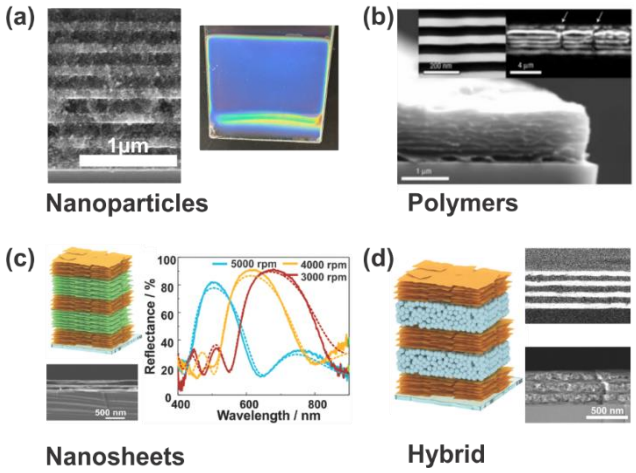

Fig. 2.2 Different materials used for the fabrication of stimuli-responsive 1DPCs. (a) Inorganic TiO_2 and SiO_2 nanoparticles. (b) Polystyrene-b-quaternized poly(2-vinyl pyridine) (PS-b-QP2VP) polymers; Reprinted with permission from ref. 24, Copyright 2007 Springer Nature. (c) $H_3Sb_3P_2O_{14}$ and $Li_2Sn_2S_5$ nanosheets; Adapted and reprinted with permission from ref. 25, Copyright 2018 John Wiley and Sons. (d) $Li_2Sn_2S_5$ nanosheets and TiO_2 nanoparticles; Adapted and reprinted with permission from ref. 25, Copyright 2018 John Wiley and Sons.

In this review, we highlight the research in the field of stimuli-responsive 1DPCs on a conceptual level to showcase the many possibilities regarding their design and application. We do so by presenting basic information on the fabrication of 1DPCs and the materials that can be used, as well as the theoretical concepts underlying their optical properties that allow the design and fine-tuning of stimuli-responsive 1DPCs. Furthermore, we give an overview of the state-of-the-art of stimuli-responsive 1DPCs considering different sensing mechanisms (RI vs. layer thickness change) as well as possible stimuli (physical and chemical). Finally, we discuss selected applications of stimuli-responsive 1DPCs with a focus on vapor and gas sensing as we anticipate that this field has the highest potential for future applications. Before a short outlook, we address the challenges of the sensor performance and how they may be overcome.

2.3 Fabrication of 1DPCs

In this section, we give an overview of the different fabrication approaches that are typically used for creating 1DPCs and compare their advantages and disadvantages.

In general, PCs can be fabricated by top-down as well as bottom-up methods.[26,27] Top-down methods mostly rely on traditional microfabrication tools such as etching to produce microstructures from bulk materials, and are often more controllable than bottom-up techniques. For instance, a 1DPC consisting of porous silicon was fabricated by means of electrochemical etching in acidic medium by controlling the electrical pulse to achieve different

levels of porosity in the layers.[28] Further, wet chemical etching was performed to obtain porous GaN structures by removing a sacrificial layer.[29] However, many microfabrication processes require complex instrumentation, which is why microfabricated crystals are not typically used for the preparation of 1DPCs. Due to the experimental ease of bottom-up techniques, we limit our discussion to these approaches with the focus lying on wet deposition methods.

The bottom-up technique is often favored as an efficient and scalable approach that makes use of the assembly of preformed building blocks into periodic photonic structures. Generally, self-assembly is defined as the spontaneous organization of matter, e.g. atoms, molecules, colloids or polymers, to a higher level of structural order and complexity by means of non-covalent interactions. This process can be driven by different kinds of weak forces that operate over multiple length scales.[30] So far, the most widely used method for the fabrication of 1DPCs is evaporation-induced self-assembly (EISA).[31] It has been applied, e.g., for the assembly of anisotropic as well as spherical nanocrystals on solid substrates. Particularly, the assembly of the building blocks begins from a homogeneous solution or suspension with a high degree of disorder. When the suspension is spread on a flat and clean substrate (e.g. silicon or glass), evaporation of the solvent in a controlled manner leads to a progressively increasing concentration of the building blocks, which results in the assembly of the building blocks in a preferred orientation at the air/solvent or substrate/ solvent interface, thereby forming highly ordered films. The assembly is driven by the fact that the relatively weak attractive forces (e.g. van der Waals forces or electrostatic interactions) between the nanocrystals become apparent due to the fact that they come closer to one another with decreasing volume of the solvent.[32]

The easiest form of EISA is the drop-casting method in which a drop of the suspension is placed on a substrate and the sample is left to dry, which induces an assembly of the building blocks at the liquid/air interface during evaporation. With this method, the formation of a film is fast and the process is scalable, but the homogeneity and the control over positioning and alignment of the building blocks is quite low compared to other solvent mediated deposition methods.[33] Especially the edges of the drop-casted film are much thicker than the rest of the sample due to the so-called "coffee ring effect", which also negatively influences the reproducibility of drop-casted samples.[34,35] Thus, due to its drawbacks, this method is not used frequently for the fabrication of 1DPCs, but is rather applicable for the formation of thin films where thickness control is no primary concern.

Another straightforward solution processing approach for the fabrication of high-quality 1DPCs, which relies on EISA, is the spin-coating method. It has been applied for various systems such as NP suspensions,[36,37] nanosheet suspensions,[25] or polymer solutions.[38] For this process, stable colloidal suspensions with known concentrations are used. It is favorable to prepare the suspensions in a solvent that evaporates quickly, such as alcohols, in order to fabricate homogeneous layers. After deposition of the suspension on a substrate, it is rotated at 2000 to 4000 revolutions per minute (rpm), whereby the majority of the excess material is removed during the acceleration step due to centrifugal forces. The spinning leads to an evaporation of the volatile solvent, which increases the viscosity of the remaining suspension, and the thin film is formed (see Fig. 2.3). Subsequently a heating step is applied to stabilize the thin film by removing residual solvent. For the formation of multilayer structures, the spin-coating and heating steps are repeated until the desired number of layers is achieved. Since the film thickness can easily be controlled and tuned by variation of the acceleration speed, final rotation speed, concentration of the suspensions or the number of applied deposition steps, the thickness and therefore the properties of 1DPCs can easily be designed and predicted (see Chapter 2.4). Note that the choice of solvents has to be made carefully to avoid dissolution and penetration between the constituent layers.[39] Major advantages of this method include reproducibility, low cost and a high degree of scalability, as they are compatible with current microfabrication technology.[40] However, the drawbacks are that most of the suspension used for the film-formation is wasted as it is spun off during rotation, and that striating often occurs due to the spinning (see microscope image in Fig. 2.3).

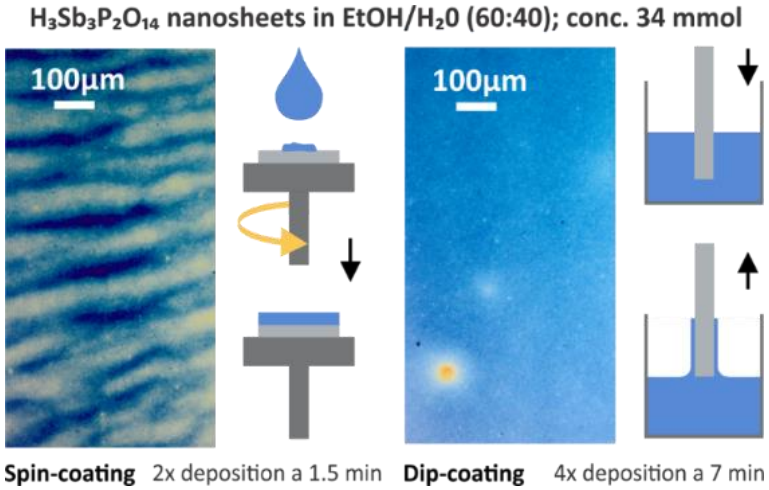

Fig. 2.3 Comparison of $H_3Sb_3P_2O_{14}$ nanosheet-based thin films obtained by spin- (left) and dip-coating (right) including microscope images, the used parameters and schematic descriptions of both processes.

Similar to spin-coating, the dip-coating technique, which is also used in the context of layer-by-layer (LBL) assembly, relies on EISA from stable colloidal suspensions and quick evaporation of the solvent is needed to ensure a homogeneous deposition. It has been applied for various systems such as NP-based 1DPCs,[41-43] or the fabrication of hybrid TiO_2/polymer 1DPCs,[44] to name a few. Generally, a substrate is dipped into the suspension (often using an automated dipping system or robot), retrieved with a certain speed and left to dry before the next dip (see Fig. 2.3). During the drying process, the capillary force-induced meniscus at the interface of the substrate and the dispersion acts as the driving force for the crystallization of the building blocks into a thin film.[45] For the formation of multilayer structures, the dip-coating and drying steps are repeated until the desired number of layers is obtained. Compared to spin-coating, the obtained structures are more homogenous (see microscope image in Fig. 2.3) and exhibit less defects, especially at the corners of the sample. Also, striating, which is often observed in spin-coated samples, occurs less frequently. Moreover, dip-coated structures can be assembled on curved surfaces or spheres, unlike spin-coated 1DPCs.[46] By controlling the concentration and viscosity of the suspension, the number of dips or the retrieval speed, the thickness of the resulting 1DPCs can be judiciously designed. However, a rather large amount of suspension in which the substrate can be immersed is required. Moreover, a higher number of dipping steps is often needed to obtain a similar sample thickness compared to the spin-coating technique, and the drying time between the dips is longer than for spin-coated samples. This in turn is time consuming and sedimentation of the particles in the suspension or evaporation of the solvent can occur, resulting in an altered concentration of the suspension. Therefore, depending on the number of fabricated samples, they may not be comparable. Furthermore, the humidity and temperature may also vary over time, which might lead to changes in solvent evaporation or drying times between the dipping steps and hence environmental parameters (temperature, humidity) need to be kept constant during the entire sample fabrication time.

Another bottom-up approach for the fabrication of 1DPCs is the self-assembly of block copolymers, which is based on microphase separation driven by the positive free energy of mixing of the chemically different polymer blocks.[18] Usually the following steps are involved: initially the copolymer precursor solution is spin-coated on a substrate, which is followed by a solvent vapor annealing step. The annealing induces movement of the polymer chains, which leads to the formation of ordered layers.[39] Optional steps are quaternizing and crosslinking of the polymers. For instance, this approach was applied for the fabrication of Polystyrene-*b*-

quaternized poly(2-vinyl pyridine) (PS-*b*-QP2VP) PCs.[24] Since this fabrication method is based on the self-assembly of block copolymers, the material choice is obviously limited. Nevertheless, the 1DPCs obtained with this method are highly ordered and can be fabricated in a facile manner.

2.4 Optical Properties of Photonic Crystals

In order to predict and design stimuli-responsive PCs for various sensing applications, it is important to understand their optical properties and sensing mechanism. PCs are nanostructures comprised of periodically arranged dielectric materials with different RIs. In 1987, John and Yablonovitch independently recognized and explored the conceptional analogy between the electronic structure of periodic solids and their dielectric counterparts, making photonic band gap (PBG) materials or PCs the electromagnetic analogue to semiconductor crystals. PCs have the ability to influence the propagation of electromagnetic waves due to the periodicity of their dielectric function, similar to how the motion of electrons is affected by the periodic lattice in semiconductor crystals.[47,48] It was shown that PCs exhibit optical band structures and possess photonic bandgaps, whereby the latter are defined as the frequency ranges in which the propagation of electromagnetic waves is forbidden in certain directions within the structure. The possibility to control the flow of light within PBG materials renders them suitable for various applications such as optical fibers, filters, waveguides, or colorimetric sensors.[49–51]

As mentioned before, PCs can be periodic in 1-, 2- or 3 spatial dimensions (Fig. 2.4), which influences the resulting dimensionality of their bandgap in reciprocal space.[22]

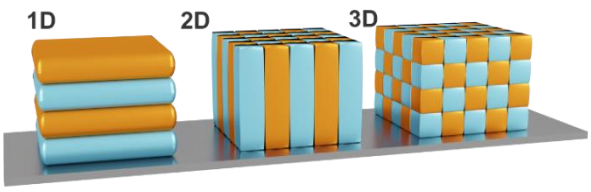

Fig. 2.4 Schematic representation of 1D, 2D and 3D PCs. Different colors indicate different dielectric constants, exhibiting periodicity in one- (1D), two- (2D) or three-dimensions (3D).

Inspired by photonic nanostructures known from nature such as peacock feathers[52] or butterfly wings,[53] much effort has been directed to creating artificial PCs. The efforts regarding the understanding of the physical theories behind PCs, along with major advances in the fabrication and material development, rapidly transformed this class of materials into a

versatile, multifunctional platform for optical sensing. Especially 1DPCs are interesting candidates for colorimetric sensing applications as their fabrication is facile compared to 2D and 3DPCs.[54] Moreover, the properties and sensing mechanism of 1DPCs are easy to predict and hence open up the opportunity to rationally design and control the stimuli-responsiveness of the PCs.[37]

According to Eq. 2.1, a strong interaction of the PC with visible light occurs if the periodicity, e.g. the optical thickness t of the material, is in the same range as the wavelength of the light interacting with the PC. Hereby, τ is given by the product of the thickness of an individual layer, d_l or d_h (for the low or high RI material), and its RI n_l or n_h, respectively:[54]

$$\tau_l = n_l \cdot d_l \qquad \text{(Eq. 2.1)}$$

The reflection and diffraction of light impinging on the periodic arrangement of dielectric films in the PC can be described in a similar fashion as the phenomenon of X-ray diffraction: upon propagation of the incident beam through the material, it is partially diffracted and reflected at each interface of layers with different RIs as a function of the optical thickness t of the constituent layers contributing to the bilayer (see Fig. 2.5) and the angle of incidence (see Eq. 2.2). Note that the stack of a high and a low RI layer is referred to as a bilayer.

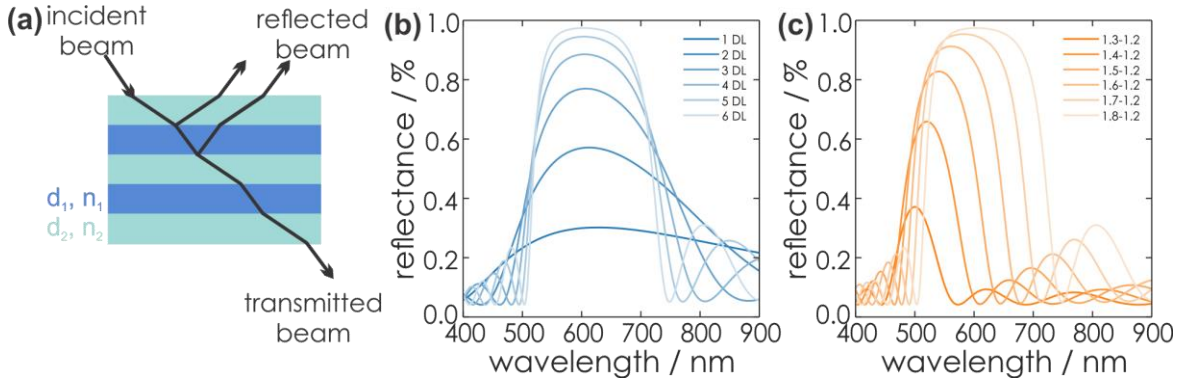

Fig. 2.5 (a) Schematic description of the interaction of light with a 1DPC. The incident beam is partially diffracted at the interfaces between different materials. (b) Calculated model of the influence of the number of bilayers comprising the 1DPC on the optical properties. The RI of the low RI material was n_l = 1.2 for the low and n_h = 1.8 for the high RI material. The number of bilayers was varied from 1 to 6. (c) Calculated model of the influence of the refractive indices of the materials comprising the 1DPC on the optical properties. The low RI was fixed to n_l = 1.2 while the high RI was varied from n_h = 1.3 to n_h = 1.8 in steps of 0.1. The number of bilayers was fixed at 6. Note that (b) and (c) were calculated for a glass substrate with n = 1.51 and a thickness of 1 mm.

The reflected light beams interfere in a constructive or destructive fashion, which leads to a strong reflectance in a defined wavelength regime, while at the other wavelengths the light is

transmitted. The former phenomenon describes the forbidden energy range in which no light waves propagate in the structure along the direction of periodicity.[55] In this range, a reflection maximum occurs, whereas the other spectral regions exhibit a maximum in transmission. Thus, by periodic stacking of inherently colorless materials, it is possible to achieve a strong color, so called structural color, provided the photonic bandgap lies in the visible region of the spectrum. This phenomenon can be exploited for optical sensing or for the application of PCs as wavelength-selective filters. The central position of the photonic stopband can be derived from the Bragg-Snell laws (Eq. 2.2):[18]

$$m\lambda_0 = 2D\sqrt{n_{\text{eff}}^2 - sin^2\,\theta} \qquad \text{(Eq. 2.2)}$$

whereby m is the order of diffraction, λ_0 describes the position of the stopband, D is the lattice parameter with $D = d_l + d_h$, where d_l and d_h describe the layer thicknesses of the constituent layers of the bilayer, n_l and n_h are the corresponding RIs of the constituent layers, and θ the incidence angle, and n_{eff} is the effective refractive index of a bilayer, defined as:

$$n_{\text{eff}} = \frac{n_l d_l + n_h d_h}{D} \qquad \text{(Eq. 2.3)}$$

It is important to mention that real materials usually show both a spectral dependence of the refractive index as well as a non-negligible imaginary part. Although the latter is negligible in dielectric materials, it becomes more noticeable in metals and semiconductors. Furthermore, the effective refractive index of porous layers is typically described by an effective medium approximation, such as those according to Bruggeman[56] or Maxwell-Garnett,[57] among others.Additionally, the intensity of the reflectance R and the bandwidth of the photonic stopband $\measuredangle\lambda_0$ can be expressed mathematically according to Eq. 2.4 and 2.5:

$$R = \left[\frac{n_0 - n_s(n_l/n_h)^{2N}}{n_0 + n_s(n_l/n_h)^{2N}}\right]^2 \qquad \text{(Eq. 2.4)}$$

$$\Delta\lambda_0 = \frac{4\lambda_0}{\pi}\arcsin\left(\frac{n_h - n_l}{n_h + n_l}\right) \qquad \text{(Eq. 2.5)}$$

whereby n_0 and n_s describe the RI of the surrounding medium and the substrate, N is the number of bilayers in the multilayer structure, and n_l and n_h correspond to the RIs of the low and high refractive index material.[18]

Fig. 2.5 gives an overview of the effect of Eq. 2.2, 2.4 and 2.5 on the stopband position and width. An increasing number of bilayers leads to a higher reflectance and a narrowed stopband, while an increase of the RI contrast leads to a higher reflectance as well, but a significant broadening of the bandwidth is observed. Furthermore, by changing the layer thickness, a shift of the stopband position is induced, which is represented in Fig. 2.6.

Considering the above relations, it is evident that the photonic bandgap properties are dependent on the properties of the constituent materials as well as the architecture of the Bragg stack and the properties of the surrounding medium.

2.5 Sensing Mechanisms in Stimuli-Responsive Photonic Crystals

Based on the photonic architectures and physical principles described above, it is possible to create stimuli-responsiveness in PCs. This opens up the opportunity of using PCs for colorimetric sensing if exposure towards a stimulus leads to an altered diffraction wavelength or intensity. Regarding Eq. 2.1, changes in the structural color of the 1DPC occur if a stimulus leads to changes in the RI or the thickness of the constituent layers (Fig. 2.6), or both. In most cases, a combination of both possibilities occurs, whereby one of them is predominant for the sensing mechanism. However, the relative change in layer thickness is often more significant than the change in RI, because the RI of a material can only be varied by a small margin in response to external stimuli, while layer thickness changes are less restricted.

Generally, several sensing mechanisms have been observed in stimuli-responsive 1DPCs. The first two options are based on the response to a stimulus either through pore filling or through swelling of the active material. Typically, these two sensing mechanisms rely on the use of inherently responsive building blocks. Another possible sensing mechanism is based on the inclusion of a responsive “defect layer” in the 1DPC. In the following, we focus on the conceptual overview of the different types of sensing mechanisms in 1DPCs, along with examples of applicable materials.

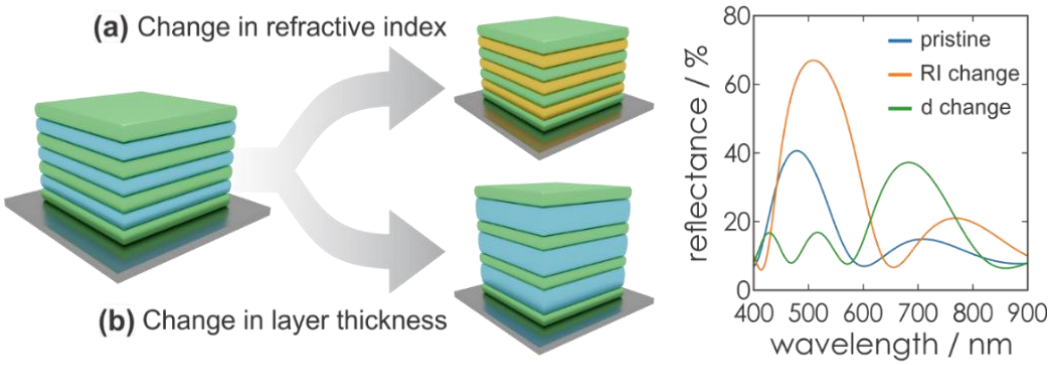

Fig. 2.6 Schematic illustration of the possible sensing mechanisms in a 1DPC. Upon exposure towards an analyte either the refractive index change (top) or the layer thickness change (bottom) is predominant. (a) Calculated red-shift of Bragg peak (orange graph) induced by a change in the RI upon exposure towards a stimulus. The low RI was fixed to $n_l = 1.6$ while the high RI was changed from $n_h = 1.8$ to $n_h = 2.0$. The thickness of each layer was 70 nm. (b) Calculated red-shift of Bragg peak (green graph) induced by a change in the layer thickness upon exposure towards a stimulus. The low RI was fixed to $n_l = 1.6$ and the high RI was fixed to $n_h = 1.8$ while the layer thickness of the high RI material was changed from 70 to 140 nm. Note that the reflectance spectra in (a) and (b) were calculated for a glass substrate with n = 1.51 and a thickness of 1mm.

2.5.1 Sensing Through Pore Filling

In the case of sensing through pore filling, the porosity of the applied 1DPCs can be due to inherent structural porosity of the constituent material, template-induced porosity, or textural porosity. In sensing devices built from porous 1DPCs, the RI is altered upon pore filling through the analyte while the thickness is kept constant, which in turn leads to an optical response of the sensor (Fig. 2.6a). The first porous BS to be reported in this field was the "smart dust" discovered by Sailor et al. in 2003.[58] In this work, two discrete porous multilayered dielectric mirrors were fabricated into silicon through electrochemical etching. One of the mirrors was chemically modified through silane chemistry to exhibit hydrophobic properties, while the other one had hydrophilic properties and both mirrors were designed to have a different optical reflectance. Upon exposure to an analyte, these BSs aligned themselves based on the hydrophilic/hydrophobic properties of the analyte. The subsequent infiltration of the responsive side of the 1DPC leads to a change of the RI and therefore predictable shifts of the optical reflectance are induced.

In 2006 Ozin and co-workers transferred the concept of porous layers for RI sensing to 1DPCs based on mesoporous, sol-gel-derived TiO_2 and SiO_2 layers. The authors demonstrated the optical response of this BS upon infiltration with organic solvents having different RIs such as alcohols and alkanes.[59] The next generation of 1DPCs used for RI sensing was based on

TiO_2 and SiO_2 nanoparticles, leading to textural mesoporosity. These 1DPCs exhibited a response towards volatile organic solvents (VOCs) instead of liquid analytes.[60] Furthermore, porous TiO_2 and SiO_2 1DPCs were attached to a flat gold film to induce a sharp Tamm mode within the stopband of the PC.[61] Tamm plasmons are electromagnetic modes confined at the interface between a noble metal layer and the 1DPC, which lead to a dip in the photonic bandgap. Therefore, changes in the refractive index inside the porous structure induced by the exposure to solvents can be probed as the spectral position of the Tamm mode changes in a precise manner.

Apart from NPs other porous, responsive building blocks such as metal–organic frameworks (MOFs)[62,63] or zeolites[64] have been used for creating stimuli-responsive 1DPCs based on a change of the RI. Since the discovery of the stimuli-responsiveness of porous 1DPCs, many efforts in this research field have been conducted, and nowadays these PCs are used in diverse applications ranging from vapor/solvent sensing,[65,66] to sensing of biologically relevant analytes[67,68] to environmental sensing[3] or water and food quality[4,69] control.

Even though a large number of functional NPs and other porous materials is available for creating responsive 1DPCs, and these sensing devices possess a high molecular selectivity, it is important to note that the sensitivity is often low. This drawback is due to the intrinsically limited RI changes upon analyte infiltration, which translate to a rather small stopband shift according to Eq. 2.2. Therefore, materials that rely on a layer thickness change (shrinking or swelling) as sensing mechanism, such as swellable polymers, are beneficial for higher sensitivity and an increased resolution (see Fig. 2.6).

2.5.2 Sensing Through Swelling

Swelling in a 1DPC (Fig. 2.6b) was first reported in 2007 by Kang et al. using a PC comprised of polymer layers as stimuli-responsive component and infiltration with a liquid analyte lead to a full-spectral stopband shift (from 364 to 1627 nm).[24] Additionally, a broad solvent and solvent mixture response[70] as well as humidity[71] and chloroform vapor sensitivity[72] has been demonstrated in polymer-based organic–inorganic hybrid 1DPCs, highlighting their wide range of applications. As the polymers possess various functional groups, their responsiveness can be tuned to different external stimuli, making them a versatile sensing platform. Even though the fabrication of polymer based 1DPCs (Fig. 2.2b) is facile and the library of possible materials[24,71,73,74] is large, the main disadvantages for polymer based 1DPC sensors are their

low RI contrast, slow response and recovery times towards stimuli, and low chemical and long-term stability.

To overcome these drawbacks, the use of 2D inorganic materials (nanosheets) as building blocks for stimuli-responsive 1DPCs has been explored as they exhibit short response and recovery times to external stimuli by taking up analytes between their layers, leading to layer swelling. Compared to polymers, they are more stable, and there is a large diversity in composition and structure. Like for polymers, it is possible to tailor their properties in order to design their responsiveness. The nanosheets that have been applied in stimuli-responsive 1DPCs include antimony phosphates,[75-77] lithium tin sulfide (Fig. 2.2c),[25] graphene oxide,[78,79] layered double hydroxides,[80] and clays,[81,82] which cover different RIs and therefore allow the fabrication of 1DPCs with a large optical contrast to the other constituent material. Considering that a large RI contrast is beneficial for stimuli-responsiveness, it is desirable to fabricate hybrid (in terms of types of materials, e.g. nanosheet/nanoparticle or nanoparticle/polymer) 1DPCs (Fig. 2.2d), based on either the sensing mechanism (RI vs. swelling materials) or the inorganic/organic nature of the materials.

A further approach to prepare swellable 1DPCs has combined the breathing capability of porous MOF nanoparticles (MIL-88B) with their high chemical selectivity for different VOCs, resulting in large stopband shifts as a function of the analyte (see Chapter 2.7).[83]

2.5.3 Sensing Based on the Inclusion of a Stimuli-Responsive Defect Layer

Another option to exploit the sensing capability of responsive 1DPCs is the inclusion of a "defect layer" with a different optical thickness and responsive properties into the otherwise periodic bilayer structure of 1DPCs in order to induce the tuneability of the photonic bandgap. In this case, the defect layer breaks the periodicity and shifts the position of the allowed state into the original forbidden bandgap.[22] Therefore, a well-defined dip (pass-band) of the reflectance (Fig. 2.7 blue graph) occurs in the photonic stopband, whereby the position and intensity of this transmission maximum is dependent on the optical thickness of the defect layer. Exposure towards a stimulus alters the thickness or RI of the 1DPC, which leads to a shift of the defect state within the bandgap (Fig. 2.7 orange graph). Since the pass-band is sharp compared to the broad stopband, the analyte resolution of the sensor is very high, and hence even subtle changes in the environment can be detected reliably.[84]

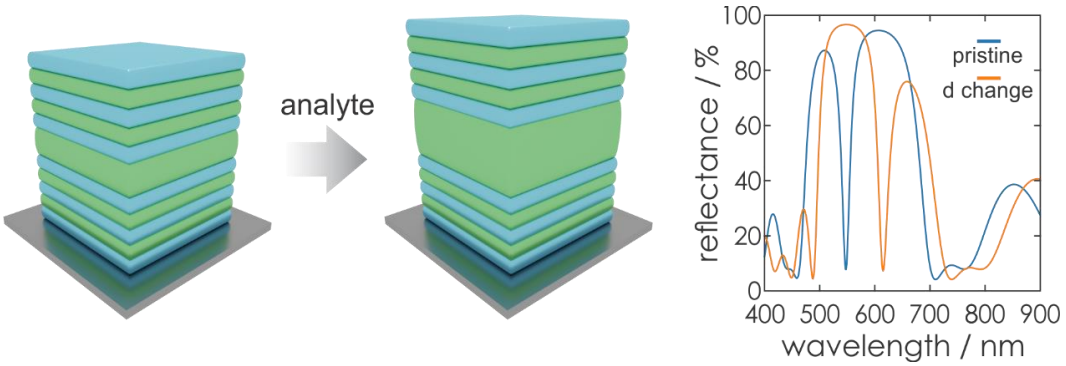

Fig. 2.7 Left: Schematic illustration of a defect layer embedded in a 1DPC. Right: Calculated resulting drop in the reflectance caused by the defect in a 1DPC. The RI of the low RI material was $n_l = 1.5$ and $n_h = 2.0$ for the high RI material and the defect was embedded in the middle (n = 1.5, d = 160 nm) of the 6 bilayers comprising the 1DPC. After analyte exposure, the thickness of the defect layer was 240 nm. Note that the reflectance was calculated for a glass substrate with n = 1.51 and a thickness of 1 mm. The thickness of each layer in the 1DPC was 80 nm.

As many different responsive materials are available as defect layers, such as dyes,[85] metallic particles,[86] MOFs[87] or nanophosphors,[88] the possibilities for manipulating the properties of the PC are vast. Additionally, defect layers in 1DPCs can also be achieved by the inclusion of a thicker layer of one of the constituent stimuli-responsive materials, which has been demonstrated for TiO_2/SiO_2, graphene oxide hydrogel and TiO_2[89] as well as clay and TiO_2/SiO_2[82] PCs, among others. Please note that more detailed examples of defect layers in 1DPCs and their application for vapor sensing are given in Chapter 2.7.2 and Fig. 2.11.

2.6 Types of Stimuli

In the past few years, the research interest in exploiting structural color for sensing applications has increased, and many stimuli-responsive 1DPCs have been applied as label-free sensing platforms. Generally, 1DPCs can be responsive to various stimuli of physical, chemical or biological nature, which induce a RI or thickness change of the responsive building block and lead to a shift of the photonic stopband. In contrast to the previous chapter, which was mainly focused on the different sensing mechanisms, the following subsections intend to give conceptual insights into the broad variety of different stimuli that 1DPCs can be responsive to. These will be briefly discussed along with a small selection of examples. For a broader overview of literature examples for each stimulus, the reader is referred to other reviews.[18,39,90]

2.6.1 Response to Physical Stimuli

One of the application fields of stimuli-responsive 1DPCs lies in the detection of physical stimuli, such as mechanical, thermal or electrical stimuli. In the following subsections, we will

discuss the different physical stimuli along with some examples to explain the underlying sensing principle.

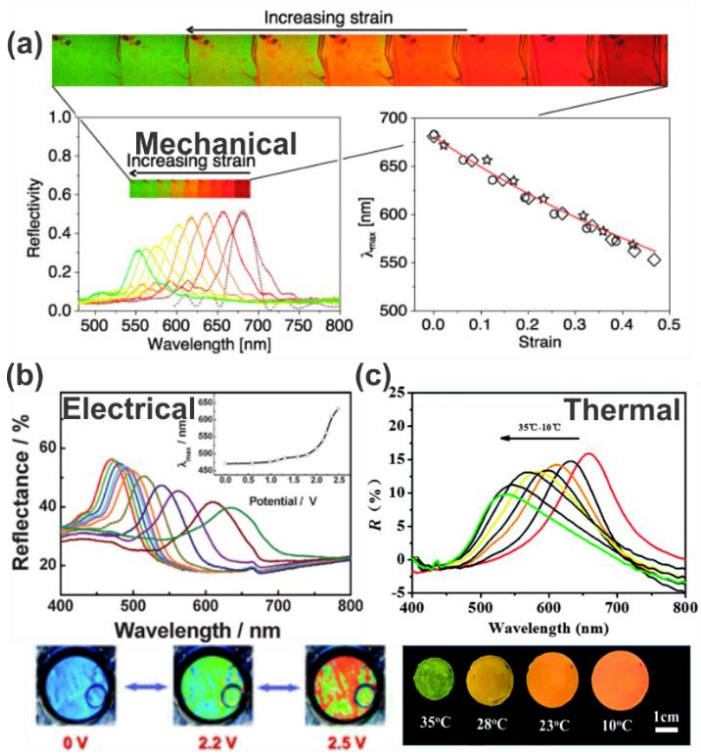

Fig. 2.8 Response of 1DPCs to different physical stimuli: (a) reversible color change induced by stretching of a 1DPC; reprinted with permission from ref. 91, Copyright 2010 Optical Society of America. (b) Reflectance spectra and photographs of electrical tuning of a 1DPC; reprinted with permission from ref. 92, Copyright 2009 Royal Society of Chemistry. (c) Reflectance spectra and photographs of a 1DPC with varying temperature; reprinted with permission from ref. 93, Copyright 2015 Royal Society of Chemistry.

2.6.1.1 Mechanical Stimuli

Mechanical stress, such as compression or stretching, is the simplest type of stimulus 1DPCs are responsive to. In 2006 the group of Ozin was the first to discover that elastomeric inverse opals (3DPCs) can be applied as mechanochromic sensors.[94] Because of the highly porous nature of the elastic inverse opal, it can easily be compressed changing the layer spacing between the air voids. This results in a gradual shift of the photonic stopband across the entire visible spectrum with increasing pressure. This work sparked the interest in using elastic polymers as building blocks for creating mechanically responsive 1DPCs. Generally, mechanical deformation is accompanied with a biaxial contraction/expansion of the polymer matrix along perpendicular directions in order to maintain a constant volume.[95] This causes changes in the RI or the lattice dimensions and therefore a shift of the photonic stopband is induced. For example, Steiner et al. demonstrated that a PC comprised of polymethylsiloxane (PDMS) and PSPI (tri-block copolymer which consists of polyisoprene containing a 22 wt-%

minority polystyrene phase) exhibits a reduction in layer thickness upon stretching, and therefore the photonic stopband is blue-shifted and can be tuned across the entire visible spectrum (from ca. 550 to 670 nm) as a function of the amount of strain (Fig. 2.8a).[91] Another mechanochromic sensor, based on a polystyrene-*b*-poly-2-vinylpyridine (PS-*b*-P2VP) di-block copolymer, was reported by Stafford and co-workers and exhibited a stopband shift from 760 to 520 nm under compressive strain from 10 to 30%.[96] Additionally, the sensor was cast into conformal coatings on nonplanar or patterned surfaces while maintaining its sensing functionality, making the application possibilities versatile. Even though the deformation and accompanied shift of the photonic stopband in mechanochromic 1DPCs is usually reversible, the long-term stability is poor and the recovery time can be comparatively long. Furthermore, the wavelength tuning range of mechanically responsive 1DPCs is dependent on the volume fraction of the polymer content and the stretching ratio (L/L0). Therefore, it is necessary to fabricate "soft" photonic crystals (with high polymer content) as they exhibit a large stopband shift (i.e. large response) under mechanical deformation.[18]

2.6.1.2 Thermal Stimuli

A change in the environmental conditions, such as a temperature change, can lead to swelling or de-swelling of 1DPCs. Therefore, the use of hydrogels, which can undergo a volume phase transition in an aqueous environment, is highly beneficial for colorimetric 1DPC temperature sensors. One of the most popular examples is the "smart" polymer poly(*N*-isopropylacrylamide) (PNIPAM), which exhibits a sharp volume phase transition around the lower critical solution temperature (LCST; ca. 32 °C). This means that the PNIPAM gel swells when the temperature is below the LCST and undergoes a dramatic collapse when the temperature is above the LCST.[97] The collapse is due to the fact that for temperatures above the LCST a transition from the hydrated (swelled) to the dehydrated (deswelled) state occurs, and thereby the hydrogel properties change from hydrophilic to hydrophobic.[98] For instance, this principle has been exploited for the fabrication of 1DPCs based on the photo-crosslinkable copolymers PNIPAM and poly(*para*-methyl styrene) (PpMS), which exhibit a color change that covers nearly the full visible spectrum when changing the temperature from 20 to 50 °C.[99] This was achieved by immersion of the sensors in water at room temperature, which leads to swelling of the PNIPAM layers and therefore a red-shift of the reflectance. Subsequent heating induced a de-swelling of the layers due to a dramatic collapse as the

temperature is increased towards the lower critical solution temperature (LCST), causing a progressive blue-shift of the stopband.

Guan et al. also made use of the volume phase transition of PNIPAM with respect to the surrounding temperature. They applied this approach for a 1DPC comprised of superparamagnetic polyvinylpyrrolidone-coated Fe_3O_4 colloidal nanocrystalline particles (Fe_3O_4@PVP CNC), which order into 1D chains when applying an external magnetic field and can be fixed and solidified in a PNIPAM gel matrix (Fig. 2.8c).[93] Due to the high RI contrast of the constituent materials, the 1DPC exhibits a bright iridescent color. During a decrease in temperature from 35 to 10 °C, the volume of the gel expands gradually and the color changes from green over yellow and orange to red. This is due to the fact that the gel matrix transforms from hydrophobic to hydrophilic with decreasing temperature, which leads to significantly increased water absorption capabilities. Therefore, a swelling of the matrix is induced, accompanied by a change in the RI and a shift of the stopband from 660 nm to 520 nm.

2.6.1.3 Electrical Stimuli

Another type of physical stimulus, which 1DPCs are responsive to, is an electric field. In general, electrically responsive 1DPCs can either be stimulated by an electrical signal or respond to an electrochemical signal. So far, most of the research in this field has been conducted with 3D photonic crystals while the number of examples for electrically tunable 1DPCs is relatively small. This may be a consequence of the lack of connectivity within the stimuli-responsive material and hence the lack of electric addressability due to the 1D architecture. Nevertheless, we highlight two examples here. One possibility for electrically responsive 1DPCs is achieved when including nematic liquid crystals as a defect layer in an SiO_2 and TiO_2-based photonic structure.[100] When an electric field is applied, the pass-band, which is caused by the defect layer, is shifted as the RI is changed due to the realignment of the liquid crystals in response to external electric fields.

Another possibility for electrically responsive 1DPCs is the response towards electrochemical signals. Examples of electrochemically responsive 1DPCs are based on the block copolymer polystyrene-*b*-poly(2-vinyl pyridine) (PS-*b*-P2VP), which exhibits swelling when an applied electric field changes the chemical environment, and therefore a full color shift of the photonic stopband is induced (Fig. 2.8b).[92,101] Precisely, the pyridine group in the P2VP block can be protonated in solution by applying an anodic bias voltage. The resulting pyridinium groups

pair with the anions of the electrolyte, which in turn are attracted to the positively charged electrode. Likewise, the reverse process occurs when applying a cathodic bias voltage. These processes enable electrical tuning of the thickness of the PV2P layers or the periodicity of the film as the application of a small voltage leads to an expansion or contraction of the layers as a function of the direction and strength of the electrical potential.

2.6.2 Response to Chemical Stimuli

Another multifaceted application of stimuli-responsive 1DPCs is the detection of chemical stimuli. These can be liquids, vapors, humidity, pH (H^+ ions) of the surrounding medium, or biomolecules. In the following subsections, we give an overview of different chemical stimuli by discussing some examples to explain the underlying sensing principle and to highlight the vast variety of possible stimuli.

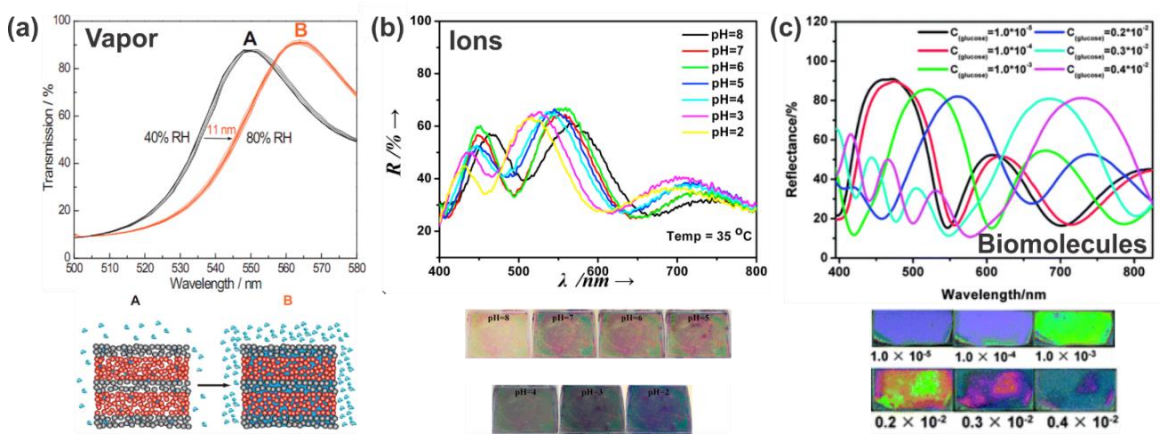

Fig. 2.9 Response of 1DPCs to different chemical stimuli: (a) relative humidity; adapted and reprinted with permission from ref. 102, Copyright 2011 American Chemical Society. (b) H^+ ions; adapted and reprinted with permission from ref. 103, Copyright 2015 Elsevier. (c) Glucose oxidase (GO_x); adapted and reprinted with permission from ref. 104, Copyright 2012 Royal Society of Chemistry.

2.6.2.1 Solvents, Liquids and Vapors

So far, much effort has been devoted to solvent, liquid and vapor sensing due to the quick and large response as well as facile readout of the 1DPCs. A large library of active components, such as porous nanoparticles,[60,65] nanosheets,[25,75] polymers,[24,105] clays,[81,106] MOFs[63] or zeolites[107] has been explored and diverse liquids, organic solvents, VOCs or humidity (Fig. 2.9a) have been applied as analytes. Depending on the active component used, the sensing principle predominantly relies on RI or thickness changes, which translates into a shift of the photonic stopband. Furthermore, the 1DPCs can function as a "photonic nose" by creating an array of PCs, in which each component is functionalized to respond to a different analyte.[67]

The applications for this class of responsive 1DPCs are widespread and range from environmental monitoring,[102] *via* water and food quality contro[l4] to medical diagnostics.[67] To our mind the field of vapor sensing is highly promising for future applications and should further be investigated. Therefore, a more detailed discussion of selected examples of 1DPCs used for vapor sensing is given in Chapter 2.7, which is why we keep the discussion short at this point.

2.6.2.2 Ions

Another possibility for chemical responsiveness of 1DPCs is the response towards pH or ions. Ion responsiveness in 1DPCs is commonly based on the interaction of analyte ions with a certain recognition group of a hydrogel polymer leading to an altered Donnan osmotic pressure.[18] Therefore, a volume change of the hydrogel takes place, which is driven by solvent influx in order to compensate the osmotic pressure.[103] Since this process leads to a swelling or shrinking of the polymer component, a shift of the photonic stopband is induced. For example, Ge and co-workers demonstrated pH-responsiveness in the range from 8 to 2 at a temperature of 35 °C (Fig. 2.9b) by incorporating a proton-sensitive co-polymer such as poly(acrylic acid-*N,N*'-methylene-bis-acrylamide-*N*-isopropylacrylamide) P(AA-bis-NIPAAm) as active material in a 1DPC.[103] Upon solvent influx, the uptake of H^+ results in electrostatic repulsion in the polymer. The more water infiltrates the 1DPC, the lower the RI of the swollen polymer, leading to a shift in PBG from 575 nm to 510 nm. From the reflectance spectra, it seems that all tested pH values can be distinguished in a proper manner except for pH 6 and 7, which show similar stopband positions.

Another example of ion detection with polymer-based 1DPCs is the use of a polydimethylaminoethyl methacrylate-*co*-ethylene glycol dimethacrylate (PDMAEMA-*co*-PEGDMA) and TiO_2-based BS, which is responsive to thiocyanate anions (SCN^-). Immersion in citric acid leads to a red-shift of the stopband due to swelling of the quaternized polymer and the decrease of its RI. Upon exposure towards SCN^- (concentrations from 10^{-6} mol l^{-1} to 10^{-1} mol l^{-1}) a blue-shift of the PBG is observed (750 nm to 490 nm) caused by a volume collapse due to weakened electrostatic repulsion in the polymer layers.[39,108] Further, the sensor exhibits a high selectivity towards the detection of SCN^- as the assay is barely influenced by the presence of other, interfering anions (F^-, Cl^-, Br^-, I^-, HPO_4^{2-}, Ac^- and HCO_3^-). Despite the fact that there are various other possibilities for sensing ions or pH, stimuli-responsive 1DPCs may offer a platform for miniaturized sensors for specific applications.

2.6.2.3 Biomolecules

Even though most biomolecules are too large to be reasonably detected by 1DPCs, we discuss a few examples in this subsection that show that chemically responsive 1DPCs can also be designed to detect biologically relevant molecules. This is achieved either directly by including an appropriate recognition group into the structure, or indirectly *via* changes in the environment such as the pH, triggered by the interaction of the analyte with the photonic structure. For example, the catalytic oxidation of glucose in the presence of glucose oxidase (GO_x) can be monitored as pH changes occur due to the gluconic acid, which is generated during the reaction. 1DPCs based on poly(*N*,*N*' -dimethylaminoethyl methacrylate) (PDMAEMA) and TiO_2 are able to detect the concentration of GO_x, since the polymer is pH-sensitive and shrinks or swells in response to the produced gluconic acid, and hence leads to a shift of the photonic bandgap (Fig. 2.9c).[104] Furthermore, surface functionalization of mesoporous 1DPCs based on TiO_2- and SiO_2-nanoparticles with biotin allows for the optical detection of probe-target interactions with streptavidin, whereby the response relies on the change in the dielectric constant due to the bio-recognition event. Interestingly, confocal fluorescence microscopy has shown that the streptavidin diffused to deeper layers of the mesoporous 1DPC instead of staying on the surface. Therefore, future research should focus on the diffusion of molecules within 1DPCs in order to gain a deeper knowledge on how to exploit stimuli-responsive 1DPCs for an even wider range of applications.

2.7 Selected Vapor Sensing Applications

In the previous chapters, the various types of stimuli that can be detected with 1DPCs have been discussed on a conceptual level. Since vapor sensing is one of the largest application fields of stimuli-responsive 1DPCs and has received increasing attention in the past few years, the next section focuses on this stimulus in more detail by reviewing selected examples. To structure this discussion, the examples of vapor-responsive 1DPCs are grouped by their architecture being either nanoparticle-based PCs, defect structures, or hybrid photonic structures.

2.7.1 NP-based 1DPCs

For porous nanoparticle-based 1DPCs, which are often comprised of SiO_2 and TiO_2 particles, the vapor sensing capabilities regarding humidity,[66,102,109] toluene[60,109] and isopropanol[66,110,111] have been studied. The main reasons for the popularity of this system is its inexpensive and easy fabrication as well as the broad tunability of the optical properties deriving from

properties on the macroscopic, mesoscopic and atomic scale.[109] Therefore, the optical response towards environmental changes can be precisely tailored to meet the desired application. These types of 1DPCs are not only sensitive to a certain vapor, but they can also distinguish specific relative vapor pressures of the analyte.[60,66,111] For example, this was studied by Kobler et al. for 1DPCs based on mesoporous SiO_2 and TiO_2 nanoparticles that exhibit a response towards different vapor pressures of toluene due to changes in the RI, which gives rise to optical adsorption isotherms.[60]

Some 1DPCs are not only stimuli-responsive, but their responsiveness can be changed and fine-tuned by post-synthetic functionalization or intercalation. For example, it has been shown that porous 1DPCs based on alternating layers of SiO_2 and TiO_2 NPs can be employed as "artificial nose" for the detection of bacteria, which are commonly involved in cases of opportunistic hospital infections.[67] Bonifacio et al. demonstrated that surface functionalized 1DPC sensor arrays, combined with color image analysis, could be used to identify different bacterial strains (Pseudomonas aeruginosa, Escherichia coli, Staphylococcus aureus, and Staphylococcus epidermidis) by analyzing the headspace created by them (Fig. 2.10). When cultivated in 5% sheep blood agar for 24 h, each bacteria strain produces a unique composition of volatile species. Even though the amount of volatiles produced by the bacteria is small, the culture headspace shows a distinct atmosphere composition, which is made up of agar volatiles along with the bacteria culture by-products, and therefore enables the unambiguous distinction of the different bacteria strains. The volatile metabolites of bacteria strains can contain alcohols, sulfides, amines, and aldehydes, among others. A detailed study on the composition of the headspace of some bacteria strains can be found elsewhere.[112] Due to the differently functionalized sensors in the array, the headspace of the studied bacteria strains can be distinguished by PCA analysis. Even though there are many examples of nanoparticle-based 1DPCs used for vapor sensing, the relative optical shift of the stopband of these 1DPCs is intrinsically limited as the optical response relies mainly on the change of RI upon analyte infiltration. It is thus key to implement suitable image or multivariate analysis to discriminate chemically similar analytes in a sufficient manner.

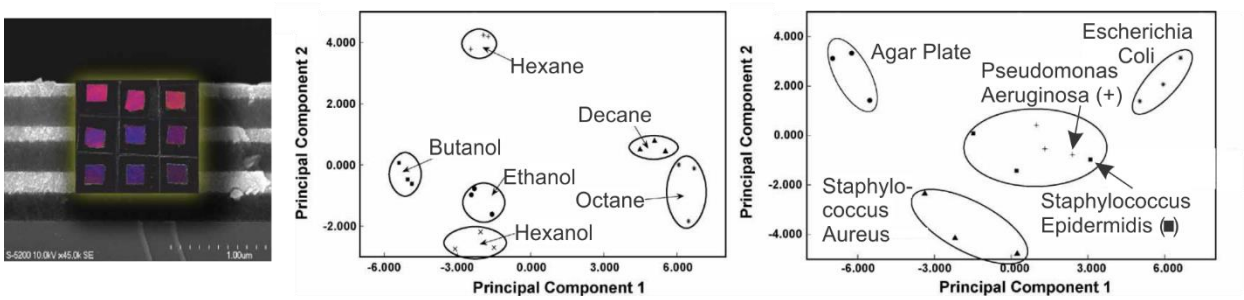

Fig. 2.10 Principal component analysis of color changes resulting from the exposure of a 1DPC-based photonic-nose array to different analyte-saturated atmospheres (middle) as well as color changes caused by the volatiles produced by bacteria strains (right); adapted and reprinted with permission from ref. 67, Copyright 2010 John Wiley and Sons.

2.7.2 Defect 1DPCs

In order to overcome the drawbacks of nanoparticle-based 1DPCs, the inclusion of a defect layer or the fabrication of hybrid 1DPCs to increase the resolution has received attention in the past few years. Exemplarily, analytes reported for defect 1DPCs range from protic (e.g. humidity,[85] ethanol (Fig. 2.11a),[87] isopropanol[66,88]) to aprotic solvent vapors such as toluene.[88] The underlying sensing mechanism of defect 1DPCs was discussed in more detail in Section 2.5.3. As mentioned previously, one possibility for defect layers is the fabrication of a thicker layer of one of the constituent materials in the middle of the 1DPC in order to break its symmetry. This approach was utilized by the group of Miguez for the fabrication of a mesoporous TiO_2- and SiO_2-based 1DPC in which a five times thicker SiO_2 layer was embedded in the middle of the otherwise periodic photonic structure (Fig. 2.11a).[66] In their work they gave a detailed analysis of the response of such a defect 1DPC towards isopropanol (Fig. 2.11a left) and water (Fig. 2.11a right) vapors with partial pressures from 0 to 1 along with the comparison of the response of the 1DPC without the defect layer. In accordance with the theoretical details discussed in Section 2.5.3, it is evident that the resolution of the defect-containing PC is higher due to the thin reflectance dip compared to the broad stopband of the normal 1DPC.

Another option for creating defect 1DPCs is the inclusion of other responsive materials such as nanosheets, dyes or nanophosphors (Fig. 2.11b and c).[85,88] For example, responsiveness towards isopropanol and toluene vapors has been demonstrated for a TiO_2- and SiO_2-based BS with rhombic-shaped Eu-doped nanophosphors embedded in the middle of the structure (Fig. 2.11b).[88] In this case, the infiltration of the BS' voids with the analyte, and hence the optical response of the photonic structure towards a vapor, causes a strong modification of

the luminescence spectrum of the nanophosphors. Note that the nanophosphors were embedded in a protective matrix to avoid interaction with the vapors. Upon increasing the partial vapor pressure, the average RI of the BS is increased due to adsorption and/or condensation of the high RI vapor in the pore walls, which results in a gradual red-shift of the resonant mode (Fig. 2.11b gray). Therefore, the intensity of the emission peak of the nanophosphor (Fig. 2.11b red) is slowly decreased because the match with the resonant mode is diminished. The higher the refractive index of the absorbed vapor, the larger the shift of the position of the resonant mode, which leads to a more abrupt drop of the emission peak intensity of the nanophosphor. Hence, this study showed that the luminescence spectra of the embedded nanophosphors are sensitive to the degree of matching with the resonant mode, and that the variations depend on the RI of the analyte, which implies selectivity of the response.

Additionally, the inclusion of a defect layer in a stimuli-responsive 1DPC opens up new possibilities in terms of readout scheme. For example, the integration of a light-emitting dye (polystyrene nanospheres dyed with Firefli Fluorescent Red) in the defect layer of a humidity-responsive PC (Fig. 2.11c) allows the creation of a tailored photoluminescence response to changes in ambient humidity.[85] Specifically, antimony phosphate nanosheets were used as a stimuli-responsive defect layer in a TiO_2 and SiO_2-based 1DPC, as they exhibit pronounced swelling upon exposure to humidity. When the nanosheet layer shows gradual swelling in response to increased humidity, the spatial and spectral positions of the reflectance dip are changed with respect to those of the emission band of the dye molecules. In this case two different scenarios can be realized, namely the *turn-on* or *turn-off* response of the luminescence of the dyes with increasing humidity. However, in the present state, the range of solvent vapors that has been detected with defect 1DPCs is still quite small.

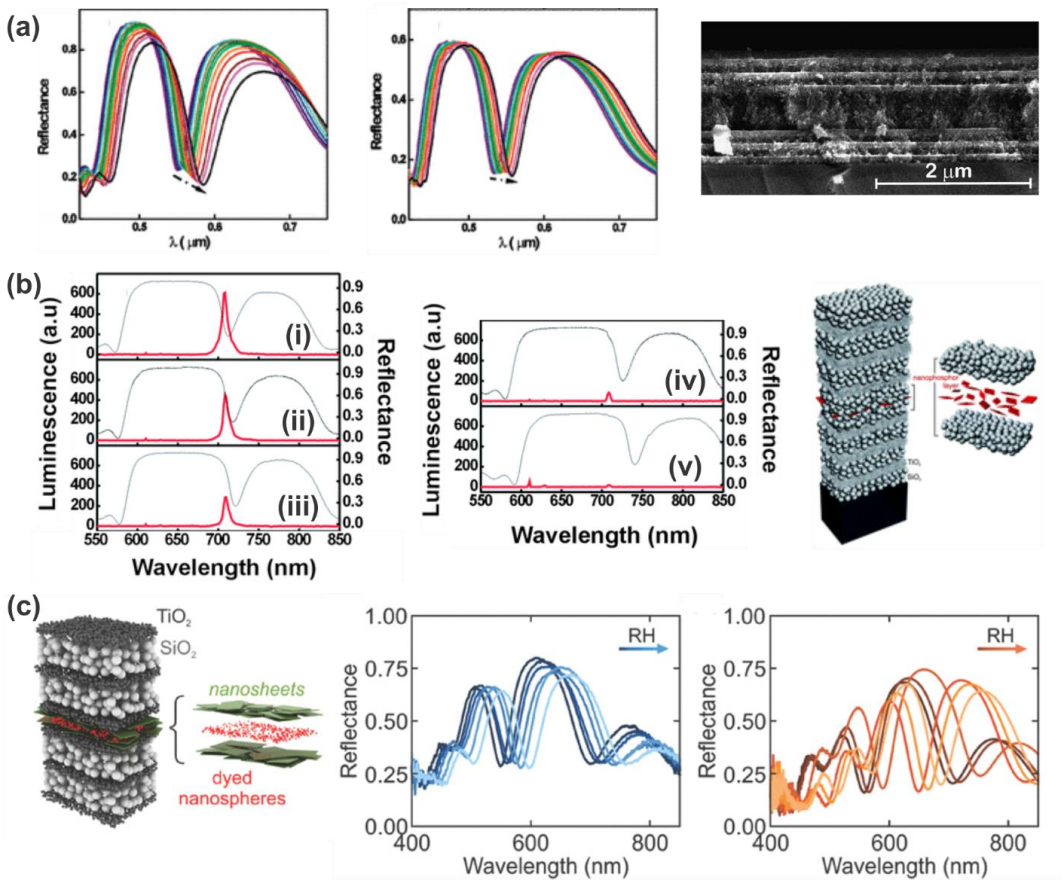

Fig. 2.11 (a) Optical response and cross-section FE-SEM image of a 1DPC with a planar defect towards different partial pressures of isopropanol (left) and water (right) vapors, respectively. The arrows indicate the increase in the vapor partial pressure from 0 to 1; adapted and reprinted with permission from ref. 66, Copyright 2008 American Chemical Society. (b) 1DPC containing a nanophosphor layer as a defect and its response (luminescence (red) and reflectance (gray)) towards different partial pressures of isopropanol vapor: (i) before exposure (ii-v) at increasing partial pressure; adapted and reprinted with permission from ref. 88, Copyright 2010 Royal Society of Chemistry. (c) 1DPC with a defect layer comprised of dyed nanospheres embedded in a nanosheet layer shows increased response towards relative humidity when the dye is in the "turn-on" state (orange); adapted and reprinted with permission from ref. 85, Copyright 2017 John Wiley and Sons.

2.7.3 Hybrid 1DPCs

A much wider range of applicable solvent vapors has been reported for hybrid 1DPCs, which combine the advantages of metal oxide NPs as RI contrast material, such as TiO_2 and SiO_2, with materials that show response towards various analytes. As the library of responsive materials is vast, this opens up the opportunity to judiciously fine-tune the 1DPC to meet specific requirements, and the possibility to distinguish between different vapors. For example, 1DPCs comprised of TiO_2 NPs and MOFs are promising candidates for selective vapor sensing due to their modular tunability, strong host–guest interactions, and tailorable sorption behavior at the molecular level.[62] The first MOF-based 1DPC was reported by Hinterholzinger

et al. and made use of ZIF-8 as active component.[62] The studied vapors included MeOH, EtOH, iso-butanol and *tert*-pentanol. Later, the analyte-specific optical detection was enhanced by Ranft et al. by integrating multiple responsive MOF species (ZIF-8, CAU-1-NH_2, HKUST-1) into a single 1DPC, whereby the response towards MeOH, EtOH, water, 2-propanol, 1-hexanol and mixtures was examined (Fig. 2.12d).[63] The analyte discrimination capability in CAU-1 based 1DPCs was enhanced by post-assembly modification of the coordination environment of the metal-oxo secondary building unit or by amide-formation at the organic linker, which translates into significant changes in the optical response of the photonic crystal sensor towards the analytes (Fig. 2.12c).[113] In this case, the used vapors were MeOH, EtOH, water, iso-propanol and heptane. As discussed in Section 2.5, a change in layer thickness upon exposure towards a stimulus leads to much larger optical shifts than a response based on RI changes. Therefore, the use of flexible MOFs such as NH_2-MIL-88B, which show a pronounced "breathing effect" upon exposure to environmental vapors (MeOH, EtOH, water, iso-propanol, DMF, acetone and EtOH/water mixture), is beneficial for obtaining large optical shifts up to 200 nm (Fig. 2.12b).[83]

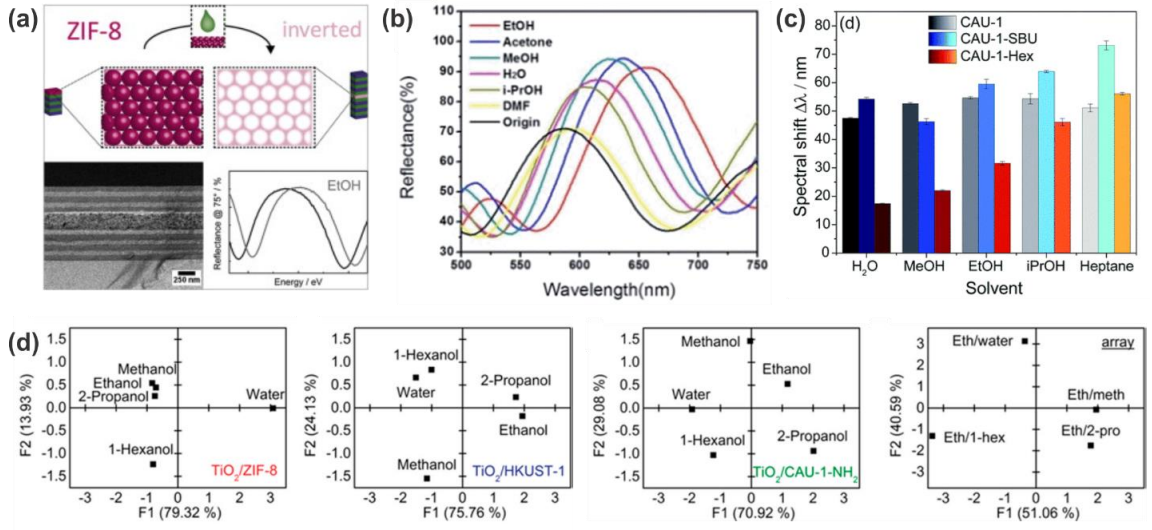

Fig. 2.12 (a) Stimuli-responsive MOF defect layer incorporated in a 1DPC for enhanced sensitivity towards EtOH vapor; adapted and reprinted with permission from ref. 87, Copyright 2015 Elsevier. (b) Selective vapor sensing through a "breathing" MOF in the 1DPC; adapted and reprinted with permission from ref. 83, Copyright 2014 Royal Society of Chemistry. (c) Different spectral shifts upon analyte exposure for modified MOF building units in 1DPCs; adapted and reprinted with permission from ref. 113, Copyright 2018 Royal Society of Chemistry. (d) Principal component analysis (PCA) of 1DPCs for differently responsive MOF species (TiO_2/ZIF-8, TiO_2/HKUST-1, and TiO_2/CAU-1-NH_2) as active components and an array assembled from these three MOF-based BSs illustrating the combinatorial capability for discriminating between solvent vapor mixtures; adapted and reprinted with permission from ref. 63, Copyright 2015 American Chemical Society.

Even larger optical shifts in response to vapors have been obtained in hybrid 1DPCs built from metal-oxide NPs and nanosheets such as $HSbP_2O_8$, $H_3Sb_3P_2O_{14}$ or $Li_2Sn_2S_5$ due to their pronounced swelling capability upon analyte exposure. Preceding work on the influence of relative humidity on the stacking distance of the layered bulk antimony phosphates revealed that the phosphatoantimonic acids can intercalate a larger amount of water at ambient RH than their potassium counterparts.[114] Specifically, in the $HSbP_2O_8$ bulk material proton diffusion behaves like a particle hydrate, while in the $H_3Sb_3P_2O_{14}$ ⋅ x H2O bulk it behaves like a true lattice hydrate.[114] Inspired by this work, ellipsometric studies of the RH dependent swelling of these materials in nanosheet-based thin films were carried out.[76] These studies showed that in the thin film case the materials exhibit a smoother, less stepwise swelling upon exposure to RH compared to the bulk material, which is highly beneficial for application of this material in sensing. This effect can be attributed to a lower layer registry and less interlayer interactions in the restacked nanosheet material compared to the crystalline bulk material, and to increased grain boundary adsorption. Taking into account the turbostratic disorder of the nanosheets, the water adsorption sites between the nanosheets are less well-defined compared to the bulk, leading to a smoother, continuous water uptake rather than the formation of defined hydrates.[76] Inspired by the unprecedentedly large swelling capabilities of antimony phosphate nanosheet thin films, paired with the fast sub-second to few seconds response times, 1DPCs with $H_3Sb_3P_2O_{14}$ and either TiO_2 or SiO_2 were fabricated. In this case, the $H_3Sb_3P_2O_{14}$ acts as the moisture-sensitive component while the nanoparticle layers are a "gate", due to their textural porosity, providing access of the water molecules to the sensing component throughout the whole photonic structure.[65,76]

Even though $HSbP_2O_8$ also exhibits extraordinary swelling capabilities, the main difference to $H_3Sb_3P_2O_{14}$ is that it loses water completely at zero humidity and therefore shows better contrast and thus superior sensitivity in the low humidity regime.[75] This behavior originates from the differences in the crystal structure of these materials. While $H_3Sb_3P_2O_{14}$ exhibits structural pores that can host water molecules within the layers, the $HSbP_2O_8$ layers are dense. A photonic nose based on $HSbP_2O_8$ nanosheets and TiO_2 was developed (Fig. 2.13b), which allows trace water sensing and vapor recognition of alcohol/water mixtures, MeOH, EtOH, water, propanol, iso-propanol, butanol, 2-butanol, acetonitrile, toluene and heptane.[75] Hereby, the sensor can distinguish between water vapor, nonprotic (nonpolar and polar) and protic solvent vapors (alcohols) by exploiting the saturation time and optical shift as two independent

descriptors. Even chemically similar solvent vapors such as homologous alcohols or isomers, which interact with the nanoparticle layers as well as the nanosheet layers of the 1DPC, can be distinguished based on their sorption and diffusion properties.[75]

Another interesting application is the exploitation of the giant moisture responsiveness of $H_3Sb_3P_2O_{14}$ and TiO_2 or SiO_2 1DPCs for touchless optical finger motion tracking (Fig. 2.13a) due to the fast intercalation of the humidity close to the finger into the nanosheet layers and the resulting optical shift.[76] In a recent publication, we demonstrated that this specific 1DPC could be transferred to arbitrary substrates (Fig. 2.13c) with the aid of a sacrificial layer without impairing the vapor sensing capability. In addition, it was shown that the sensing properties can be flexibly changed and fine-tuned through modification with various primary alkylamines.[115] Particularly, this allows to flexibly fine-tune the hydrophobicity of the sample and therefore the response towards VOCs.[115] Even though the fine-tuning of the sensing properties of 1DPCs has not received extensive attention so far, we believe that there is high potential for future research. As there is a wide variety of literature concerning intercalation in layered (nano)materials, this may open up the opportunity of judiciously creating stimuli-responsiveness and tunability in inherently non-responsive building blocks.

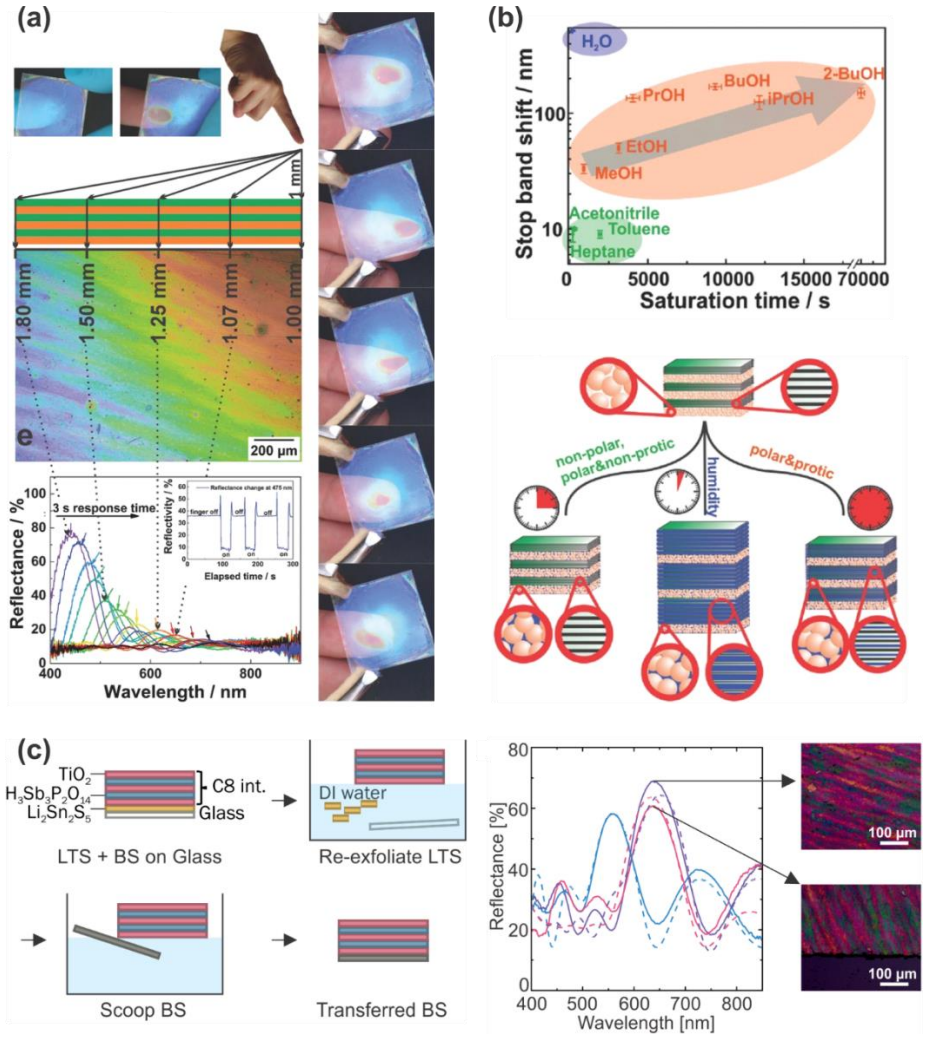

Fig. 2.13 (a) 1DPC with giant moisture responsiveness used as a touchless positioning interface by responding to the moisture of a finger; adapted and reprinted with permission from ref. 76, Copyright 2015 John Wiley and Sons. (b) 1DPC acting as a photonic nose: analyte identification of different solvent vapors by different sensing mechanisms; adapted and reprinted with permission from ref. 75, Copyright 2016 John Wiley and Sons. (c) Left: Schematic description of the transfer of a vapor sensitive 1DPC to another substrate by hydrophobization of the sample (amine intercalation) and the use of a sacrificial layer. Right: Reflectance of the pristine (blue), hydrophobized (purple) and transferred (pink) sample along with the calculated reflectance (dashed lines) and microscope images of the sample before and after transfer; adapted and reprinted with permission from ref. 115, Copyright 2021 The Authors.

To the best of our knowledge, the highest reported RI contrast in 1DPCs was achieved in a hybrid BS which combined $Li_2Sn_2S_5$ nanosheets with SiO_2 nanoparticles.[25] In combination with the excellent swelling capability of the nanosheets upon exposure to humidity, this device bodes well for a new generation of humidity sensors with extremely high sensitivity.

In this chapter, we highlighted some vapor sensing applications of stimuli-responsive 1DPCs taking into account the different analytes that have been studied as well as the various materials that are suitable and different 1DPC architectures that are applicable. In terms of sensitivity,

we anticipate that future research (not only in the field of vapor sensing) will focus on hybrid 1DPCs due to their often superior swellability or combination of sensing mechanisms, and thus larger optical shifts. In addition, unleashing new stimuli-responsive materials for sensor integration holds great potential due to the vast variety of building blocks, chemical properties and responsiveness.

2.8 Current challenges of 1DPC sensors

Although many groups have focused on the architectures, techniques and materials in the field of 1DPC sensing, there are still several challenges limiting the performance of 1DPC-based sensors at the current state. These challenges emerge partly from the sensing field in general and are partly related specifically to 1DPCs.

For example, the miniaturization, which is highly desired for emerging application fields such as IoT, point of care testing, or wearables, is an important aspect for both 1DPCs and the corresponding readout systems. While 1DPCs can easily be fabricated in small size, the miniaturization of the readout system remains challenging because quantitative measurements often rely on microscopic or spectroscopic techniques that require large and non-portable setups. A promising option to overcome this drawback is either the qualitative detection based on color changes induced through the sensing event, or building a readout platform that is based on handheld devices such as smartphones. By integrating the zoom function of the camera and systems for optical analysis, colorimetric as well as fluorescence detection may be achieved thus rendering PCs a versatile sensing platform.[116]

Regarding the challenges specifically related to 1DPCs,[90,117] the key issues that need to be addressed to make them competitive with other sensor types are summarized schematically in Fig. 2.14. These parameters, also referred to as the "4S", include the sensitivity (Fig. 2.14a), selectivity (Fig. 2.14b), stability (Fig. 2.14c) and speed (response-recovery rate; Fig. 2.14d).[118]

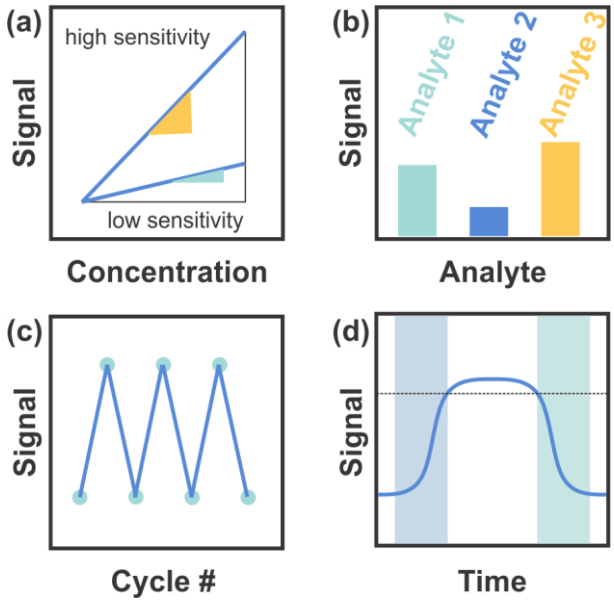

Fig. 2.14 (a) Sensitivity of the sensor based on the slope definition and the maximum sensitivity. (b) Selectivity of the sensor towards different analytes. (c) Stability of the sensor based on the number of cycles conducted. (d) Response (blue square) and recovery (green square) times. Figure adapted and reproduced from ref. 119.

2.8.1 Sensitivity

In Fig. 2.14a the sensitivity – i.e. the measurement signal change per concentration unit of the analyte (slope definition) – is schematically depicted in accordance with the slope definition of the maximum sensitivity for a sensor with high (yellow) and low (green) sensitivity. Colorimetric 1DPC-based sensors that make use of RI changes as the main sensing mechanism often exhibit a stopband-shift of a few nanometers upon analyte infiltration at best, which makes a naked-eye-readout difficult. This can be improved with larger changes in the photonic stopband, e.g. by applying materials that show a large change in layer thickness, along with RI changes, in response to a stimulus. In these sensors, the sensitivity is enhanced and therefore future research should be directed in finding materials with pronounced swelling capability.

2.8.2 Selectivity

An example of the differentiating capability, and therefore the selectivity of a sensor towards different analytes, is given in Fig. 2.14b. A general issue in the field of sensing is the selectivity and cross sensitivity towards chemically similar analytes as the sensors are not labelled with recognition groups and often solely distinguish different analytes by RI and polarity. This shortcoming can be alleviated by means of statistical data analysis, e.g. principal component analysis (PCA) of sensor arrays,[4,63,67] or hierarchical sensor structures.[120] The functionalization

of the sensor with chemically selective recognition groups as well as the application of building blocks with inherent chemical selectivity might also help overcome this issue.

2.8.3 Stability

The sensor stability defines how long and throughout how many cycles the sensor maintains its performance, which is depicted schematically in Fig. 2.14c. Issues regarding the sensor stability include chemical stability, long-term stability and cyclability. For example, the sensor can undergo irreversible changes during the sensing event, or storage may affect the sensing performance, both of which is impracticable for long-term applications. Enhanced stability could be controlled, for example, by a careful choice of the building blocks (i.e. inorganic vs. organic materials) or morphology (e.g. active material with textural or structural porosity) of the sensor. Quite generally, the use of robust inorganic materials may lead to an improved chemical and long-term stability as compared to polymers.

2.8.4 Speed

Per definition, the speed of a sensor, i.e. the response and recovery times, is characterized by the times needed to achieve 90% of the signal change. This is illustrated in Fig. 2.14d, whereby the dotted line marks 90% of the signal change and the blue and green squares show the response and recovery times, respectively. As required by the desired application, swellable nanosheets with response times in the second to sub-second regime may be favored as functional building blocks for 1DPCs as compared to swellable polymers that typically exhibit response times in the range of up to several tens of minutes.

Lastly, the optimization of existing materials regarding the homogeneity of the particles (in terms of e.g. size, morphology, and phase purity), and the layer thicknesses as well as their surface roughness should be improved as these factors give rise to color purity and hence an improved color resolution of the sensor. This in turn facilitates the discrimination of analytes that only induce small shifts of the photonic stopband and may pave the way for continuous monitoring of physical, chemical or biochemical stimuli.

2.9 Summary and Outlook

In this review, we have summarized the materials and principles for the design and fabrication of 1DPCs. The main fabrication methods rely on liquid processing and evaporation-induced self-assembly of the constituent materials without the need for expensive instrumentation or delicate processing conditions. Moreover, a large library of materials is available for the

fabrication of 1DPCs including nanoparticles, polymers, nanosheets, MOFs and zeolites. However, in order to transfer the materials and fabrication methods from research to industry, large-scale manufacturing needs to be improved tremendously. At the same time, the optical properties of PCs can be judiciously tuned based on theory-guided optical design. Hence, stimuli-responsiveness can be introduced rationally and translated into a visibly perceptible color change of the PC. Hereby, two different sensing mechanisms are possible based on the active component: change of RI or change of layer thickness. Since the RI changes are intrinsically limited, the use of 1DPC sensors that are based on layer thickness changes are favorable as the relative shift of the photonic stopband is more pronounced in this case. The main advantages of 1DPC sensors is their low cost and ease of readout. The response types can be divided into response towards physical or chemical stimuli, whereby we highlighted various examples of 1DPCs for each case. Furthermore, we introduced selected applications for 1DPCs in the field of vapor sensors, as we believe that this is a field with a bright future owing to the rapidly increased need for cheap and label-free sensor systems. In particular, different 1DPCs have been applied as "artificial noses" to detect humidity, explosives, toxic volatiles, or metabolic products. Finally, we provided an overview of several challenges that remain in 1DPC sensors, some of which stem from the sensing field in general and some of which are specific to 1DPCs.

Given the importance of sensors in our everyday life, photonic crystal based sensors represent a highly promising, low-cost technology for smart next-generation sensors, particularly regarding their subtle response to the environment for ambient monitoring and point-of-care applications. To achieve real-world applications in the near future it is of utmost importance to foster collaborative innovation from different research communities.

2.10 Conflict of Interest

There are no conflicts to declare.

2.11 Acknowledgements

Financial support was granted by the Max Planck Society, the University of Munich (LMU), the Center for Nanoscience and the Cluster of Excellence e-conversion. A. Jiménez-Solano gratefully acknowledges a postdoctoral scholarship from the Max Planck Society and the Spanish Ministry of Universities for funding through a Beatriz Galindo Research fellowship BG20/ 00015. Open Access funding provided by the Max Planck Society.

2.12 References

1. X. Guo, D. Kuang, Z. Zhu, Y. Ding, L. Ge, Z. Wu, B. Du, C. Liang, G. Meng, Y. He, *ACS Appl. Nano Mater.* **2021**, *4*, 11159.
2. S. Su, W. Wu, J. Gao, J. Lu, C. Fan, *J. Mater. Chem.* **2012**, *22*, 18101.
3. F. Wang, Z. Meng, F. Xue, M. Xue, W. Lu, W. Chen, Q. Wang, Y. Wang, *Trends Environ. Anal. Chem.* **2014**, *3-4*, 1.
4. L. D. Bonifacio, G. A. Ozin, A. C. Arsenault, *Small* **2011**, *7*, 3153.
5. Y. Lu, S. Peng, D. Luo, A. Lal, *Nat. Commun.* **2011**, *2*, 578.
6. Y. Guo, M. Zhong, Z. Fang, P. Wan, G. Yu, *Nano Lett.* **2019**, *19*, 1143.
7. C. Liu, B. Zhang, W. Chen, W. Liu, S. Zhang, *TrAC, Trends Anal. Chem.* **2021**, *143*, 116334.
8. X. Wu, T. Chen, Y. Chen, G. Yang, *J. Mater. Chem. B* **2020**, *8*, 2650.
9. E. C. Nelson, N. L. Dias, K. P. Bassett, S. N. Dunham, V. Verma, M. Miyake, P. Wiltzius, J. A. Rogers, J. J. Coleman, X. Li, P. V. Braun, *Nat. Mater.* **2011**, *10*, 676.
10. R. A. Potyrailo, *Chem. Soc. Rev.* **2017**, *46*, 5311.
11. H. Ji, W. Zeng, Y. Li, *Nanoscale* **2019**, *11*, 22664.
12. U. Guth, W. Vonau, J. Zosel, *Meas. Sci. Technol.* **2009**, *20*, 042002.
13. X. Liu, S. Cheng, H. Liu, S. Hu, D. Zhang, H. Ning, *Sensors* **2012**, *12*, 9635.
14. S. H. Cho, J. M. Suh, T. H. Eom, T. Kim, H. W. Jang, *Electron. Mater. Lett.* **2021**, *17*, 1.
15. D.-H. Kim, J.-H. Cha, J. Y. Lim, J. Bae, W. Lee, K. R. Yoon, C. Kim, J.-S. Jang, W. Hwang, I.-D. Kim, *ACS Nano* **2020**, *14*, 16907.
16. T. Wang, Y. Guo, P. Wan, X. Sun, H. Zhang, Z. Yu, X. Chen, *Nanoscale* **2017**, *9*, 869.
17. X. Wang, Y. Li, X. Li, J. Yu, S. S. Al-Deyab, B. Ding, *Sens. Actuators B* **2014**, *203*, 333.
18. J. Ge, Y. Yin, *Angew. Chem., Int. Ed.* **2011**, *50*, 1492.
19. Z. Cai, N. L. Smith, J.-T. Zhang, S. A. Asher, *Anal. Chem.* **2015**, *87*, 5013.
20. Z. Cai, X. Xu, Z. Meng, B. Rafique, R. Liu, *Functional Materials from Colloidal Self-Assembly*, Wiley-VCH, Weinheim, Germany, **2022**.
21. P. Ganter, B. V. Lotsch, *Mol. Syst. Des. Eng.* **2019**, *4*, 566.
22. S. G. Johnson, J. D. Joannopoulos, J. N. Winn, R. D. Meade, *Photonic Crystals: molding the flow of light*, Princeton University Press, Princeton, NJ, USA, **2011**.

23. M. E. Calvo, H. Míguez, Responsive Photonic Nanostructures: Smart Nanoscale Optical Materials, The Royal Society of Chemistry, **2013**.

24. Y. Kang, J. J. Walish, T. Gorishnyy, E. L. Thomas, *Nat. Mater.* **2007**, *6*, 957.

25. K. Szendrei-Temesi, O. Sanchez-Sobrado, S. B. Betzler, K. M. Durner, T. Holzmann, B. V. Lotsch, *Adv. Funct. Mater.* **2018**, *28*, 1705740.

26. G. von Freymann, V. Kitaev, B. V. Lotsch, G. A. Ozin, *Chem. Soc. Rev.* **2013**, *42*, 2528.

27. A. Biswas, I. S. Bayer, A. S. Biris, T. Wang, E. Dervishi, F. Faupel, *Adv. Colloid Interface Sci.* **2012**, *170*, 2.

28. M. Qian, X. Q. Bao, L. W. Wang, X. Lu, J. Shao, X. S. Chen, *J. Cryst. Growth* **2006**, *292*, 347.

29. A. Altoukhov, J. Levrat, E. Feltin, J.-F. Carlin, A. Castiglia, R. Butte´, N. Grandjean, *Appl. Phys. Lett.* **2009**, *95*, 191102.

30. G. A. Ozin, K. Hou, B. V. Lotsch, L. Cademartiri, D. P. Puzzo, F. Scotognella, A. Ghadimi, J. Thomson, *Mater. Today* **2009**, *12*, 12.

31. C. J. Brinker, Y. Lu, A. Sellinger, H. Fan, *Adv. Mater.* **1999**, *11*, 579.

32. S.-Y. Zhang, M. D. Regulacio, M.-Y. Han, *Chem. Soc. Rev.* **2014**, *43*, 2301.

33. C. Zhao, L. Xing, J. Xiang, L. Cui, J. Jiao, H. Sai, Z. Li, F. Li, *Particuology* **2014**, *17*, 66.

34. R. D. Deegan, O. Bakajin, T. F. Dupont, G. Huber, S. R. Nagel, T. A. Witten, *Nature* **1997**, *389*, 827.

35. A. Kaliyaraj Selva Kumar, Y. Zhang, D. Li, R. G. Compton, *Electrochem. Commun.* **2020**, *121*, 106867.

36. D. P. Puzzo, L. D. Bonifacio, J. Oreopoulos, C. M. Yip, I. Manners, G. A. Ozin, *J. Mater. Chem.* **2009**, *19*, 3500.

37. M. E. Calvo, O. Sánchez-Sobrado, S. Colodrero, H. Míguez, *Langmuir* **2009**, *25*, 2443.

38. T. Komikado, A. Inoue, K. Masuda, T. Ando, S. Umegaki, *Thin Solid Films* **2007**, *515*, 3887.

39. H. Shen, Z. Wang, Y. Wu, B. Yang, *RSC Adv.* **2016**, *6*, 4505.

40. J. Zhu, M. C. Hersam, *Adv. Mater.* **2017**, *29*, 1603895.

41. Z. Wu, D. Lee, M. F. Rubner, R. E. Cohen, *Small* **2007**, *3*, 1445.

42. A. Jiménez-Solano, J. F. Galisteo-López, H. Míguez, *Adv. Opt. Mater.* **2018**, *6*, 1700560.

43. C. Inui, Y. Tsuge, H. Kura, S. Fujihara, S. Shiratori, T. Sato, *Thin Solid Films* **2008**, *516*, 2454.

44. X. Yu, W. Ma, S. Zhang, *Dyes Pigm.* **2021**, *186*, 108961.

45. Z. Cai, Z. Li, S. Ravaine, M. He, Y. Song, Y. Yin, H. Zheng, J. Teng, A. Zhang, *Chem. Soc. Rev.* **2021**, *50*, 5898.

46. M. Barhoum, J. M. Morrill, D. Riassetto, M. H. Bartl, *Chem. Mater.* **2011**, *23*, 5177.

47. E. Yablonovitch, *Phys. Rev. Lett.* **1987**, *58*, 2059.

48. S. John, *Phys. Rev. Lett.* **1987**, *58*, 2486.

49. R. Srivastava, K. Thapa, S. Pati, S. Ojha, *Prog. Electromagn. Res. C* **2008**, *81*, 225.

50. J. C. Knight, *Nature* **2003**, *424*, 847.

51. H. Wang, K.-Q. Zhang, *Sensors* **2013**, *13*, 4192.

52. J. Zi, X. Yu, Y. Li, X. Hu, C. Xu, X. Wang, X. Liu, R. Fu, *Proc. Natl. Acad. Sci. USA* **2003**, *100*, 12576.

53. B. A. Bober, J. K. Ogata, V. E. Martinez, J. J. Hallinan, T. A. Leach, B. Negru, *J. Chem. Educ.* **2018**, *95*, 1004.

54. L. D. Bonifacio, B. V. Lotsch, D. P. Puzzo, F. Scotognella, G. A. Ozin, *Adv. Mater.* **2009**, *21*, 1641.

55. K. Tsakmakidis, *Nat. Mater.* **2012**, *11*, 1000.

56. D. A. G. Bruggeman, *Ann. Phys.* **1935**, *416*, 636.

57. J. C. M. Garnett, J. Larmor, *J. C. Philos. Trans. R. Soc.* **1904**, *203*, 385.

58. J. R. Link, M. J. Sailor, *Proc. Natl. Acad. Sci. USA* **2003**, *100*, 10607.

59. S. Y. Choi, M. Mamak, G. von Freymann, N. Chopra, G. A. Ozin, *Nano Lett.* **2006**, *6*, 2456.

60. J. Kobler, B. V. Lotsch, G. A. Ozin, T. Bein, *ACS Nano* **2009**, *3*, 1669.

61. B. Auguié, M. C. Fuertes, P. C. Angelomé, N. L. Abdala, G. J. A. A. Soler Illia, A. Fainstein, *ACS Photonics* **2014**, *1*, 775.

62. F. M. Hinterholzinger, A. Ranft, J. M. Feckl, B. Ruhle, T. Bein, B. V. Lotsch, *J. Mater. Chem.* **2012**, *22*, 10356.

63. A. Ranft, F. Niekiel, I. Pavlichenko, N. Stock, B. V. Lotsch, *Chem. Mater.* **2015**, *27*, 1961.

64. K. Lazarova, H. Awala, S. Thomas, M. Vasileva, S. Mintova, T. Babeva, *Sensors* **2014**, *14*, 12207.

65. S. Colodrero, M. Ocaña, H. Míguez, *Langmuir* **2008**, *24*, 4430.

66. S. Colodrero, M. Ocana, A. R. Gonzalez-Elipe, H. Miguez, *Langmuir* **2008**, *24*, 9135.

67. L. D. Bonifacio, D. P. Puzzo, S. Breslav, B. M. Willey, A. McGeer, G. A. Ozin, *Adv. Mater.* **2010**, *22*, 1351.

68. M. M. Orosco, C. Pacholski, G. M. Miskelly, M. J. Sailor, *Adv. Mater.* **2006**, *18*, 1393.

69. G. M. Paternò, G. Manfredi, F. Scotognella, G. Lanzani, *APL Photonics* **2020**, *5*, 080901.

70. Z. Wang, J. Zhang, J. Li, J. Xie, Y. Li, S. Liang, Z. Tian, C. Li, Z. Wang, T. Wang, H. Zhang, B. Yang, *J. Mater. Chem.* **2011**, *21*, 1264.

71. Z. Wang, J. Zhang, J. Xie, C. Li, Y. Li, S. Liang, Z. Tian, T. Wang, H. Zhang, H. Li, W. Xu, B. Yang, *Adv. Funct. Mater.* **2010**, 20, 3784.

72. K. Lazarova, R. Georgiev, M. Vasileva, B. Georgieva, M. Spassova, N. Malinowski, T. Babeva, *Opt. Quantum Electron.* **2016**, *48*, 310.

73. D. Kou, W. Ma, S. Zhang, B. Tang, *ACS Appl. Polym. Mater.* **2020**, *2*, 2.

74. E. Tian, J. Wang, Y. Zheng, Y. Song, L. Jiang and D. Zhu, *J. Mater. Chem.* **2008**, *18*, 1116.

75. P. Ganter, K. Szendrei, B. V. Lotsch, *Adv. Mater.* **2016**, *28*, 7436.

76. K. Szendrei, P. Ganter, O. Sànchez-Sobrado, R. Eger, A. Kuhn, B. V. Lotsch, *Adv. Mater.* **2015**, *27*, 6341.

77. K. Szendrei-Temesi, A. Jiménez-Solano, B. V. Lotsch, *Adv. Mater.* **2018**, *30*, 6289.

78. C. Yao, J. Zhao, H. Ge, J. Ren, T. Yin, Y. Zhu, L. Ge, *Colloids Surf. A: Physicochem. Eng. Asp.* **2014**, *452*, 89.

79. C. Yao, J. Ren, C. Liu, T. Yin, Y. Zhu, L. Ge, *ACS Appl. Mater. Interfaces* **2014**, *6*, 16727.

80. J. Han, Y. Dou, M. Wei, D. G. Evans, X. Duan, *RSC Adv.* **2012**, *2*, 10488.

81. B. V. Lotsch, G. A. Ozin, *Adv. Mater.* **2008**, *20*, 4079.

82. B. V. Lotsch, G. A. Ozin, *ACS Nano* **2008**, *2*, 2065.

83. Z. Hu, C.-a. Tao, F. Wang, X. Zou, J. Wang, *J. Mater. Chem. C* **2015**, *3*, 211.

84. M. C. Fuertes, F. J. López-Alcaraz, M. C. Marchi, H. E. Troiani, V. Luca, H. Míguez, G. J. A. A. Soler-Illia, *Adv. Funct. Mater.* **2007**, *17*, 1247.

85. K. Szendrei, A. Jiménez-Solano, G. Lozano, B. V. Lotsch, H. Míguez, *Adv. Opt. Mater.* **2017**, *5*, 1700663.

86. O. Sánchez-Sobrado, G. Lozano, M. E. Calvo, A. Sánchez-Iglesias, L. M. Liz-Marzán, H. Míguez, *Adv. Mater.* **2011**, *23*, 2108.

87. A. Ranft, I. Pavlichenko, K. Szendrei, P. M. Zehetmaier, Y. Hu, A. von Mankowski, B. V. Lotsch, *Microporous and Mesoporous Mater.* **2015**, *216*, 216.

88. O. Sanchez-Sobrado, M. E. Calvo, N. Nunez, M. Ocana, G. Lozano, H. Miguez, *Nanoscale* **2010**, *2*, 936.

89. J. Ren, H. Xuan, C. Liu, C. Yao, Y. Zhu, X. Liu, L. Ge, *RSC Adv.* **2015**, *5*, 77211.

90. C. Fenzl, T. Hirsch, O. S. Wolfbeis, *Angew. Chem. Int. Ed.* **2014**, *53*, 3318.

91. M. Kolle, B. Zheng, N. Gibbons, J. J. Baumberg, U. Steiner, *Opt. Express* **2010**, *18*, 4356.

92. Y. Lu, H. Xia, G. Zhang, C. Wu, *J. Mater. Chem.* **2009**, *19*, 5952.

93. H. Ma, M. Zhu, W. Luo, W. Li, K. Fang, F. Mou, J. Guan, *J. Mater. Chem. C* **2015**, *3*, 2848.

94. A. C. Arsenault, T. J. Clark, G. von Freymann, L. Cademartiri, R. Sapienza, J. Bertolotti, E. Vekris, S. Wong, V. Kitaev, I. Manners, R. Z. Wang, S. John, D. Wiersma, G. A. Ozin, *Nat. Mater.* **2006**, *5*, 179.

95. Y. Yue, J. P. Gong, *J. Photochem. Photobiol. C* **2015**, *23*, 45.

96. E. P. Chan, J. J. Walish, E. L. Thomas, C. M. Stafford, *Adv. Mater.* **2011**, *23*, 4702.

97. S. Zhou, C. Wu, *Macromolecules* **1996**, *29*, 4998.

98. M. Li, J. Bae, *Polym. Chem.* **2020**, *11*, 2332.

99. M. C. Chiappelli, R. C. Hayward, *Adv. Mater.* **2012**, *24*, 6100.

100. R. Ozaki, T. Matsui, M. Ozaki, K. Yoshino, *Jpn. J. Appl. Phys* **2002**, *41*, L1482.

101. K. Hwang, D. Kwak, C. Kang, D. Kim, Y. Ahn, Y. Kang, *Angew. Chem. Int. Ed.* **2011**, *50*, 6311.

102. I. Pavlichenko, A. T. Exner, M. Guehl, P. Lugli, G. Scarpa, B. V. Lotsch, *J. Phys. Chem. C* **2011**, *116*, 298.

103. C. Liu, C. Yao, Y. Zhu, J. Ren, L. Ge, *Sens. Actuators B: Chem.* **2015**, *220*, 227.

104. Z. Wang, J. Zhang, Z. Wang, H. Shen, J. Xie, Y. Li, L. Lin, B. Yang, *J. Mater. Chem. C* **2013**, *1*, 977.

105. D. Kou, S. Zhang, J. L. Lutkenhaus, L. Wang, B. Tang, W. Ma, *J. Mater. Chem. C* **2018**, *6*, 2704.

106. B. V. Lotsch, G. A. Ozin, *J. Am. Chem. Soc.* **2008**, *130*, 15252.

107. B. V. Lotsch, F. Scotognella, K. Moeller, T. Bein, G. A. Ozin, *Proc. SPIE 7713*, Photonic Crystal Materials and Devices IX, **2010**, 77130V.

108. Z. Wang, J. Zhang, Z. Tian, Z. Wang, Y. Li, S. Liang, L. Cui, L. Zhang, H. Zhang, B. Yang, *Chem. Commun.* **2010**, *46*, 8636.

109. G. Soler-Illia, M. Fuertes, P. Angelomé, M. Marchi, H. E. Troiani, V. Luca, H. Míguez, Mesoporous multilayer thin films: photonic crystals sensitive to the environment, **2008**.

110. N. Hidalgo, M. E. Calvo, H. Míguez, *Small* **2009**, *5*, 2309.

111. O. Sanchez-Sobrado, M. E. Calvo, H. Miguez, *J. Mater. Chem.* **2010**, *20*, 8240.

112. R. A. Allardyce, V. S. Langford, A. L. Hill, D. R. Murdoch, *J. Microbiol. Methods* **2006**, *65*, 361.

113. A. von Mankowski, K. Szendrei-Temesi, C. Koschnick, B. V. Lotsch, *Nanoscale Horiz.* **2018**, *3*, 383.

114. S. Deniard-Courant, Y. Piffard, P. Barboux, J. Livage, *Solid State Ion.* **1988**, *27*, 189.

115. M. Däntl, S. Guderley, K. Szendrei-Temesi, D. Chatzitheodoridou, P. Ganter, A. Jiménez-Solano, B. V. Lotsch, *Small* **2021**, *17*, 2007864.

116. J. Hou, M. Li, Y. Song, *Angew. Chem. Int. Ed.* **2018**, *57*, 2544.

117. K. Szendrei-Temesi, Ph.D. Thesis, LMU Munich, **2018**.

118. J. Zhang, X. Liu, G. Neri, N. Pinna, *Adv. Mater.* **2016**, *28*, 795.

119. P. Ganter, Ph.D. Thesis, LMU Munich, **2018**.

120. T. L. Kelly, A. Garcia Sega, M. J. Sailor, *Nano Lett.* **2011**, *11*, 3169.

3 Objective

Despite the extraordinary and diverse properties of nanosheets and their potential applicability for miniaturized colorimetric sensors based on structural color for gas and vapor sensing, the translation of nanosheet-based devices to commercially successful applications in everyday life is still in its infancy. This circumstance originates from the lack of techniques to tailor and fine-tune their sensing properties according to the users' requirements. Further obstacles in this regard are the lack of methods for controlling the shape of the device or transferring the sensors to arbitrary surfaces to broaden the application possibilities. In order to exploit the superior properties of nanosheets for practical applications, it is indispensable to tackle these remaining challenges with the aim of enabling practical applications.

$H_3Sb_3P_2O_{14}$ nanosheet-based devices (both thin films and 1DPCs) have great potential for applications as colorimetric vapor sensors due to their tremendous swelling capability, label-free optical readout, fast response and recovery times, and the possibility to tailor the selectivity to specific vapors.[1-4] Previous research has shown that *Fabry-Pérot* thin films based on $H_3Sb_3P_2O_{14}$ nanosheets can intercalate primary alkylamines over the vapor phase, which allows the tuning of the sensor properties.[5] Based on these findings, the main objectives of this thesis are to utilize this amine intercalation in $H_3Sb_3P_2O_{14}$-based sensors for the design and development of highly tunable and adaptable optical nanosheet-based gas sensors (thin film and 1DPC) for future applications, and to gain fundamental insights into the mechanism of the amine intercalation.

To this end, the behavior of amine intercalation should be analyzed when a antimony phosphate *Fabry-Pérot* sensor, which was already intercalated with a certain amine, is exposed to the vapor of another amine. Possible scenarios include the replacement of the first intercalated amine, a co-intercalation of both amines, or no reaction at all. In order to verify the outcome, a library of different primary alkylamines needs to be examined. If a replacement of the first amine takes place during the exposure towards a second one, the properties of the *Fabry-Pérot* sensor can be fine-tuned post-synthetically. In addition, this would enable patterning of the sample through spatially resolved amine intercalation and exchange using a mask, which would potentially enlargen the application range even further.

Another goal is to create adaptable gas sensors by making them transferrable to arbitrary substrates. For these experiments, it is necessary to use antimony phosphate 1DPC sensors

instead of thin films because they are thicker and therefore have a higher stability when detached from their substrate. By applying a sacrificial layer approach, while making use of the amine intercalation to hydrophobize the sensor, the 1DPC can potentially be detached from its substrate in water. This would leave the free-standing hydrophobic 1DPC at the water-air interface. In a second step, it may be picked up with another substrate, such as a curved glass, or a metal surface, to which the sensor cannot be spin-coated. Presumably, patterning of the 1DPC sensor by controlled spatial amine intercalation can be combined with the transfer process to enable pattern transfer.

Since amine intercalation has also been reported for other ionic and non-ionic layered materials, it can be assumed that the method of amine intercalation is generally applicable. Therefore, it is highly desirable to understand the underlying mechanisms at a fundamental level to rationally improve the design and application of future nanosheet-based sensing devices. To achieve this goal, the amine intercalation in antimony phosphate thin films should be studied by monitoring the peak shift with real time X-ray diffraction (XRD) measurements and subsequently performing an in depth analysis of the data to derive the intercalation mechanism.

3.1 References

1. K. Szendrei-Temesi, O. Sanchez-Sobrado, S. B. Betzler, K. M. Durner, T. Holzmann, B. V. Lotsch, *Adv. Funct. Mater.* **2018**, *28*, 1705740.
2. K. Szendrei, P. Ganter, O. Sànchez-Sobrado, R. Eger, A. Kuhn, B. V. Lotsch, *Adv. Mater.* **2015**, *27*, 6341.
3. K. Szendrei-Temesi, A. Jiménez-Solano, B. V. Lotsch, *Adv. Mater.* **2018**, *30*, 6289.
4. K. Szendrei, A. Jiménez-Solano, G- Lozano, B. V. Lotsch, H. Míguez,. *Adv. Opt. Mater.* **2017**, *5*, 1700663.
5. P. Ganter, L. M. Schoop, M. Däntl, B. V. Lotsch, *Chem. Mater.* **2018**, *30*, 2557.

4 Tailoring and Fine-Tuning the Selectivity of Nanosheet-Based Fabry-Pérot Interference Thin Films: Amine Intercalation and Exchange

4.1 Summary

Previous research has demonstrated that amine intercalation enables the tuning of the gas sensing properties of *Fabry-Pérot* thin films based on $H_3Sb_3P_2O_{14}$ nanosheets. In order to further increase the versatility of the amine intercalated thin films, we made use of this amine intercalation to rationally tailor and fine-tune the sensing properties. In this project, we performed a facile two-step amine intercalation protocol, which revealed that one amine can easily be exchanged for another one *via* the vapor phase. This approach provides an exquisite control over the properties of the thin film, as the continuous change of the mean *d*-spacing and polarity of the films can be performed reversibly in the sub-Å range. In addition, we exploited the reversibility of the amine exchange process in combination with a mask to demonstrate patterning of the thin films.

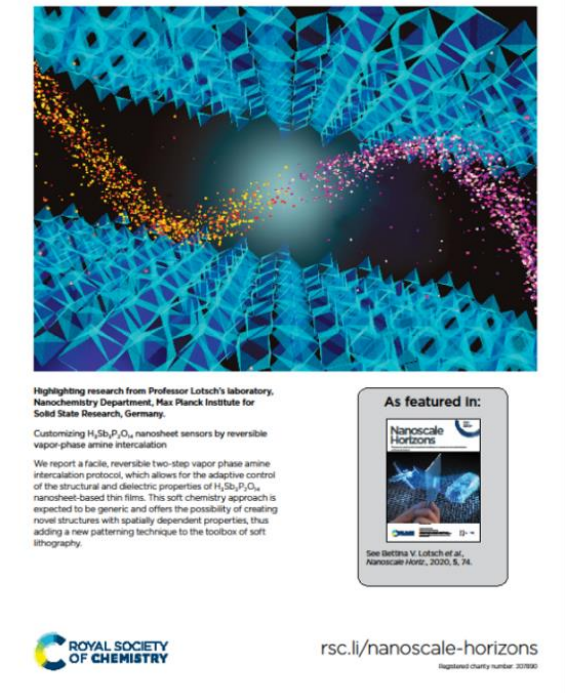

Contributions: Marie Däntl fabricated the samples and conducted the measurements. Marie Däntl analyzed the results with the help of Pirmin Ganter, Katalin Szendrei-Temesi and Alberto Jiménez-Solano. Marie Däntl edited the figures and wrote the manuscript with the help of all contributing authors.

This project was highlighted as a back cover in the journal Nanoscale Horizons. The cover image was designed by Marie Däntl and Alberto Jiménez-Solano.

4.2 Customizing $H_3Sb_3P_2O_{14}$ Nanosheet Sensors by Reversible Vapor-phase Amine Intercalation

The work in this Chapter was reproduced and adapted from:

*Marie Däntl, Pirmin Ganter, Katalin Szendrei-Temesi, Alberto Jiménez-Solano, Bettina V. Lotsch**

Published in: *Nanoscale Horizons* **2020**, *5*, 74-81.

DOI: 10.1039/C9NH00434C

https://pubs.rsc.org/en/content/articlehtml/2020/nh/c9nh00434c

Supporting information can be found in Chapter 8.2.

4.3 Abstract

Harvesting the large property space of 2D materials and their molecular-level fine-tuning is of utmost importance for future applications such as miniaturized sensors for environmental monitoring or biomedical detection. Therefore, developing straightforward strategies for the reversible and gradual fine-tuning of nanosheet properties with soft chemical intercalation methods is in high demand. Herein we address this challenge by customizing the host–guest interactions of nanosheets based on the solid acid $H_3Sb_3P_2O_{14}$ by vapor-phase amine-intercalation with primary alkylamines. Fine-tuning of the structural and chemical properties of the intercalated nanosheets is achieved by applying a two-step, post-synthetic intercalation strategy *via* the vapor phase. The method allows for the gradual and reversible replacement of one amine type by another. Hence, fine-tuning of the *d*-spacing in the sub-Å regime is accomplished and offers exquisite control of the properties of the thin films such as refractive index, polarity, film thickness and sensitivity towards solvent vapors. Moreover, we employ amine replacement to pattern thin films by locally resolved amine intercalation and subsequent washing, leading to spatially dependent property profiles. This process thus adds a new vapor-phase, amine-based variant to the toolbox of soft lithography.

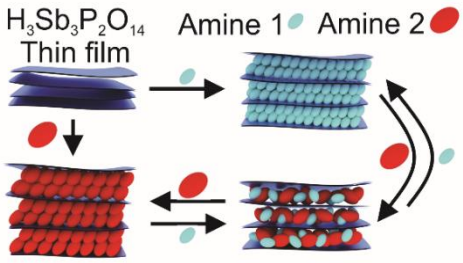

4.4 Conceptual Insights

Fine-tuning the (opto)electronic properties of nanosheet-based thin films post-synthetically and with high spatial resolution is required in order to create sophisticated devices – for example miniaturized sensors – more easily. So far, property tuning of 2D materials has been achieved for example *via* covalent or electrochemical intercalation and de-intercalation. However, these approaches are either non-reversible or require a complex setup. Therefore, straightforward strategies for fine-tuning the properties of nanosheet materials are in high demand. We herein report a facile, two-step amine intercalation protocol, which allows for the adaptive control of the structural and dielectric properties of amine intercalated $H_3Sb_3P_2O_{14}$ nanosheet thin films such as film thickness, polarity, sensitivity towards solvent vapors, and effective refractive index. This soft chemistry approach is expected to be generic and offers the possibility of creating novel structures with spatially dependent properties, thus adding a new patterning technique to the toolbox of soft lithography, based on reversible amine intercalation.

4.5 Introduction

After the discovery of graphene, the interest in inorganic layered materials resurged, since like graphite, they can be exfoliated into two-dimensional (2D) nanosheets, which exhibit properties distinct from their bulk counterparts.[1-5] So far, exfoliation of a large variety of layered materials such as graphite,[6] transition metal dichalcogenides (TMD),[7] transition metal oxides (TMO),[8] layered double hydroxides (LDH),[9] Zintl phases[10] and MXenes[11] has been successful. Although these nanosheets exhibit many outstanding and diverse properties in their pristine form, tailoring and fine-tuning their properties in a rational manner for applications and processing is still challenging.[12-14]

As of now, there are five main strategies for modifying the physical and chemical properties of the nanosheets. These approaches include covalent functionalization,[12,15-17] intercalation and ion exchange,[18,19] morphology control,[20-23] nanoparticle decoration[24,25] and elemental substitution.[26,27] So far, post-synthetic tuning of the nanosheet properties over a broad range is only possible with covalent functionalization, electrochemical[28,29] and soft chemical intercalation, as well as ion exchange methods.[30-32] For instance, covalent modification has been utilized for functionalizing germanane nanosheets with organic groups to tailor their electronic structure.[15,33,34] Moreover, ion exchange reactions with different cations in graphene oxide (GO) membranes allow for precisely controlling the interlayer spacing, which leads to a

change in the permeability of the membranes.[35] In addition, we demonstrated a vapor-phase amine intercalation strategy for modifying the swelling characteristics of $H_3Sb_3P_2O_{14}$ nanosheet-based thin films.[36] Apart from that, the gradual optoelectronic tunability of $Ti_3C_2T_x$ (T = O, OH, F or other surface termination) MXene thin films was demonstrated by electrochemical intercalation.[37] While all of these methods are efficient in their present stage, only electrochemical intercalation and de-intercalation currently achieves a reversible and fine-tuned gradual modification, whereas a rather stepwise and non-reversible change in properties is observed for the other methods. In contrast to the other approaches, however, electrochemical intercalation requires a more complex experimental set-up.[18,37,38] Therefore, strategies for the straightforward, reversible and gradual fine-tuning of nanosheet properties with soft chemical intercalation methods are in high demand.

Inspired by intercalation studies of bulk materials[39] and ligand exchange reactions for nanocrystals[40] or nanoparticle assemblies,[41] here we present a comprehensive vapor-phase amine intercalation strategy for fine-tuning the properties of $H_3Sb_3P_2O_{14}$ nanosheet-based photonic thin films. We demonstrate that by using a two-step post-synthetic intercalation method a continuous and reversible fine-tuning of the *d*-spacing in the sub-Å regime is achieved, allowing for the exquisite control of the properties of the thin films. Hereby, the tunable properties include the optical properties such as the refractive index, the polarity, film thickness and sensitivity towards solvent vapors. Therefore, this intercalation approach stands out from covalent modification and electrochemical intercalation, as it combines an easy synthetic methodology with gradual and reversible tunability, which is a generic method that can be applied to a wide range of nanosheets.

4.6 Results and Discussion

Fabry-Pérot photonic thin films producing structural colors due to thin film interference were chosen as an optical transducer since they enable the label-free colorimetric observation of intercalation processes in inherently colorless materials.[42] A scheme of the two-step intercalation protocol for tuning the properties of nanosheet-based photonic thin films is given in Fig. 4.1a. In the first step, $H_3Sb_3P_2O_{14}$ thin films were prepared by spin-coating and subsequently intercalated with primary alkylamines *via* the vapor phase.[36,43] Through the acid–base reaction of the amines with the interlayer protons of the solid acid $H_3Sb_3P_2O_{14}$, ammonium ions are formed and the amines are thus trapped in the interlayer space (Fig. 4.1b). Moreover, the amine-modified films exhibit a tilted bimolecular arrangement of the

intercalants, and long-term stability of the amine intercalation was inferred by heating experiments (Fig. S4.1, ESI). We find that the intercalated amines cannot be removed when heating the samples to 60 °C over a period of ten days. Note that in the following the nomenclature used for the intercalated amines refers to the number of carbon atoms in the alkyl chain (e.g. butylamine is named C4). In the second step, the primary alkylamine intercalated films were exposed to other primary alkylamines with various chain lengths. Hereby, different outcomes after an equilibration process can be imagined, including no change of the intercalated sample (i), a co-intercalation of two different amines (ii), or the complete replacement of the first intercalated amine by the second one (iii). The last two outcomes enable the versatile post-synthetic modification of the nanosheet-based thin films, as they allow for a gradual and reversible tailoring of the structural properties such as the interlayer distance, the optical properties, the polarity and, hence, wettability of the films. As a consequence, this makes a potentially vast property space accessible and at the same time allows for customizing the sensing response of a nanosheet sensor based on a single material.[44]

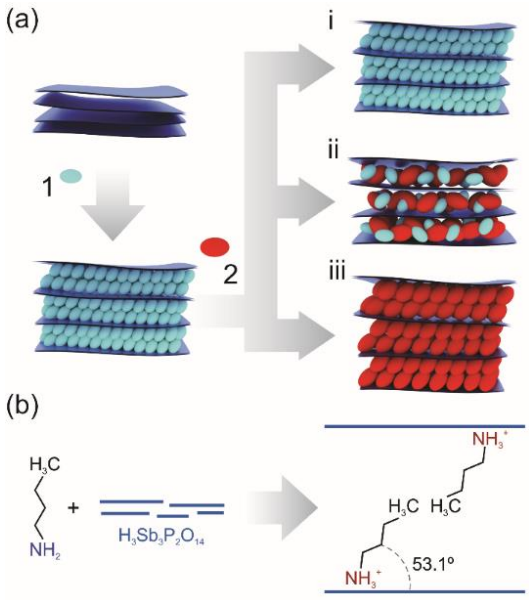

Fig. 4.1 (a) Schematic overview of the two-step intercalation of primary amines into nanosheet-based photonic thin films. (1) and (2) show the first and second intercalation step, respectively. (i), (ii) and (iii) highlight possible outcomes when exposing the amine intercalated thin film to the second, different amine vapor. (i): no exchange, (ii): co-intercalation, (ii): replacement. (b) Trapping of amines in the interlayer space through acid–base reaction and tilted bimolecular arrangement.[36]

For the modification of the intercalated thin films in the second step, either longer or shorter amines than the ones already intercalated in step 1 can be used. These possibilities are referred to as "upward" (e.g. replacement of C2 by C4) and "downward" (e.g. replacement of C6 by C4) intercalation in the following. The differences in the alkyl chain lengths of the amines lead

to a change in the interlayer distance. Hence, the upward and downward intercalation in $H_3Sb_3P_2O_{14}$ can be tracked optically (spectroscopically or by the naked eye) through the change in structural color, and by out-of-plane X-ray powder diffraction (XRPD). Our results immediately indicate that in the system studied here possibility (i) does not occur, since the interference color of the thin films invariably changes during the exposure to the second amine vapor, thus suggesting a change in the interlayer distances. When probed in Bragg–Brentano geometry, the XRPD patterns of the first step intercalated sample exhibit only 00*l* reflections due to the preferred orientation of the nanosheets parallel to the substrate.[45] Therefore, and considering the turbostratic disorder, the first reflection corresponds to the basal plane, i.e. the distance between the nanosheets. During the second intercalation step, the out-of-plane XRPD measurements in Fig. 4.2a (middle and right) reveal the gradual replacement of the first intercalated amine up to a complete exchange depending on the amine exposure time for the upward (C4 + C6) and downward (C6 + C4) intercalation. For these series of experiments, samples were taken from the intercalation chamber at a certain time (in the range of 1 to 30 minutes) during the second intercalation step, which either leads to a co-intercalation of both amines or a complete replacement of the first one (time dependence of Fig 4.1b and c). Similar results were obtained for the C6 + C8 and C8 + C6 experiments (Fig. S4.2, ESI). Note that these measurements were performed after a room temperature equilibration step, i.e. keeping the samples in a closed sample holder under ambient conditions for several days. When measuring the out-of-plane XRPD (Fig. 4.2a, left) of the sample directly after the second amine exposure a peak splitting is observed. The peak splitting strongly indicates non-uniform distribution and phase segregation of the amine guests within the thin film. During the equilibration step the amines diffuse through the film and mix, giving rise to uniformly intercalated interlayer spaces. As a consequence, the peak splitting in the XRPD patterns gradually vanishes leading to one single series of basal reflections, which do not change significantly over months. Therefore, a co-intercalation of both amines with a nearly uniform distribution is achieved.

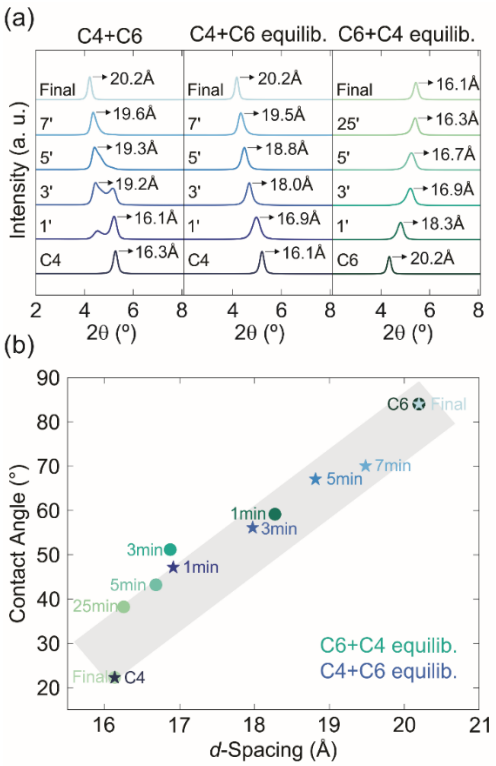

Fig. 4.2 Modification of primary alkylamine intercalated thin films with a second primary alkylamine in a two-step intercalation process allowing for sub-Å control of the interlayer space, e.g. from 16.9 to 16.7 Å, by changing the exposure time of a C6 intercalated sample to C4 from 3 to 5 minutes. (a) Out-of-plane XRPD patterns (Cu-$K_{\alpha 1}$) of upward and downward intercalation at different intercalation times in the range of 1 to 30 minutes. Patterns on the left were recorded directly after the intercalation (peak splitting), whereas the patterns in the middle and on the right were measured after the equilibration step (nearly uniform peaks). Upward intercalation results in an increase and downward intercalation leads to a decrease in the stacking distance. (b) Contact angle measurements of upward and downward intercalated samples in correlation with the *d*-spacing. The gray rectangle was inserted as a guide for the eye.

Applying our two-step modification strategy, we are able to control the interlayer space continuously in the sub-Å regime, which is in contrast to previous nanosheet amine intercalation studies exhibiting a step-like change in *d*-spacing based on the amine chain length (Fig. 4.2b, ESI).[36,46,47] The change in properties with modification of the *d*-spacing of the $H_3Sb_3P_2O_{14}$ thin films is underlined by contact angle measurements (Fig. 4.2b), as they show that the hydrophilicity of the C4 intercalated sample decreases continuously with exposure time towards C6 vapor due to the difference in the hydrophobicity of the used amines. The opposite behavior is observed for the exposure of the C6 intercalated sample towards C4, as expected. The continuous control of the *d*-spacing is highly important for fine-tuning the optical properties as well as the polarity of nanosheet-based thin films for different applications such as the development of chemo-selective sensors, optoelectronic devices, and membranes.[48,49] Specifically, through engineering the intergallery space at the sub-Å level very

similar molecules with only subtle differences in size or polarity can exhibit significantly altered permeation rates, which enables possible applications in the field of membranes and sieving. For example, the fine control of the *d*-spacing influences the selectivity of physically confined GO (PCGO) membranes towards hydrated ions with similar sizes significantly due to their differences in size.[44] In addition, other important properties of nanosheets, such as the band gap, can also be influenced directly through the interlayer spacing.[50,51]

In order to demonstrate the scope of the amine exchange process and establish its generality, the experiments were carried out for various primary alkylamines with chain lengths ranging from C2–C12 (see Tab. S4.1, ESI) and thus different hydrophilicity. The resulting stacking distances of the two-step amine exchanged samples are given in Fig. 4.3a. The *d*-values are all similar for each set of experiments, thus suggesting a complete exchange of the first intercalated amine in all cases. Taking into account the fact that co-intercalation results in altered *d*-values compared to the singly intercalated samples as discussed above, complete exchange can unequivocally be verified. The complete out-of-plane XRPD patterns of the experiment series with C6 intercalated in the second step are given in Fig. 4.3b for upward as well as downward intercalated samples. It should be noted that the second reflection is the second order stacking reflection at ~8.7° 2θ. This implies a homogeneous exchange process. For out-of-plane XRPD patterns of the other experiment series see Fig. S4.3 (ESI). Further confirmation of the complete exchange of the first intercalated amine is given by microscope images in combination with reflectance measurements (Fig. 4.3c-e). Fig. 4.3c shows microscope images of one- and two-step intercalated samples and indicates similar structural color for samples containing the same amine after the second intercalation step compared with the corresponding singly intercalated samples. Minor differences in color may arise from different film thicknesses before the intercalation due to the spin-coating process. The reflectance spectra of an upward as well as a downward intercalation starting from C6 are given in Fig. 4.3d (for other reflectance spectra see Fig. S4.4, ESI) along with a comparison of the relative optical shifts of all conducted experiments in Fig. 4.3e. It can be observed that the optical shifts are linear and all show a similar slope for a certain amine. Note that the difference in color for each intercalated amine renders this system a versatile platform for applications in amine detection.

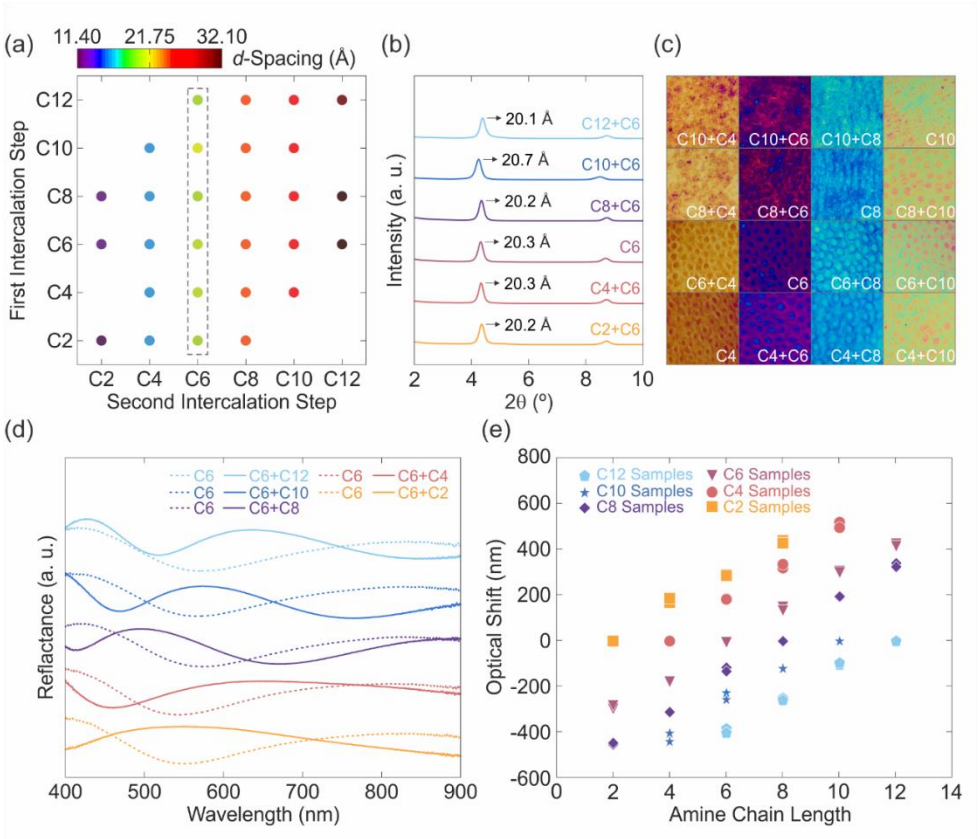

Fig. 4.3 (a) *d*-Values of all amine exchange experiments showing a complete exchange of the first intercalated amine after exposure to a second amine. (b) Detailed out-of-plane XRPD patterns (Cu-$K_{\alpha 1}$) for upward and downward intercalation of samples with C6. Second reflection observed at ~8.7° 2θ is the second order stacking reflection. (c) Comparison of some microscope images of singly and doubly intercalated $H_{3-x}(NH_3(CH_2)_{n-1}CH_3)_xSb_3P_2O_{14}$ thin films. (d) Reflectance spectra of the one-step C6 intercalated samples (dashed) and after the second intercalation step (solid lines). (e) Comparison of the relative optical shifts of all prepared thin films. Nomenclature: a certain color refers to samples intercalated with the same amine in the first intercalation step, e.g. all light blue pentagons represent samples, which contained dodecylamine in step one.

Complementary ellipsometry measurements (Fig. S4.5, ESI) also evidence the complete replacement of the first intercalated amine. Furthermore, Raman measurements (Fig. S4.6, ESI) support the previously discussed results, as the C–H vibrations of the amine chains offer a fingerprint to identify the intercalated species. With larger amine chain lengths, the observed peaks at 1200, 1300 (both νC–C or δC–H), 2900 and 3000 cm^{-1} (νCH_2 and νCH_3) become more pronounced and the latter are slightly shifted towards smaller wavenumbers (see Fig. S4.6a, ESI).

Since we could show that a partial up to a complete replacement of the first intercalated amine gradually takes place when exposing the sample to another amine vapor, this has important implications for customizing the interlayer space and, hence, sensor design, post-synthetically. The present experiments concentrated on showing the intercalation and exchange of primary

alkylamines since there are many different ones with different hydrophilicity and therefore they allow a systematic study of the behavior. However, it is also possible to intercalate and exchange amines which are relevant in food spoilage control in the same manner. Very preliminary results for trimethylamine and 1,5-diaminopentane (both produced through microbial spoilage of fish and meat) are given in Fig. S4.7 (ESI). The exchange of trimethylamine with C6 seems to take place on a similar timescale as observed for the primary alkylamines. Regarding the 1,5-diaminopentane the intercalation takes a lot longer (ca. 2 days) and therefore the exchange was not studied but should in principle be possible. The complete characterization of the intercalation and exchange of a large class of biologically relevant amines however, goes beyond the scope of this work.

For many applications cyclability of the intercalated sample is of prime importance and reversible intercalation would allow for versatile and repeated use. To demonstrate this possibility, cycling experiments were performed by intercalating the sample with C2 and subsequently replacing C2 with C8 and *vice versa*. Fig. 4.4a shows the position of the basal reflection obtained for the different intercalation states for up to five cycles, whereby the exposure to each amine leads to a complete replacement of the one intercalated before. This can be seen from the peak positions, where the stacking distances of all samples (Fig. 4.4a) are in good agreement with the ones of the singly C2 (11.5 Å) or C8 (24.4 Å) intercalated samples. Further, the complete replacement of the intercalated amines can also be tracked with the naked eye, which is shown in the insets in Fig. 4.4a. C2 samples exhibit a blue-yellow hue whereas the C8 samples show a purple-blue color. The two-step amine modification method is advantageous over other nanosheet modification methods such as covalent functionalization or nanoparticle decoration, for which a reversible and cyclable modification is notoriously difficult if not close to impossible to achieve. Moreover, our modification method stands out against electrochemical modification methods, as they commonly lack air stability and need an external power supply for cycling.[18,28]

Re-modification of the samples by intercalating and replacing amines with different properties can be used to build novel structures with arbitrary shapes and spatio-dependent, tailor-made properties. To demonstrate this concept, an entire wafer was intercalated with C2. Using a mask, a large circular part of the sample was subsequently replaced with C10. Finally, another smaller circular region in this circle was replaced with C6. A photograph of a three-step amine intercalated sample along with close-up images of different regions of the sample and a

schematic height profile for different parts of the sample are depicted in Fig. 4.4b. The inset numbers indicate the corresponding region in the height profile. Furthermore, representative reflectance spectra are given for different parts of the sample (Fig. 4.4c). Due to the compactness and area-dependent functionality, these structures are good candidates for multi-purpose, miniaturized sensors.

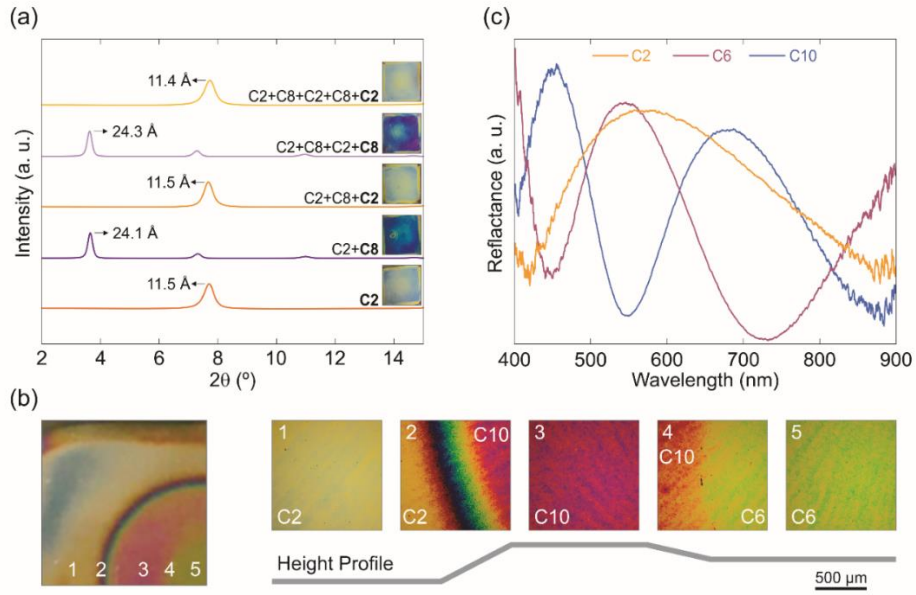

Fig. 4.4 (a) Out-of-plane XRPD patterns (Cu-$K_{\alpha 1}$) obtained for cycling experiments. A C2 intercalated sample was exposed to C8 and C2 in turn up to five times to show the cyclability and, hence, reversibility of the amine replacement. The insets of sample photographs show the sample color after each intercalation step. (b) Photograph of a three-step amine intercalated sample along with images of different regions of the sample and a schematic height profile for each part of the sample. The inset numbers indicate the corresponding region in the height profile. (c) Representative reflectance spectra for different parts of the sample.

Another example for an application of the amine replacement process is shown in Fig. 4.5. Since the spin-coating process during sample fabrication does not allow for patterning the deposited thin film, masks have to be applied during the intercalation step in order to obtain *e.g.* a circular amine intercalated thin film. To realize pattern formation, the C2-intercalated hydrophilic part of the sample given in Fig. 4.5(1), which has a circular part intercalated with hydrophobic C10, was removed by repeatedly washing the wafer with water yielding a hydrophobic circular thin film. However, this approach is only possible if the circular intercalated part contains a hydrophobic amine, which prevents this part from being washed away with polar solvents. If the desired pattern should be obtained with a hydrophilic amine at the end, the hydrophobic region can easily be turned into a hydrophilic one through re-modification by a short-chain amine such as C2 (Fig. 4.5(2)). Each row in Fig. 4.5 shows two

microscope images along with a photograph of the sample (right). The differences in the color in the circular part arise from inhomogeneous thickness in the middle of the sample due to the spin-coating process. The modification could also be performed in the same manner using the pristine $H_3Sb_3P_2O_{14}$ thin film. In this case, however, the re-modification of a C2 intercalated thin film was chosen in order to compare the color with the obtained C2 modified circular thin film. The intercalation of more complex patterns, such as the letter "M", can also be achieved (see Fig. S4.8, ESI), which enables the straightforward patterning of the amine modified thin film.

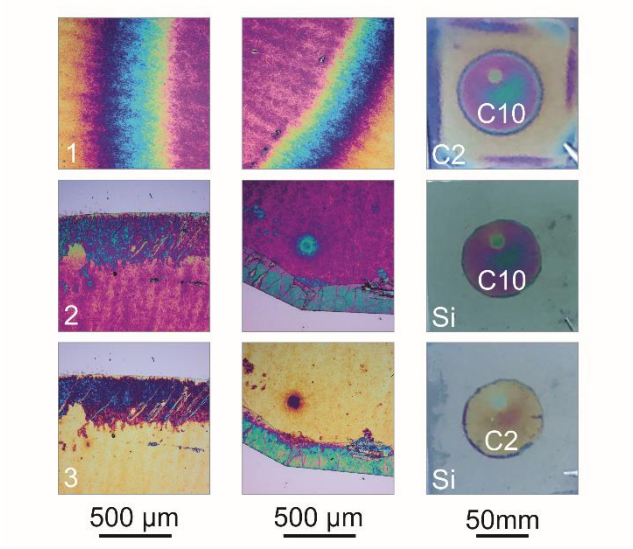

Fig. 4.5 Patterning through amine intercalation. Each row shows two images taken with an optical microscope (left and middle) along with a photograph of the sample (right). With the intermediate intercalation and washing step (2) a circular shape of C2 intercalated thin film (3) could be obtained.

Changing the properties of surfaces in a spatially distinct manner through amine functionalization is currently also achieved with soft lithography methods, for example microcontact printing.[52,53] Soft lithography has the advantage of creating patterns with high spatial resolution down to about 30 nm with well-defined and controllable surface chemistry.[54] However, methods like microcontact printing are rather time-consuming in comparison to the amine intercalation strategy.[55] Therefore, the above-described patterning approach relying on amine-exchange and etching adds another easy and complementary method to the toolbox of soft lithography.

4.7 Conclusions

In summary, we showed that amine intercalated photonic thin films consisting of $H_3Sb_3P_2O_{14}$ nanosheets could easily be modified with other primary alkylamines with a straightforward,

soft chemistry based reaction protocol *via* the vapor phase. We observe a continuous exchange of the first by the second amine until complete replacement is reached, which can be controlled through the exposure time (in the range of minutes) to the second amine vapor. Due to the continuous replacement of the first amine by a second amine, the interlayer spacing could be tailored on the sub-Å level and the polarity of the nanosheets was gradually fine-tuned over a broad range. The scope of the two-step amine modification strategy was verified by intercalating and replacing a large library of primary alkylamines. Furthermore, cycling experiments revealed that the modification is a reversible process, which allows for a versatile adaptive control of the materials' properties. This is a clear advantage compared to non-reversible covalent modification[12,17] of layered materials or sophisticated electrochemical control requiring external power supply and in most cases inert gas conditions.[18] Furthermore, patterning experiments indicate that the amine replacement method can be employed to create more complex structures coupled with area-resolved intercalation and etching.[36,56] Since the modification of other ionic and also non-ionic layered materials with amines has been studied frequently in the past,[36,57-60] the modification process developed in this work is most likely generic. Hence, it can be transferred to other nanosheet-based host materials displaying acid–base behavior and therefore opens up a new methodology for fine-tuning nanosheet properties for sensing applications and beyond. Other applications may lie in the field of membranes, in which the interlayer species takes the role of the gatekeeper controlling the selectivity through its shape (resulting *d*-spacing and properties, e.g. polarity).[61] More generally, the two-step amine intercalation approach may be utilized to fine-tune the mechanical[46,47] or (opto)electronic properties[62] of nanosheet-based thin films post-synthetically and with high spatial resolution in order to create sophisticated devices more easily.[63]

4.8 Conflicts of Interest

There are no conflicts to declare.

4.9 Acknowledgements

Financial support was granted by the Max Planck Society, the University of Munich (LMU) and the Cluster of Excellence e-conversion. The authors gratefully acknowledge Dimitra Chatzitheodoridou for providing her experience in thin film patterning and thank Armin Schulz for Raman spectroscopy, Christine Stefani for thin film X-ray diffraction measurements and James Borchert for contact angle measurements. A. J. S. gratefully acknowledges a

postdoctoral scholarship from the Max Planck Society. Open Access funding provided by the Max Planck Society.

4.10 References

1. J. N. Coleman, M. Lotya, A. O'Neill, S. D. Bergin, P. J. King, U. Khan, K. Young, A. Gaucher, S. De, R. J. Smith, I. V. Shvets, S. K. Arora, G. Stanton, H.-Y. Kim, K. Lee, G. T. Kim, G. S. Duesberg, T. Hallam, J. J. Boland, J. J. Wang, J. F. Donegan, J. C. Grunlan, G. Moriarty, A. Shmeliov, R. J. Nicholls, J. M. Perkins, E. M. Grieveson, K. Theuwissen, D. W. McComb, P. D. Nellist, V. Nicolosi, *Science* **2011**, *331*, 568.
2. V. Nicolosi, M. Chhowalla, M. G. Kanatzidis, M. S. Strano, J. N. Coleman, *Science* **2013**, *340*, 1226419.
3. Y. Ebina, T. Sasaki, M. Watanabe, *Solid State Ion.* **2002**, *151*, 177.
4. T. Sasaki, *J. Ceram. Soc. Jpn.* **2007**, *115*, 9.
5. L. M. Liz-Marzán, M. Giersig, *Low-Dimensional Systems: Theory, Preparation, and Some Applications*, Springer, Berlin, Germany, **2003**.
6. A. K. Geim, K. S. Novoselov, *Nat. Mater.* **2007**, *6*, 183.
7. J. A. Wilson, A. D. Yoffe, *Adv. Phys.* **1969**, *18*, 193.
8. K. Kalantar-zadeh, J. Z. Ou, T. Daeneke, A. Mitchell, T. Sasaki, M. S. Fuhrer, *Appl. Mater. Today* **2016**, *5*, 73.
9. R. Ma, T. Sasaki, *Adv. Mater.* **2010**, *22*, 5082.
10. M. Q. Arguilla, J. Katoch, K. Krymowski, N. D. Cultrara, J. Xu, X. Xi, A. Hanks, S. Jiang, R. D. Ross, R. J. Koch, S. Ulstrup, A. Bostwick, C. Jozwiak, D. W. McComb, E. Rotenberg, J. Shan, W. Windl, R. K. Kawakami, J. E. Goldberger, *ACS Nano* **2016**, *10*, 9500.
11. M. Naguib, V. N. Mochalin, M. W. Barsoum, Y. Gogotsi, *Adv. Mater.* **2013**, *26*, 992.
12. W. L. B. Huey, J. E. Goldberger, *Chem. Soc. Rev.* **2018**, *47*, 6201.
13. D. Sangian, Y. Ide, Y. Bando, E. Rowan Alan, Y. Yamauchi, *Small* **2018**, *14*, 1800551.
14. S. Bertolazzi, M. Gobbi, Y. Zhao, C. Backes, P. Samorì, *Chem. Soc. Rev.* **2018**, *47*, 6845.
15. S. Jiang, M. Q. Arguilla, N. D. Cultrara, J. E. Goldberger, *Acc. Chem. Res.* **2015**, *48*, 144.
16. S. S. Chou, M. De, J. Kim, S. Byun, C. Dykstra, J. Yu, J. Huang, V. P. Dravid, *J. Am. Chem. Soc.* **2013**, *135*, 4584.
17. D. Voiry, A. Goswami, R. Kappera, e. SilvaCecilia de Carvalho Castro, D. Kaplan, T. Fujita, M. Chen, T. Asefa, M. Chhowalla, *Nat. Chem.* **2015**, *7*, 45.

18. J. Wan, S. D. Lacey, J. Dai, W. Bao, M. S. Fuhrer, L. Hu, *Chem. Soc. Rev.* **2016**, *45*, 6742.

19. M. Boota, M. Pasini, F. Galeotti, W. Porzio, M.-Q. Zhao, J. Halim, Y. Gogotsi, *Chem. Mater.* **2017**, *29*, 2731.

20. M. Osada, T. Sasaki, *Dalton Trans.* **2018**, *47*, 2841.

21. Z. Wang, J. Xuan, Z. Zhao, Q. Li, F. Geng, *ACS Nano* **2017**, *11*, 11559.

22. C. Backes, B. M. Szydłowska, A. Harvey, S. Yuan, V. Vega-Mayoral, B. R. Davies, P.-l. Zhao, D. Hanlon, E. J. G. Santos, M. I. Katsnelson, W. J. Blau, C. Gadermaier, J. N. Coleman, *ACS Nano* **2016**, *10*, 1589.

23. C. Backes, R. J. Smith, N. McEvoy, N. C. Berner, D. McCloskey, H. C. Nerl, A. O'Neill, P. J. King, T. Higgins, D. Hanlon, N. Scheuschner, J. Maultzsch, L. Houben, G. S. Duesberg, J. F. Donegan, V. Nicolosi, J. N. Coleman, *Nat. Commun.* **2014**, *5*, 4576.

24. D. Sarkar, X. Xie, J. Kang, H. Zhang, W. Liu, J. Navarrete, M. Moskovits, K. Banerjee, *Nano Lett.* **2015**, *15*, 2852.

25. A. Jiménez-Solano, C. López-López, O. Sánchez-Sobrado, J. M. Luque, M. E. Calvo, C. Fernández-López, A. Sánchez-Iglesias, L. M. Liz-Marzán, H. Míguez, *Langmuir* **2012**, *28*, 9161.

26. M. Osada, G. Takanashi, B.-W. Li, K. Akatsuka, Y. Ebina, K. Ono, H. Funakubo, K. Takada, T. Sasaki, *Adv. Funct. Mater.* **2011**, *21*, 3482.

27. M. Osada, T. Sasaki, *Int. J. appl. Ceram. Tec.* **2012**, *9*, 29.

28. J. S. Kang, M. Ke, Y. Hu, *Nano Lett.* **2017**, *17*, 1431.

29. W. Bao, J. Wan, X. Han, X. Cai, H. Zhu, D. Kim, D. Ma, Y. Xu, J. N. Munday, H. D. Drew, M. S. Fuhrer, L. Hu, *Nat. Commun.* **2014**, *5*, 4224.

30. J. J. Cha, K. J. Koski, K. C. Y. Huang, K. X. Wang, W. Luo, D. Kong, Z. Yu, S. Fan, M. L. Brongersma, Y. Cui, *Nano Lett.* **2013**, *13*, 5913.

31. J. Yao, K. J. Koski, W. Luo, J. J. Cha, L. Hu, D. Kong, V. K. Narasimhan, K. Huo, Y. Cui, *Nat. Commun.* **2014**, *5*, 5670.

32. K. Lu, Z. Hu, Z. Xiang, J. Ma, B. Song, J. Zhang, H. Ma, *Angew. Chem., Int. Ed.* **2016**, *55*, 10448.

33. S. Jiang, K. Krymowski, T. Asel, M. Q. Arguilla, N. D. Cultrara, E. Yanchenko, X. Yang, L. J. Brillson, W. Windl, J. E. Goldberger, *Chem. Mater.* **2016**, *28*, 8071.

34. S. Jiang, S. Butler, E. Bianco, O. D. Restrepo, W. Windl, J. E. Goldberger, *Nat. Commun.* **2014**, *5*, 3389.

35. L. Chen, G. Shi, J. Shen, B. Peng, B. Zhang, Y. Wang, F. Bian, J. Wang, D. Li, Z. Qian, G. Xu, G. Liu, J. Zeng, L. Zhang, Y. Yang, G. Zhou, M. Wu, W. Jin, J. Li, H. Fang, *Nature* **2017**, *550*, 380.

36. P. Ganter, L. M. Schoop, M. Däntl, B. V. Lotsch, *Chem. Mater.* **2018**, *30*, 2557.

37. K. Hantanasirisakul, M.-Q. Zhao, P. Urbankowski, J. Halim, B. Anasori, S. Kota, C. E. Ren, M. W. Barsoum, Y. Gogotsi, *Adv. Electron. Mater.* **2016**, *2*, 1600050.

38. S. Y. F. Zhao, G. A. Elbaz, D. K. Bediako, C. Yu, D. K. Efetov, Y. Guo, J. Ravichandran, K.-A. Min, S. Hong, T. Taniguchi, K. Watanabe, L. E. Brus, X. Roy, P. Kim, *Nano Lett.* **2018**, *18*, 460.

39. S. Jeong, D. Yoo, M. Ahn, P. Miró, T. Heine, J. Cheon, *Nat. Commun.* **2015**, *6*, 5763.

40. J. Buha, L. Manna, *Chem. Mater.* **2017**, *29*, 1419.

41. D. Merg Andrea, Y. Zhou, M. Smith Ashley, E. Millstone Jill, L. Rosi Nathaniel, *ChemNanoMat* **2017**, *3*, 745.

42. P. Ganter, B. V. Lotsch, *Mol. Syst. Des. Eng.* **2019**, Advance Article.

43. K. Szendrei-Temesi, A. Jiménez-Solano, B. V. Lotsch, *Adv. Mater.* **2018**, *30*, 6289.

44. J. Abraham, K. S. Vasu, C. D. Williams, K. Gopinadhan, Y. Su, C. T. Cherian, J. Dix, E. Prestat, S. J. Haigh, I. V. Grigorieva, P. Carbone, A. K. Geim, R. R. Nair, *Nat. Nanotechnol.* **2017**, *12*, 546.

45. P. Ganter, K. Szendrei, B. V. Lotsch, *Adv. Mater.* **2016**, *28*, 7436.

46. S. Stankovich, D. A. Dikin, O. C. Compton, G. H. B. Dommett, R. S. Ruoff, S. T. Nguyen, *Chem. Mater.* **2010**, *22*, 4153.

47. P. Gonzalez Rodriguez, H. Yuan, K. J. H. van den Nieuwenhuizen, W. Lette, D. J. Schipper, J. E. ten Elshof, *ACS Appl. Mater. Interfaces* **2016**, *8*, 28926.

48. W.-S. Hung, C.-H. Tsou, M. De Guzman, Q.-F. An, Y.-L. Liu, Y.-M. Zhang, C.-C. Hu, K.-R. Lee, J.-Y. Lai, *Chem. Mater.* **2014**, *26*, 2983.

49. K. H. Thebo, X. Qian, Q. Zhang, L. Chen, H.-M. Cheng, W. Ren, *Nat. Commun.* **2018**, *9*, 1486.

50. Q. Zhou, Q. Li, S. Yuan, Q. Chen, J. Wang, *Phys. Chem. Chem. Phys.* **2017**, *19*, 29232.

51. Z. Hai, S. Zhuiykov, *Adv. Mater. Interfaces* **2018**, *5*, 1701385.

52. G. M. Whitesides, E. Ostuni, S. Takayama, X. Jiang, D. E. Ingber, *Annu. Rev. Biomed. Eng.* **2001**, *3*, 335.

53. R. G. Chapman, E. Ostuni, L. Yan, G. M. Whitesides, *Langmuir* **2000**, *16*, 6927.

54. D. Qin, Y. Xia, G. M. Whitesides, *Nat. Protoc.* **2010**, *5*, 491.

55. G. M. Whitesides, J. K. Kriebel, B. T. Mayers, *Self-assembly and Nanostructured Materials*, Springer, Berlin, Germany, **2005**.

56. P. Ganter, B. V. Lotsch, *Angew. Chem., Int. Ed* **2017**, *56*, 8389.

57. P. Ganter, L. M. Schoop, B. V. Lotsch, *Adv. Mater.* **2017**, *29*, 1604884.

58. R. M. Tindwa, D. K. Ellis, G.-Z. Peng, A. Clearfield, *J. Chem. Soc., Faraday Trans. 1* **1985**, *81*, 545.

59. Y. Wang, M. Nikolopoulou, E. Delahaye, C. Leuvrey, F. Leroux, P. Rabu, G. Rogez, *Chem. Sci.* **2018**, *9*, 7104.

60. S. Ahmad, P. K. Kanaujia, W. Niu, J. J. Baumberg, G. Vijaya Prakash, *ACS Appl. Mater. Interfaces* **2014**, *6*, 10238.

61. B. Mi, *Science* **2014**, *343*, 740.

62. R. Frisenda, A. J. Molina-Mendoza, T. Mueller, A. Castellanos-Gomez, H. S. J. van der Zant, *Chem. Soc. Rev.* **2018**, *47*, 3339.

63. C. Wang, Q. He, U. Halim, Y. Liu, E. Zhu, Z. Lin, H. Xiao, X. Duan, Z. Feng, R. Cheng, N. O. Weiss, G. Ye, Y.-C. Huang, H. Wu, H.-C. Cheng, I. Shakir, L. Liao, X. Chen, W. A. Goddard Iii, Y. Huang, X. Duan, *Nature* **2018**, *555*, 231.

5 Application of the Amine Intercalation and Exchange for the Transfer of Multilayered Photonic Structures Based on 2D Nanosheets

5.1 Summary

The $H_3Sb_3P_2O_{14}$ nanosheets discussed in the previous chapter are not only suitable for the fabrication of colorimetric thin film sensors, but can also be used as active sensing component in optical 1DPC sensors. With the goal of an advanced sensor design, this project combined several previously known aspects of amine intercalation in $H_3Sb_3P_2O_{14}$: In a first step, we applied amine intercalation in a 1DPC comprised of $H_3Sb_3P_2O_{14}$ nanosheets and TiO_2 nanoparticles to hydrophobize the sensor. Subsequently, the sensor was detached from the substrate by immersion in water with the aid of a sacrificial layer, and transferred to another, arbitrary substrate. Furthermore, the transfer process was combined with the patterning discussed in Chapter 4, to achieve the transfer of 1DPC patterns. Finally, we showed that the sensing capability of the 1DPC was not impaired by the (pattern) transfer process and that the properties can be tailored by amine exchange (known from Chapter 4) or removal post-transfer, which allows a judicious fine-tuning of the sensor properties on demand.

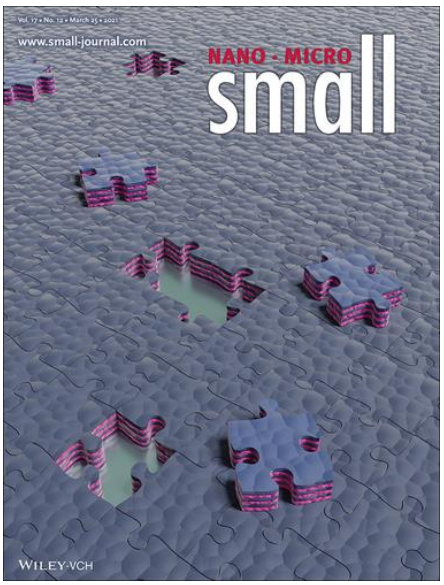

Contributions: Dimitra Chatzitheodoridou and Katalin Szendrei-Temesi conducted preliminary experiments. Marie Däntl and Susanna Guderley fabricated the samples and conducted the measurements. Marie Däntl analyzed the results and edited the figures with the help of Alberto Jiménez-Solano. Marie Däntl wrote the manuscript with the help of all contributing authors.

The project was highlighted as a back cover in the journal *Small*, which was designed by Alberto Jiménez-Solano.

Furthermore, this project was highlighted in the "Women in Materials Science" Virtual Issue, a special collection hosted in Advanced Materials. The issue draws attention to outstanding work in materials science conducted under the lead of female principal investigators to emphasize that gender does not matter when it comes to high impact research.

5.2 Transfer of 1D Photonic Crystals via Spatially Resolved Hydrophobization

The work in this Chapter was reproduced and adapted from:

*Marie Däntl, Susanna Guderley, Katalin Szendrei-Temesi, Dimitra Chatzitheodoridou, Pirmin Ganter, Alberto Jiménez-Solano, and Bettina V. Lotsch**

Published in: *Small* **2021**, *17*, 2007864.

DOI: 10.1002/smll.202007864

https://doi.org/10.1002/smll.202007864

Supporting information can be found in Chapter 8.3.

5.3 Abstract

1D photonic crystals (1DPCs) are well known from a variety of applications ranging from medical diagnostics to optical fibers and optoelectronics. However, large-scale application is still limited due to complex fabrication processes and bottlenecks in transferring 1DPCs to arbitrary substrates and pattern creation. These challenges were addressed by demonstrating the transfer of millimeter- to centimeter-scale 1DPC sensors comprised of alternating layers of $H_3Sb_3P_2O_{14}$ nanosheets and TiO_2 nanoparticles based on a non-invasive chemical approach. By depositing the 1DPC on a sacrificial layer of lithium tin sulfide nanosheets and hydrophobizing only the 1DPC by intercalation of *n*-octylamine via the vapor phase the 1DPC can be detached from the substrate by immersing the sample in water. Upon exfoliation of the hydrophilic sacrificial layer, the freestanding 1DPC remains at the water–air interface. In a second step, it can be transferred to arbitrary surfaces such as curved glass. In addition, the transfer of patterned 1DPCs is demonstrated by combining the sacrificial layer approach with area-resolved intercalation and etching. The fact that the sensing capability of

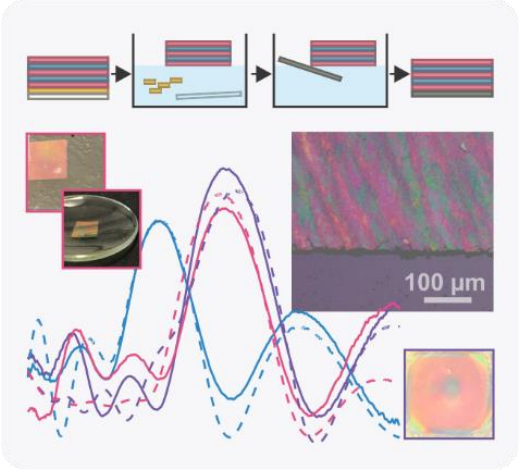

the 1DPC is not impaired and can be modified after transfer renders this method a generic platform for the fabrication of photonic devices.

5.4 Introduction

The vibrant color of inherently colorless materials due to their periodic architecture on the nanoscale is well known in nature. This phenomenon, innate to living organisms such as the skin of a chameleon[1] or butterfly wings,[2] and minerals such as opals, is termed structural color. Compared to the color of most dyes and pigments, which arises due to absorption, structural color is based on diffraction, reflection, and refraction of light.[3] In the past decades many publications have shown that structural color can be achieved synthetically in so-called photonic crystals (PCs), which are prominent for various applications ranging from medical diagnostics[4] and environmental monitoring[5] over sensor technology in food control[6] and photovoltaics[7] to optical fibers[8] and optoelectronics.[9] The reason for their popularity is that they can influence the propagation of electromagnetic waves similar to how semiconductors affect the motion of electrons.[10] Generally, PCs are comprised of two dielectric materials with different refractive indices (RIs) and exhibit optical band structures characterized by photonic bandgaps. PCs are distinguished as 1-, 2-, or 3D periodic structures and the resulting dimensionality of their bandgap in reciprocal space.[10] Ever since their discovery, great efforts have been made to produce new functional PCs due to their wide range of applications.

1D photonic crystals (1DPCs), also referred to as Bragg stacks (BSs), are especially interesting for colorimetric sensing applications where changes in structural color can be induced by external stimuli leading to changes in the RI or thickness changes of the layers, or a combination of both.[11] Since sensors require robust constituent materials, the use of inorganic layered (2D) nanomaterials is beneficial. Furthermore, the need for a large and quick sensing response as well as reversibility is met by 2D nanomaterials as the operation principle of this type of sensor is based on fast and reversible changes of the layer thickness in response to external stimuli, which typically shows a larger effect on the structural color than a change in RI. Moreover, 2D materials bear further advantages for creating structural color such as their chemical and structural diversity[12,13] and the possibility of flexibly fine-tuning their properties through modification.[14] This makes them even more versatile in their applicability, especially regarding the current challenge of progressive miniaturization. We have recently shown that the layered phosphatoantimonic acid $H_3Sb_3P_2O_{14}$ is a promising 2D material for sensory applications due to its excellent swelling behavior upon exposure to vapors as well as the

possibility to fine-tune the properties post-synthetically in a gradual and reversible fashion.[15] Specifically, the sensitivity towards certain vapors can be modified through intercalation of primary alkylamines, which also influences the overall hydrophobicity of the sample.[16,17] Combining this material with TiO_2 nanoparticles leads to highly reflective BSs that exhibit and enhance the properties of the inorganic nanosheets.[18,19]

Especially in the field of optoelectronic applications, it is of great interest to further enhance the adaptability and flexibility of sensors in terms of being able to transfer them to arbitrary surfaces with different physicochemical characteristics. Several approaches, such as polymer infiltration and peel off,[20-23] contact printing[24] or the use of a sacrificial layer[25,26] are known for thin film transfer. For example, peeling off polymer infiltrated hybrid films has been shown for UV protecting surface coatings comprised of TiO_2 and ZrO_2.[27] However, for sensing, this method is challenged by the fact that the active material component is blocked and hence the functionality is limited after the transfer. Therefore, one of the remaining key challenges is the design of a transfer method for BSs that does not impair their optical quality and stimuli-responsiveness.

This can be achieved either with contact printing or with the use of a sacrificial layer that can be removed selectively. For example, wet etching of a sacrificial layer was successfully applied for the fabrication of transferable $LiFe_5O_8$[25] or $CoFe_2O_4$[26] thin films, which are interesting candidates for flexible electronics. The challenge in this transfer approach lies in finding a material, which can be removed while the multilayer stack itself stays unaffected.

Inspired by the sacrificial layer method, we herein address the need for transferable sensors and report a facile, gentle, and cost-effective transfer procedure that exploits the possibility of hydrophobizing the $H_3Sb_3P_2O_{14}/TiO_2$ BSs by intercalation with *n*-octylamine (C8; 1M in ethanol), while the used sacrificial lithium tin sulfide (LTS) layer remains hydrophilic. Since LTS is not protonated and no stable intercalation with the amines occurs, this chemical approach allows the detachment of the BS from the substrate by immersing it in water, leaving the freestanding hydrophobic BS on the water surface. This opens up the possibility of transferring the sensor to arbitrary surfaces where the multilayer deposition is not trivial without some additional treatment, such as curved glass, metals or PDMS, and hence widens the overall applicability. Furthermore, it is important to note that amine intercalation does not impair the sensitivity of the sensor but only changes the sort of stimuli it reacts on. The transferred BS stays accessible to external stimuli and the sensitivity towards analytes can be

remodified by amine removal or exchange. Ultimately, this method can be utilized in combination with a previously reported patterning method to enable BS pattern transfer.[17]

5.5 Results and Discussion

5.5.1 Bragg Stack Transfer

BSs comprised of alternating layers of $H_3Sb_3P_2O_{14}$ nanosheets and TiO_2 nanoparticles (Experimental Section is given in ESI) were chosen as a platform for film transfer with the aid of a water soluble sacrificial layer (LTS) as they exhibit high reflectivity and can easily be hydrophobized by intercalating C8 over the vapor phase.[19] Briefly, the 1DPCs consisting of 4-5 bilayers were deposited on LTS coated glass substrates via the spin-coating technique and exposed to *n*-octylamine (1M in ethanol) vapor for hydrophobization. Note that *n*-octylamine was chosen for these experiments as *n*-butylamine and *n*-hexylamine are not hydrophobic enough and *n*-decylamine or non-linear alkylamines increase the intercalation time drastically due to their lowered volatility. During the amine intercalation, LTS is barely affected by the amine while the BS itself readily intercalates the molecules and therefore exhibits increased hydrophobicity (Fig. S5.2, Supporting Information). Due to exfoliation of the hydrophilic LTS upon immersion of the sample in de-ionized (DI) water (≈2 h), the BS could be detached from the substrate leaving a freestanding BS floating on the water surface, which could be collected by an arbitrary substrate. The duration of the water immersion was optimized to enable the transfer of the BS without damages. Shorter immersion times often did not show satisfactory results as it led to incomplete transfer or breakage of the BS. This may be due to the fact that the sacrificial layer did not fully exfoliate in the given time. Note that a rectangular part of the BS was cut with a glass cutter prior to water immersion to make sure only the homogeneous part in the middle of the sample is transferred and to assist the detachment from the substrate. The inhomogeneous parts of the sample at the edges of the substrate arise from the spin-coating process and do not detach from the substrate nicely, which may arise from the large amount of structural defects around the perimeter of the sample and differences in layer thickness distribution. The remaining inhomogeneous edges, which are left on the substrate after the transfer of the rectangular homogeneous part, is shown in Fig. 5.1d on the right. A scheme of the transfer process is given in Fig. 5.1a. In order to ensure conformal adhesion of the transferred BS to the new substrate and remove excess water, which might be present in the structure, the sample was heated to 90 °C for 15 min. The reflectance measurements in Fig. 5.1b show data obtained for the pristine BS (blue) along with the amine intercalated

(purple) and the transferred sample (pink). Upon intercalation the Bragg peak shifts from the blue towards the red spectral region indicative of an increase of the interlayer distance of the nanosheets and therefore of the overall layer thickness. As we expect that the transfer does not affect the thickness of the BS, the Bragg peak of the transferred sample should not be significantly shifted in comparison to the one of the amine-intercalated sample, which is confirmed by these measurements. However, the reflectance seems to be slightly decreased after the transfer, which may arise from inhomogeneous adhesion to the new substrate as the high frequency oscillations observed in the spectrum, and also the absence of the LTS layer in the transferred structure suggest. Also, an increase in structural defects and especially in surface roughness can cause the appearance of diffuse reflection, which leads to a decrease in the specular reflectance measured here. The dashed lines (color code corresponding to that of the solid lines) in Fig. 5.1b show the theoretically modeled optical responses. In all cases, the experimentally obtained peaks are in good agreement with the theoretical values. The calculations were obtained similar to a previously reported approach applying the transfer matrix method (TMM).[19]

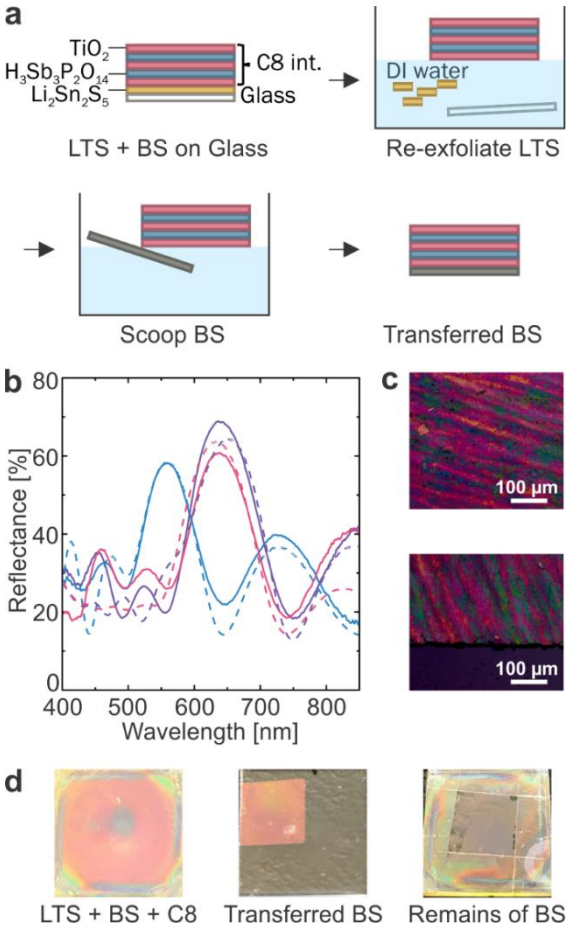

Fig. 5.1 (a) Schematic description of the BS transfer with the aid of a sacrificial layer. (b) Reflectance spectra of the pristine BS (blue), the C8 intercalated BS (purple), and the transferred BS (pink). Theoretically calculated Bragg peaks are shown as dashed lines. (c) Images of the transferred BS taken at 100x magnification with a camera attached to an optical microscope. Top: middle of the sample, bottom: clean edge of the sample. (d) Photographs of the amine intercalated BS (left), the transferred BS (middle), and the remains of the sample after the transfer (right). The substrate size is 1.5 × 1.5 cm.

Compared to previously reported techniques that do not rely on polymer infiltration for stabilization,[25,26] the herein reported method allows the transfer of large BS pieces (Fig. 5.1c, 8 × 7 mm) with clear edges and without impairing the sample's sensing capabilities. Further, the microscope images in Fig. 5.1d confirm that the 1DPC is not cracked and that the edges are preserved with high fidelity. Therefore, it can be assumed that the transfer conditions are rather gentle compared to other multistep or etching methods. Note that the transfer from one glass substrate to another one is displayed in Fig. 5.1d to ensure comparability, but in general, other substrates such as silicon wafers or metals can be used as final substrate as well (Fig. S5.6, Supporting Information).

5.5.2 Bragg Stack Patterning

The possibility of transferring the BSs to arbitrary and curved surfaces opens up a wide application range including advanced electronics, coatings, or solvent vapor sensors and represents a simple and cost-effective approach, which could meet industrial needs. Since micrometer scale patterning or pattern transfer of thin films has gained increasing research interest in the past few years,[22,28-30] we applied a soft chemical lithography method including spatial amine intercalation for hydrophobization, which was reported previously on $H_3Sb_3P_2O_{14}$ thin films.[17] Using this method on the BSs opens up the possibility of combining patterning and transfer in one step. Patterning experiments were performed with BSs (four bilayers of $H_3Sb_3P_2O_{14}$ and TiO_2) deposited directly on glass substrates. In order to ensure spatially resolved intercalation, the exposure of the sample towards *n*-octylamine vapor was conducted with the aid of a mask. The non-intercalated (hydrophilic) parts were subsequently removed by repeatedly pipetting DI water over the mask-free sample, leaving the hydrophobized pattern on the substrate. This process is described schematically in Fig. 5.2a. The microscope images in Fig. 5.2b show that the intercalation with the mask leads to clear edges (purple) as well as a pink zone that is caused by lateral diffusion of the amines in the BS. However, the concentration of the amines in this diffuse laterally intercalated zone is too small to hydrophobize the sample and therefore this part of the sample can easily be washed away (see Fig. S5.8 in the Supporting Information), leaving a clear edge at the border of the mask-intercalated part of the sample and the clean substrate. This is further confirmed by the photographs of the patterned sample before (top) and after (bottom) washing (Fig. 5.2c). In Fig. 5.2d it is shown that amine intercalation leads to a redshift of the Bragg peak (purple) compared to the one of the pristine sample (blue). Furthermore, a minor blueshift of the Bragg peak after the washing process (pink) is indicated. We attribute this to the fact that some of the intercalated amines get washed out of the structure during the process and thus decrease the overall layer thickness of the BS.

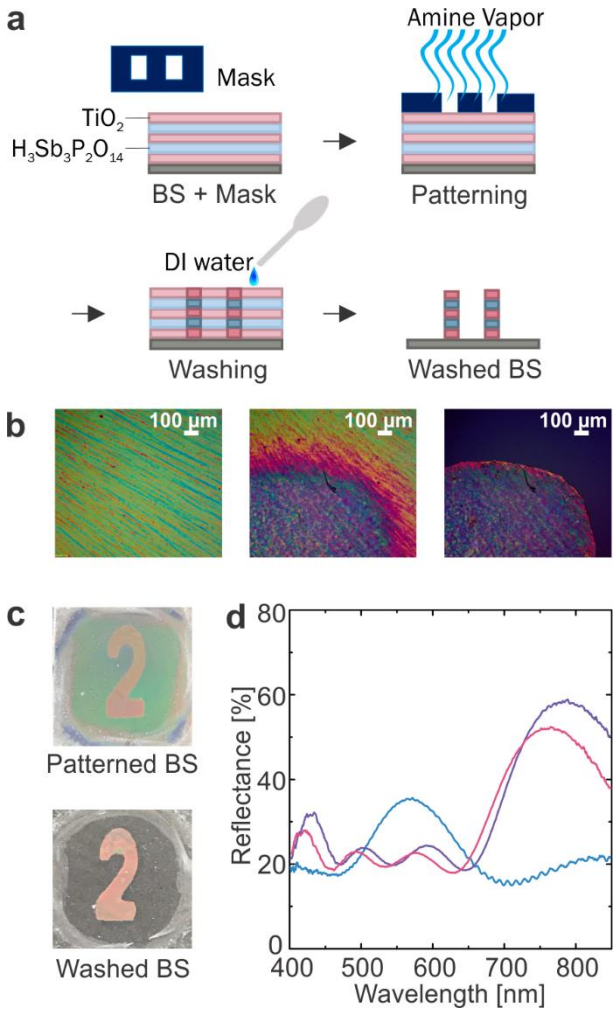

Fig. 5.2 (a) Schematic description of the BS patterning process. (b) Microscope images (100x magnification) of the pristine BS (left), the BS intercalated with amines using a mask (middle), and the BS after washing away the hydrophilic part (right). (c) Photograph of the patterned BS (top) along with the patterned BS after removal of the hydrophilic surrounding (bottom). The substrate size is 1.5 × 1.5 cm. (d) Reflectance measurements of the pristine BS (blue), the amine intercalated part of the pattern (purple), and the pattern after the washing step (pink).

5.5.3 Bragg Stack Pattern Transfer

The results we obtained by combining both patterning and transfer are given in Fig. 5.3. For these experiments, 1DPCs with five bilayers of $H_3Sb_3P_2O_{14}$ and TiO_2 were deposited on a glass substrate that was previously coated with the sacrificial layer. The spatial intercalation was achieved via a mask as described above, while this time the washing of the patterned sample was not conducted with a pipette but rather solely by immersion of the sample in DI water. After the sacrificial layer as well as the non-intercalated parts of the BS were re-exfoliated/dissolved by the water, the hydrophobic, patterned BS was detached from the substrate by dipping it into the water and collecting it from the water surface with another substrate. Again, the adhesion to the new substrate was improved by heating the sample to

90 °C for 15 min. Similar to the BS transfer experiment, the reflectance measurements (Fig. 5.3a) exhibit a redshift of the Bragg peak (blue) upon amine intercalation (purple) and barely no shift after the pattern transfer (pink). Specifically, the BS pattern seems to have been transferred completely with only marginal damage. This fact is further supported by the microscope images in Fig. 5.3b,d, which show that clean edges can be preserved. Since this pattern transfer is a facile two-step method and relies on endowing the 1DPC with hydrophobicity by amine intercalation it is imaginable that this approach is generic and can be applied to other heterostacks or thin films as well.

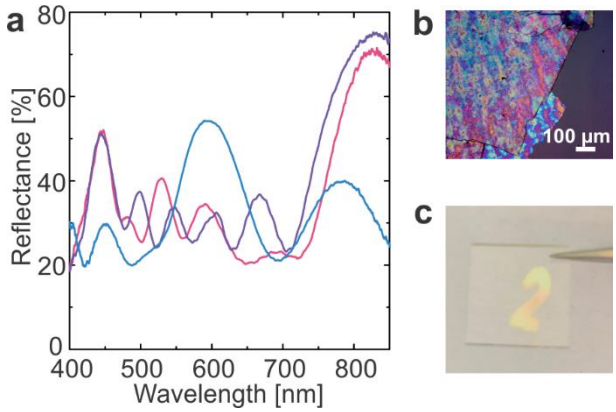

Fig. 5.3 (a) Reflectance measurements of the non-intercalated BS (blue), the amine intercalated pattern before transfer (purple), and the pattern after transfer and removal of the hydrophilic part (pink). (b) Image of the edge of the transferred BS pattern taken at 100x magnification. (c) Photograph of the transferred BS pattern. The substrate size is 1.5 × 1.5 cm.

5.5.4 Bragg Stack Transfer to Non-coatable Substrates

Furthermore, this new 1DPC transfer approach makes it possible to solve the problem of deposition of dielectric multilayers on certain substrates where up to now an additional processing step was necessary. For depositing the 1DPC on curved glass, which cannot be spin-coated in a homogeneous manner directly, the transfer is a simple and convenient method. The 1DPCs used for this experiment were fabricated, intercalated, and transferred to a watch glass dish by the same approach as described in Fig. 5.1. As seen in the previous reflectance measurements, the measurements in Fig. 5.4a exhibit a redshift of the intercalated sample (purple) compared to the pristine one (blue) and barely no shift after the pattern transfer (pink) compared to the one before the transfer (purple). However, the reflectance seems to be decreased slightly upon transfer. This may be due to the difficulties in measuring the specular reflectance of the sample on the curved substrate or defects in the sample. Being able to transfer the BSs to a curved surface may allow their integration in light emitting devices in which curved substrates or covers are required.[31-33]

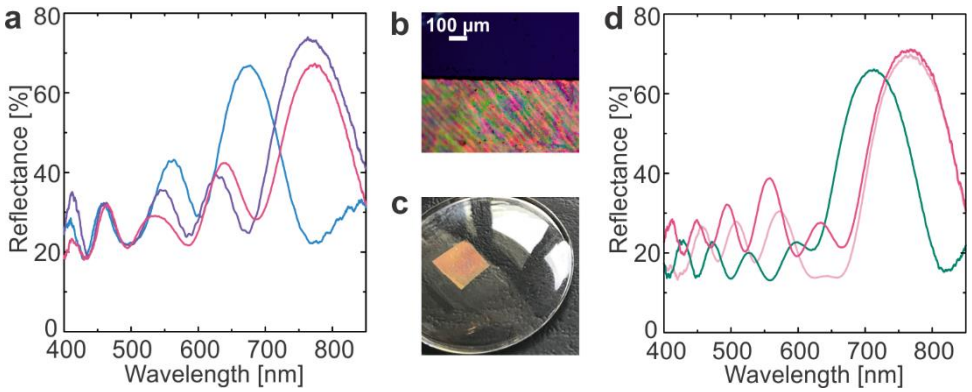

Fig. 5.4 (a) Reflectance measurements of the pristine BS (blue), the amine intercalated BS before transfer (purple), and the BS after transfer to the curved substrate (pink). (b) Image of the edge of the transferred BS pattern taken at 100x magnification. (c) Photograph of the transferred BS on a curved glass substrate. (d) Reflectance measurements of an *n*-octylamine intercalated BS transferred to a curved substrate (pink), the same sample after the amine exchange of *n*-octylamine with ethylamine (green), and the same sample after the amine exchange of ethylamine with *n*-octylamine (light pink).

Apart from demonstrating the transfer of BSs and patterns thereof to various substrates, we can also tailor the hydrophobicity and therefore the sensing response of the 1DPCs after the transfer. In order to allow the transfer in water, the BS had to be hydrophobized to ensure that it does not get damaged upon immersion. However, the intercalation does not impair the sensing capabilities of the BS but rather modifies their responsiveness towards different vapors dependent on the chain length of the primary alkylamine used for intercalation. Therefore, different amines can be utilized to endow the BSs with hydrophilic or hydrophobic properties, which in turn changes the response towards different types of analytes. Since we have previously developed a method for flexible, postsynthetic exchange of primary alkylamines in $H_3Sb_3P_2O_{14}$-based thin films,[17] we applied this protocol to the transferred BSs, giving rise to a versatile platform for adaptable sensors. This was demonstrated exemplarily by exchanging the *n*-octylamine by ethylamine (1 m in ethanol). In Fig. 5.4 the Bragg peak of the *n*-octylamine intercalated sample after the transfer to a curved substrate (pink) is compared to the Bragg peak of the same sample after exchanging *n*-octylamine with ethylamine over the vapor phase (green). The clear blue-shift indicates a decrease in layer thickness, which evidences the exchange of the longer amines (hydrophobic) for the shorter ones (hydrophilic) and therefore suggests a change of hydrophobicity and thus an altered sensing response (see Fig. S5.4 in the Supporting Information) of the sample. Subsequently, the ethylamine intercalated sample can be re-modified with *n*-octylamine in the same manner (light pink), which underlines the reversibility as well as the flexibility of the applied protocol.

5.5.5 Regeneration of the Pristine Bragg Stack after Transfer

In this work it could be shown that the properties and hence the sensing capability cannot only be remodified with different amines but also the pristine sensor can be regenerated (Fig. S5.4 and Fig. S5.7, Supporting Information). Since ethylamine is small and quite volatile compared to the longer primary alkylamines it is possible to remove this amine from the sample by heat treatment (24 h, 70 °C). Therefore, it is possible to recover the pristine structure applying a two-step protocol to the *n*-octylamine containing transferred or patterned sample consisting of *n*-octylamine exchange with ethylamine and subsequent heat treatment.[17] This is supported by the fact that the sensing response of the regenerated transferred BS, which results in a red-shift of the Bragg peak upon exposure to ethanol vapor, is very similar to that of the pristine sample (see Fig. S5.4 in the Supporting Information) while the ethylamine intercalated one shows an increased response. Furthermore, scanning electron microscopy was conducted to show the morphology of the BS before and after intercalation and to determine if the BS integrity is maintained in a transferred, regenerated sample. The obtained cross section images are given in Fig. S5.5 in the Supporting Information.

5.6 Conclusion

In summary, we have demonstrated a generic method to transfer 1DPCs to arbitrary surfaces without impairing their colorimetric sensing capabilities by using a sacrificial layer approach. 1DPCs comprised of alternating $H_3Sb_3P_2O_{14}$ and TiO_2 layers, which were deposited on top of a sacrificial LTS layer, were first hydrophobized by intercalation of *n*-octylamine via the vapor phase. Since the LTS remained hydrophilic, immersion of the sample in water led to exfoliation of the sacrificial layer and therefore the BS was detached from the substrate. The millimeter- to centimeter-scale freestanding BS could be collected by various substrates, including those on which it could not have been grown directly, thus leveraging a platform for the creation of sophisticated optical devices. Importantly, the possibility of using the BS as a colorimetric sensor is not impaired by the reported transfer method. In addition, the BS can be remodified with other primary alkylamines or the amines can be removed by heat treatment to tune its polarity and intercalation properties; therefore, further enlarging the scope of applications. Prediction of the optical properties of the transferred BS using the transfer matrix method opens up the possibility for rationally designing applications in lighting control.

Finally, we showed that a soft chemical patterning method, previously applied to $H_3Sb_3P_2O_{14}$ thin films, can also be used to pattern the BSs. Combining the sacrificial layer approach with

area-resolved intercalation and etching enables the possibility of patterning and transfer of the BSs in an economic and cost-efficient two-step manner. As amine intercalation into layered materials has been frequently reported in the past,[16,17,34-36] this method is expected to be applicable to a range of host materials.

5.7 Acknowledgements

Financial support was granted by the Max Planck Society, the University of Munich (LMU), the Center for Nanoscience and the Cluster of Excellence e-conversion. The authors thank C. Schneider for LTS synthesis, A. Mähringer for assistance with water contact angle measurements and V. Duppel for the acquisition of SEM images. A.J.-S. gratefully acknowledges a postdoctoral scholarship from the Max Planck Society.

Open access funding enabled and organized by Projekt DEAL.

5.8 Conflict of Interest

The authors declare no conflict of interest.

5.8 References

1. J. Teyssier, S. V. Saenko, D. van der Marel, M. C. Milinkovitch, *Nat. Comm.* **2015**, *6*, 6368.
2. B. A. Bober, J. K. Ogata, V. E. Martinez, J. J. Hallinan, T. A. Leach, B. Negru, *J. Chem. Educ.* **2018**, *95*, 1004.
3. J. Sun, B. Bhushan, J. Tong, *RSC Adv.* **2013**, *3*, 14862.
4. Y. Lu, S. Peng, D. Luo, A. Lal, *Nat. Comm.* **2011**, *2*, 578.
5. F. Wang, Z. Meng, F. Xue, M. Xue, W. Lu, W. Chen, Q. Wang, Y. Wang, *Trends Environ. Anal. Chem.* **2014**, *3*, 1.
6. L. D. Bonifacio, G. A. Ozin, A. C. Arsenault *Small* **2011**, *7*, 3153.
7. F. Priolo, T. Gregorkiewicz, M. Galli, T. F. Krauss, *Nat. Nanotechnol.* **2014**, *9*, 19.
8. J. C. Knight, *Nature* **2003**, *424*, 847.
9. E. C. Nelson, N. L. Dias, K. P. Bassett, S. N. Dunham, V. Verma, M. Miyake, P. Wiltzius, J. A. Rogers, J. J. Coleman, X. Li, P. V. Braun, *Nat. Mater.* **2011**, *10*, 676.
10. J. D. Joannopoulos, S. G. Johnson, J. N. Winn, R. D. Meade, *Photonic Crystals: Molding the Flow of Light*, Princeton University Press, Princeton, NJ, USA, **2011**.
11. B. V. Lotsch, G. A. Ozin, *Adv. Mater.* **2008**, *20*, 4079.

12. V. Nicolosi, M. Chhowalla, M. G. Kanatzidis, M. S. Strano, J. N. Coleman, *Science* **2013**, *340*, 1226419.

13. R. Ma, T. Sasaki, *Adv. Mater.* **2010**, *22*, 5082.

14. J. Wan, S. D. Lacey, J. Dai, W. Bao, M. S. Fuhrer, L. Hu, *Chem. Soc. Rev.* **2016**, *45*, 6742.

15. P. Ganter, K. Szendrei, B. V. Lotsch, *Adv. Mater.* **2016**, *28*, 7294.

16. P. Ganter, L. M. Schoop, M. Däntl, B. V. Lotsch, *Chem. Mater.* **2018**, *30*, 2557.

17. M. Däntl, P. Ganter, K. Szendrei-Temesi, A. Jiménez-Solano, B. V. Lotsch, *Nanoscale Horiz.* **2020**, *5*, 74.

18. K. Szendrei, P. Ganter, O. Sànchez-Sobrado, R. Eger, A. Kuhn, B. V. Lotsch, *Adv. Mater.* **2015**, *27*, 6341.

19. K. Szendrei-Temesi, A. Jiménez-Solano, B. V. Lotsch, *Adv. Mater.* **2018**, *30*, 6289.

20. M. E. Calvo, H. Míguez, *Chem. Mater.* **2010**, *22*, 3909.

21. M. E. Calvo, L. González-García, J. Parra-Barranco, A. Barranco, A. Jiménez-Solano, A. R. González-Elipe, H. Míguez, *Adv. Opt. Mater.* **2015**, *3*, 171.

22. W. Ma, S. Li, D. Kou, J. L. Lutkenhaus, S. Zhang, B. Tang, *Dyes Pig.* **2019**, *160*, 740.

23. M. E. Calvo, O. Sanchez Sobrado, G. Lozano, H. Miguez, *J. Mater. Chem.* **2009**, *19*, 3144.

24. C. Linghu, S. Zhang, C. Wang, J. Song, *npj Flexible Electron.* **2018**, *2*, 26.

25. L. K. Shen, L. Wu, Q. Sheng, C. R. Ma, Y. Zhang, L. Lu, J. Ma, J. Ma, J. H. Bian, Y. D. Yang, A. P. Chen, X. L. Lu, M. Liu, H. Wang, C.-L. Jia, *Adv. Mater.* **2017**, *29*, 1702411.

26. Y. Zhang, L. Shen, M. Liu, X. Li, X. Lu, L. Lu, C. Ma, C. You, A. Chen, C. Huang, L. Chen, M. Alexe, C.-L. Jia, *ACS Nano* **2017**, *11*, 8002.

27. J. R. C. Smirnov, M. E. Calvo, H. Míguez, *Adv. Funct. Mater.* **2013**, *23*, 2805.

28. Y.-L. Loo, R. L. Willett, K.W. Baldwin, J. A. Rogers, *Appl. Phys. Lett.* **2002**, *81*, 562.

29. Z. Wang, J. Zhang, J. Xie, Y. Yin, Z. Wang, H. Shen, Y. Li, J. Li, S. Liang, L. Cui, L. Zhang, H. Zhang, B. Yang, *ACS Appl. Mater. Interfaces* **2012**, *4*, 1397.

30. K. Lodewijks, V. Miljkovic, I. Massiot, A. Mekonnen, R. Verre, E. Olsson, A. Dmitriev, *Sci. Rep.* **2016**, *6*, 28490.

31. T. Hamaguchi, M. Tanaka, H. Nakajima, *Jpn. J. Appl. Phys.* **2019**, *58*, SC0806.

32. A. Jiménez-Solano, J. F. Galisteo-López, H. Míguez, *Adv. Opt. Mater.* **2018**, *6*, 1700560.

33. C.-A. Chuang, M.-H. Lin, B.-X. Yeh, C.-H. Ho, *RSC Adv.* **2018**, *8*, 2733.

34. P. Ganter, L. M. Schoop, B. V. Lotsch, *Adv. Mater.* **2017**, *29*, 1604884.

35. R. M. Tindwa, D. K. Ellis, G.-Z. Peng, A. Clearfield, *J. Chem. Soc., Faraday Trans. 1* **1985**, *81*, 545.

36. A. J. Jacobson, J. W. Johnson, J. T. Lewandowski, *Mater. Res. Bull.* **1987**, *22*, 45.

6 Towards a Fundamental Understanding of the Amine Exchange: Real Time Tracking of the Amine Intercalation Mechanism in 2D Nanosheet-based Fabry-Pérot Thin Films

6.1 Summary

Since we assume that the intercalation of amines in other layered materials is generic, this project aims to gain a basic understanding of the process, especially when the intercalation is solvent-mediated. Therefore, fundamental insights into the mechanism and kinetics are highly sought after, because they can be used to rationally design the intercalation in other nanosheet-based systems, potentially paving the way for novel applications. In this project, we demonstrated a novel approach for the quantitative analysis of changes in the peak profile and position observed in *in situ* X-ray diffraction patterns during the intercalation of *n*-butylamine in an $H_3Sb_3P_2O_{14}$ thin film. This allowed us to elucidate the mechanism of competing amine-solvent intercalation.

Contributions: Marie Däntl coordinated the project and fabricated the samples. Marie Däntl designed the measurement setup with the help of Alberto-Jiménez-Solano, Hugo Vignolo-Gonzalez and Peter Wochner. Marie Däntl and Johannes Maschita conducted the measurements with the help of Alberto Jiménez-Solano, Hugo Vignolo-Gonzalez and Peter Wochner. Marie Däntl analyzed the data and selected the relevant files for the fittings. Sebastian Bette developed the fitting routines and conducted the fittings and simulations. Marie Däntl and Sebastian Bette edited the figures and wrote the manuscript with the help of all contributing authors.

6.2 Protocol for the Analysis of Real-Time XRD Data of Intercalation Processes in Thin Films Demonstrated for Amine Intercalation in $H_3Sb_3P_2O_{14}$ Thin Films

The work in this Chapter was reproduced and adapted from:

Marie Däntl, Johannes Maschita, Peter Wochner, Alberto Jiménez-Solano, Hugo A. Vignolo-González, Daniel Putzky, Robert E. Dinnebier, Sebastian Bette, Bettina V. Lotsch**

Submitted

Supporting information can be found in Chapter 8.4.

6.3 Abstract

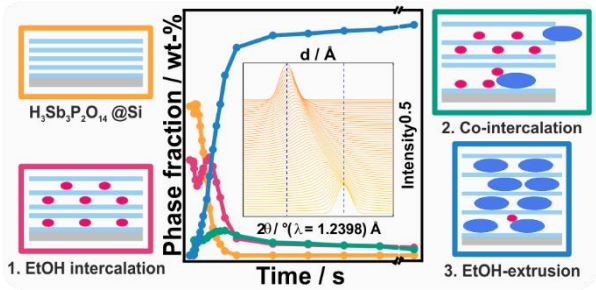

Thin films comprised of 2D layered materials have attracted significant attention as they can be assembled into novel functional materials. However, to further enhance their application range, for example in miniaturized sensors, it is necessary to harvest the large property space of 2D materials by fine-tuning them on a molecular level. Intercalation, among other methods, has been explored to this end. In order to fully exploit the potential of intercalated 2D materials and to design their properties, it is vital to gain a fundamental understanding of the underlying intercalation mechanism. In this work, we present a novel method for the analysis of the peakshift observed by *in situ* X-ray diffraction measurements upon intercalation of the guest molecule in the layered host. We do this by exemplarily applying it to a dataset collected for the real time monitoring of the intercalation of *n*-butylamine (3M in ethanol) into an $H_3Sb_3P_2O_{14}$ thin film. Using this approach, we reveal the transient formation of intermediates and the critical role of ethanol, which acts as a vehicle for amine intercalation into the layered host.

6.4 Introduction

Since the discovery of graphene,[1] a variety of other inorganic layered materials, such as transition metal dichalchogenides (TMD),[2] layered double hydroxides,[3] Zintl phases,[4] MXenes[5] or transition metal oxides[6] have been exfoliated into so-called two-dimensional (2D)

nanosheets. These materials exhibit properties that are distinct from those of their bulk counterparts, which has recently lead to a resurge in research interest in their parent, layered materials.[7-11] In addition, the assembly of 2D materials into van der Waals (vdW) heterostructures with novel properties has gained significant momentum, further amplified by the discovery that rotational degrees of freedom in such superlattices can be used to fine-tune their electronic properties (twistronics).[12] The fact that the physical or chemical properties of layered and 2D vdW solids can be further modified by intercalation opens up new avenues to tailored solids for applications in quantum technologies,[13] catalysis,[14] sensing[15] and (opto)electronics.[16,17]

Taking a step back, the change of the physical and chemical properties of the layered bulk materials by intercalation has already been studied in the 1970s and 80s. For example, the critical temperature for superconductivity has been modified in TaS_2 and other layered sulfides by intercalation of various alkylamines.[18] Furthermore, the intercalation of primary alkylamines has also been applied to a broad range of inorganic layered oxide bulk materials, e.g. α–zirconium, α–titanium and α-tin phosphates.[19-21] In these cases, amine intercalation can be considered as an acid-base reaction between the negatively charged layers of the acidic host and the Brönsted-base amines. The latter are protonated during the reaction and therefore trapped between the layers of the host material. This rational tuning of the interlayer space opened up applications in the field of sorption, among others. For example, it was shown that the intercalation of propylamine in α-titanium phosphate significantly improved the materials ability for sorption of Eu^{3+}, which is often considered as a chemical analogue for other trivalent heavy metals (e.g. lanthanides and actinides).[22]

In parallel with these findings, layered antimony phosphates ($H_nSb_nP_2O_{5+3n}$ with n = 1, 3) and their ability to exchange ions, e.g., alkali metal ions, lanthanides, and actinides, as well as the possibility of intercalating water molecules were discovered.[23-25] In recent experiments we have shown that the intercalation of primary alkylamines can also be applied to antimonyphosphates, which was achieved in a facile manner over the vapor phase.[26,27] Specifically, the material was exfoliated into nanosheets and thin films were fabricated in order to exploit and combine the properties of the 2D material with the versatility of amine intercalation for modifying the materials properties, e.g. for sensing applications.[26,28] Moreover, we demonstrate amine exchange reactions which allowed for the control of the structural and

dielectric properties of amine intercalated thin films such as polarity, effective refractive index, film thickness, and sensitivity towards solvent vapors.[29]

Apart from the interesting fundamental properties of 2D layered materials not only the assembly into novel functional materials but also the fine-tuning of their properties on a molecular level, e.g. by chemical intercalation, are of great importance for applications in nanoscale science, optoelectronics,[16] superconductivity,[18] or sensing.[15] In order to design functional materials based on the intercalation of 2D nanosheets it is essential to gain a fundamental understanding of the intercalation mechanism. Given the variety of layered materials that can host amine molecules, we expect that the amine intercalation in nanosheet-based thin films is generic. Towards this end, the real-time monitoring of such intercalation processes is of particular interest to gain a fundamental understanding of the intercalation mechanism and kinetics in order to further enhance the design of 2D nanosheet-based materials for a wide range of applications. Even though intercalation compounds are mostly characterized by X-ray diffraction (XRD), the interpretation of the observed peak shift upon insertion of a guest species is not trivial. When probed in specular reflection geometry, the resulting diffraction patterns only exhibit the 00*l* reflections due to the preferred orientation of the nanosheets parallel to their substrate and therefore the observed reflection corresponds to the interlayer distance. Since intercalation is often mediated by solvents[13,30,31] and hence a competing reaction of the intercalant and the solvent may occur, it is important to take this into account when analyzing the peak shift. In this work, we address this challenge by developing a novel method for the analysis of the peakshift observed by *in situ* X-ray diffraction measurements upon insertion of the guest molecule in the layered host. The method consists of the quantitative refinement of the peak position and profile in the XRD pattern by a DIFFaX-like recursive approach implemented into the TOPAS software, compared to the presently used approaches. We present our method by applying it to a dataset collected for the real-time monitoring of the intercalation of *n*-butylamine (3M in ethanol) into an $H_3Sb_3P_2O_{14}$ thin film. We are able to extract different interlayer distances and intercalation probabilities for the multi-step intercalation, and considering two different faulting scenarios, we propose a mechanism based on the competing intercalation of ethanol and amine.

6.5 Results and Discussion

The intercalation of atoms, ions or molecules in layered materials leads to a significant alteration of the crystal structure, which is reflected by changes in the diffraction pattern.[32]

Hence, diffraction techniques using X-rays, neutrons or electrons are a suitable and facile tool for monitoring intercalation processes. However, when it comes to intercalation into thin films, these techniques reach their limit as the diffraction pattern is reduced to a few signals due to the two-dimensional character of the specimen and the rigid orientation of the crystallites parallel to the substrate. Therefore, often only one peak, the so-called basal reflection, i.e. the reflection attributed to the interlayer distance, can be observed by investigation of a thin film using X-ray diffraction. During intercalation processes in-between the layers, the position and shape of the reflection changes, and sometimes even splitting of this reflection occurs.[33,34] In the following, we demonstrate a method for a quantitative analysis of the changes in peak shape and position of the basal reflection during ethanol mediated amine intercalation in-between $H_3Sb_3P_2O_{14}$ layers.

6.5.1 X-ray Diffraction (XRD)

The vapor phase intercalation of butylamine dissolved in ethanol (EtOH) was monitored in real-time (one measurement every second) by *in situ* XRD using a sample chamber equipped with the antimony phosphate thin film, a syringe for injection of the amine solution, and a constant He-flow to prevent air scattering during the measurement. Excerpts of the *in situ* XRD patterns are shown in Fig. 6.1a and b. In the following, we describe the observed changes in peak position and peak shape during the intercalation experiment. Based on these observations, we set up scenarios, i.e. faulting scenarios, for randomly occurring intercalation in-between stacks of $H_3Sb_3P_2O_{14}$ layers. Subsequently, recursive simulations of XRD patterns with varying intercalation probabilities, i.e. fault probabilities, are employed to validate the faulting scenarios. After determining the expansion of the interlayer distance upon ethanol, amine, and ethanol and amine co-intercalation, we perform fully weighted Rietveld refinements of the *in situ* XRD patterns collected at different stages of the intercalation process for extraction of the fault probabilities. Based on the evolution of the probability for ethanol, amine, and ethanol and amine co-intercalation, conclusions on the mechanism of ethanol mediated amine intercalation in-between $H_3Sb_3P_2O_{14}$ layers can be drawn.

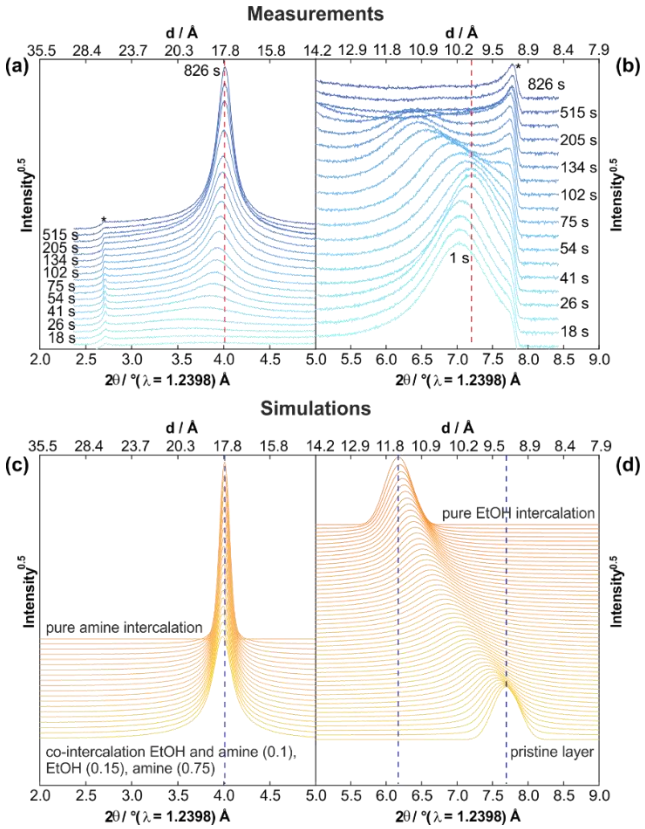

Fig. 6.1 Excerpts of *in situ* XRD patterns of an $H_3Sb_3P_3O_{14}$ thin film recorded during the intercalation of amine in the 2θ regions, corresponding to *d*-spacings of (a) amine intercalated and (b) pristine layers. Recursive XRD pattern simulations of the diffraction effects of a modulation of the interlayer distances by (c) random interstratification of amine (probability 0.75 to 1), ethanol (probability 0.15 to 0) and both amine and ethanol (probability 0.1 to 0) between the $H_3Sb_3P_3O_{14}$ layers and (d) random interstratification of ethanol between the pristine $H_3Sb_3P_2O_{14}$ layers with a fault probability from 0 to 1. The dashed blue line corresponds to interlayer distances of pristine (d = 9.24 Å, 7.69° 2θ), ethanol (d = 11.51 Å, 6.15° 2θ), and amine (d = 17.72 Å, 4.01° 2θ) intercalated layers. Note that the asterisks in (a) and (b) mark the cut-off of the detector.

Initially (after 1 s; no amine solution in the chamber) only one reflection is present in the XRD pattern at 7° 2θ, corresponding to the mean interlayer distance of the spin-coated film of 10.2 Å (Fig. 6.1b). Note that the amine solution was injected 10 s after the measurement was started in order to collect data on the sample before intercalation. Therefore, we use two time scales in the following: the time that has passed from the start of the experiment and the time that has passed from the time of the amine injection, which differs by 10 s. During the intercalation process in the thin film, the peak initially shifts towards higher diffraction angles, reaching a maximum at 33 s after the start of the experiment (23 s after amine injection; Fig. 6.1b) before it finally moves towards lower diffraction angles. This shift goes along with a broadening of the peak. Gradual shifting of XRD reflections during intercalation processes is a frequently observed phenomenon and corresponds to a change in the mean interlayer

distance.[35,36] As the intercalation of species into the interlayer space does not occur homogenously, some interlayer distances are broadened by intercalation and some are not, until the intercalation process is finalized and all interlayer distances are broadened. This leads to a randomization of the interlayer distances and therefore to a modulation of the corresponding lattice plane distances, which is also known as interstratification. In our data analysis, we described the interstratification by using the Faulting Scenario I, which is given in Fig. 6.2.

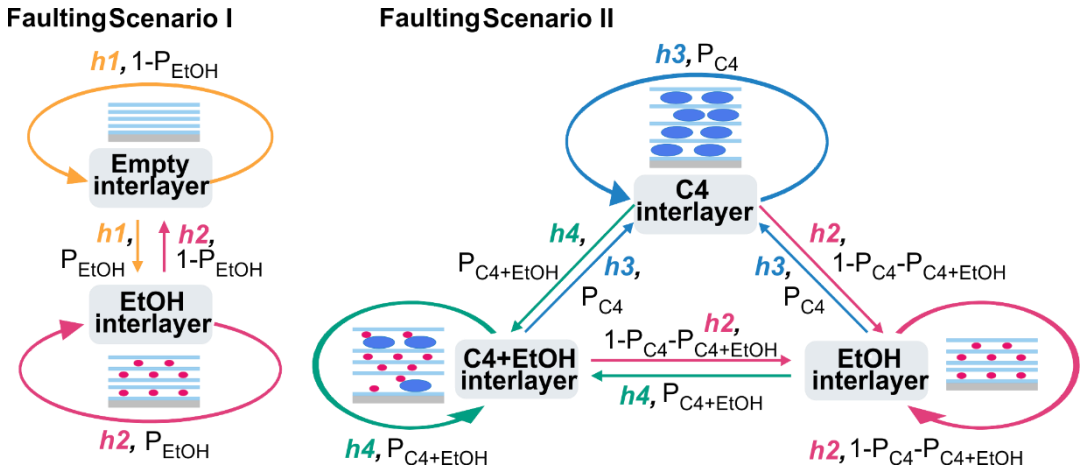

Fig. 6.2 Graphical representation of faulting scenarios describing the interstratification of ethanol between pristine $H_3Sb_3P_2O_{14}$ layers (Faulting Scenario I) and of amine, ethanol, and both amine and ethanol between the $H_3Sb_3P_2O_{14}$ layers (Faulting Scenario II), with h1, h2, h3, and h4 being the related interlayer distances (ESI Tab. S6.1) and the related fault probabilities P_{EtOH}, P_{C4}, $P_{C4+EtOH}$.

The corresponding *d*-spacing of the 00*l* reflection of the pristine thin film (d = 10.11 Å, Fig. 6.1b) does not match the interlayer distance of $H_3Sb_3P_2O_{14}$ bulk powder (d = 9.24 Å, ESI Fig. S6.2). Therefore, we conclude that there are empty layers as well as EtOH intercalated layers originating from the spin-coating process using EtOH as suspending liquid (see ESI experimental section). Regarding EtOH, stacking of non-intercalated layers, i.e. transitions (see transition probability matrix in ESI Tab. S6.1) among non-intercalated layers, are associated with an interlayer distance called h1, and transitions among EtOH-intercalated layers with an interlayer distance called h2, while h2 is larger than h1. A non-intercalated layer is followed by an intercalated layer with a certain fault probability, P_{EtOH} and by a non-intercalated layer with a probability of 1-P_{EtOH} since the rows in the transition probability matrix (ESI Tab. S6.1) have to sum up to 1. If $P_{EtOH} = 0$ the entire film does not show any EtOH intercalation and if $P_{EtOH} = 1$, all layers are intercalated with EtOH. In order to confirm that the considered faulting scenario leads to the changes in the peak profile and position that were experimentally

observed, we performed systematic, recursive DIFFaX-like[37] simulations of the XRD patterns using the TOPAS software.[38,39] These simulations serve as a qualitative measure and quantitative refinements of fault probabilities are usually performed after a certain faulting scenario is evaluated as suitable.[40-42]

Fig. 6.1d shows a series of recursive simulations in which P_{EtOH} was incrementally increased from 0 to 1 in steps of 0.05, thus simulating the gradual transition from non-intercalated to fully intercalated stacking. The 00*l* reflection gradually shifts towards lower diffraction angles from a position corresponding to an interlayer distance of h1 to the position corresponding to the large interlayer distance h2 (Fig. 6.1d, dashed lines). This goes along with a broadening of the reflection that reaches its maximum at $P_{EtOH} = 0.5$, where the stacking order is completely randomized for EtOH intercalated and non-intercalated stacking and therefore the structural coherence perpendicular to the layer planes reaches its minimum. After exposure of the sample to a He-gas flow, which is used to reduce air scattering and avoid sample degradation due to oxygen radicals, the ethanol is partially removed, resulting in a downshift in *d*-spacing of the stacking peak. When the atmosphere is enriched by ethanol from the reservoir after injection of the amine solution, the degree of the ethanol intercalation rises again, leading to a temporary upshift in *d*-spacing of the reflection. The peak broadening can partially be explained by the loss of structural coherence due to increasing ethanol interstratification, but also by the beginning of the amine intercalation, which decreases the effective lateral size of the $H_3Sb_3P_2O_{14}$ / $H_3Sb_3P_2O_{14} \cdot n(CH_3CH_2OH)$ domains.

In parallel, a broad peak attributed to the intercalation of the amine starts to appear in the low 2θ region 33 s after the start of the experiment (23 s after amine injection; Fig. 6.1a). During the intercalation process this peak becomes more intense, sharper, and shifts towards higher diffraction angles until it reaches a maximum corresponding to a *d*-spacing of 17.7 Å (Fig. 6.1a, red dashed line). The peak shows an asymmetrical broadening mostly towards lower diffraction angles. In the initial stage of the experiment, the broadening towards lower diffraction angles is very pronounced, leading to an almost trigonal peak shape. However, starting at around 75 s after the start of the experiment (65 s after amine injection), broadening towards higher diffraction angles becomes more dominant. Thus, the faulting scenario for the amine-intercalated phase is more complex than for the pristine sample. It contains stacking associated with amine intercalation with an interlayer distance h3, stacking associated with intercalation of amine and another component, e.g. ethanol, leading to a larger interlayer distance h4, and

finally a component associated with a smaller interlayer distance, h2, resulting from the intercalation of ethanol only. A graphical representation of this Faulting Scenario II is given in Fig. 6.2 and an overview on the transition probability matrix is shown in ESI Tab. S6.1. In a series of recursive XRD simulations, we gradually increased the probability for amine + ethanol intercalation ($P_{C4+EtOH}$) and for pure ethanol intercalation ($1-P_{C4}-P_{C4+EtOH}$) with the latter being increased by a factor of 1.5 compared to the increase in $P_{C4+EtOH}$. This leads to a peak tailing of the reflection towards lower diffraction angles (Fig. 6.1c, orange patterns) as well as to a small shift of the peak maximum towards higher diffraction angles, which is comparable with the trends observed in the later stages of the experiment (Fig. 6.1a, blue patterns). Therefore, in the later stages of the experiment some layers with pure ethanol intercalation may be present in the microstructure of the amine-intercalated layers, which represents incomplete amine intercalation since the peaks attributed to the non-amine intercalated phase disappear 205 s after the start of the experiment (195 s after amine injection; Fig. 6.1d). Additionally, some layers exhibit a larger distance caused, e.g., by the intercalation of both ethanol and amine simultaneously. The latter feature governs the microstructure in the initial stage of the experiment.

In order to extract more quantitative information from the measured XRD data, we refined the recorded patterns using a recursive supercell approach[38,39] and grid search routines[43,44] for the optimization of the transition probabilities. For minimization of the parameter space, we decided to use two separate phases: a phase describing the interstratification of ethanol in between the $H_3Sb_3P_2O_{14}$ layers, called "non-C4-intercalated phase", using Faulting Scenario I, and another phase called "C4-intercalated phase" for modeling the interstratification of ethanol, amine, and both ethanol and amine in-between the layers using Faulting Scenario II (Fig. 6.2, ESI Tab. S6.1).

Before starting the refinements, we had to derive the interlayer distances h1, h2, h3, and h4 (ESI Tab. S6.1). The interlayer distance of pristine, non-intercalated $H_3Sb_3P_2O_{14}$ could be directly extracted from the measured XRPD pattern (ESI Fig. S6.2). Note that this value was extracted from the bulk material as the processing for the fabrication of the thin films includes exfoliation/restacking as well as suspension of the material in a water/EtOH mixture. Therefore, the pristine thin film already contains EtOH in between the layers and cannot be used for the determination of h1. For the determination of the distance h2 for ethanol intercalated layers we used the XRD pattern collected after 1 s, as this could be modeled by

using one phase and Faulting Scenario I only. An automated, sequential series of 10,000 Rietveld refinements was performed for a 2-dimensional grid search in which the fault probability, P_{EtOH}, was varied between 0.01 and 1.00 and the interlayer distance h2 was altered between 10.70 Å and 11.69 Å. Fig. 6.3 shows a plot of the investigated parameter space against the R-wp values of the refinement.

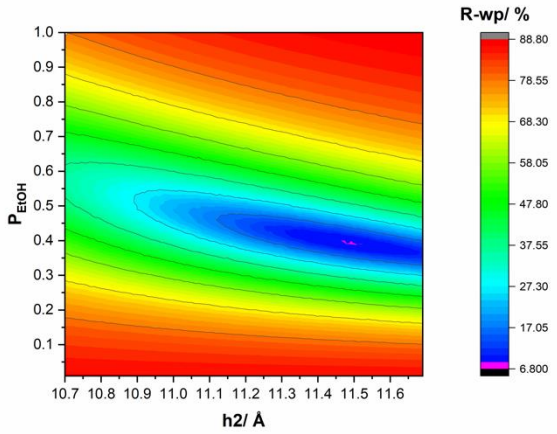

Fig. 6.3 Result of the two-dimensional grid search by an automated sequence of 10,000 Rietveld refinements for the optimization of the interlayer distance of ethanol intercalated thin film $H_3Sb_3P_2O_{14}$ (h2) and the ethanol intercalation probability P_{EtOH}.

The global minimum was determined as P_{EtOH} = 0.39 and h2 = 11.41 Å. The final refinement of the XRD pattern using these parameters led to a good fit (Fig. 6.4a) with satisfying agreement factors (R-wp = 6.9%). We refined the final diffraction pattern (Fig. 6.4c), recorded after 826 s, for the determination of h3 and h4, as it could be described by using the C4-intercalated phase and Faulting Scenario II only. Since the simultaneous grid search optimization of both h3, h4, P_{C4}, and $P_{C4+EtOH}$ bursts the parameter space, we went for an iterative approach: we used the peak position as an initial value for h3 and approximated h4 by adding the difference between h2 and h1 to h3 (Eq. 6.1). The transition probabilities were subsequently optimized by a 2D grid search using 10,000 Rietveld refinements. Afterwards we optimized h3 by a one-dimensional grid search and then used the refined parameter for another optimization of the transition probabilities. The iterations were repeated until all parameters showed a variation of less than 2%. It must be noted, that the optimization of h4 was impossible due to a strong correlation with $P_{C4+EtOH}$ and therefore we kept the relationship:

$$h4 = h3 + (h2 - h1) \qquad \text{(Eq. 6.1)}$$

as an educated guess. Using the optimized values for h3, h4, P_{C4}, and $P_{C4+EtOH}$ led to a proper refinement of the XRD pattern recorded 826 s after the start of the experiment (816 s after

amine injection; Fig. 6.4c). With all interlayer distances known, we were able to refine the recorded XRD patterns using the two-phase approach. As an example, the graphical result of the final refinement (using all interlayer distances as well as all optimized transition probabilities) of the XRD pattern recorded 75 s after the start of the experiment (65 s after amine injection) is given in Fig. 6.4b.

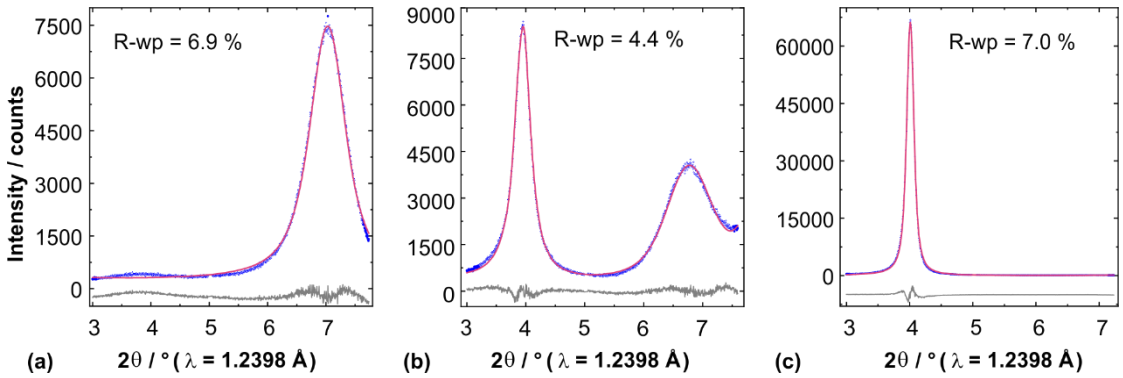

Fig. 6.4 Graphical results of the final Rietveld refinements (pink) of the XRD patterns (blue) recorded (a) 1 s, (b) 75 s and (c) 826 s after the start of the experiment using a non-C4-intercalated phase with random ethanol interstratification described by Faulting Scenario I (Fig. 6.2, ESI Tab. S6.1) and a C4-intercalated phase with random amine, ethanol, and both ethanol and amine interstratification using Faulting Scenario II. The grey graphs show the difference plots. For phase fractions and fault probabilities, refer to Tab. S6.2 in the ESI.

The refinement of the recorded XRD patterns enabled us to monitor the evolution of the phase fractions (Fig. 6.5) and the fault probabilities (ESI Fig. S6.3) during the amine intercalation process.

6.5.2 Proposed Intercalation Mechanism

In order to derive conclusions on the intercalation mechanism we calculated the relative amounts of $H_3Sb_3P_2O_{14}$-layers showing either no-, pure ethanol-, ethanol + amine-, or pure amine intercalation from the refined phase fractions and fault probabilities using (Eq. 6.2 – Eq. 6.5):

$$[\text{no-intercalation}]_{\text{total}} = [\text{non-C4-intercalated phase}] \cdot (1 - P_{\text{EtOH}}) \quad \text{(Eq. 6.2)}$$

$$[\text{EtOH-intercalation}]_{\text{total}} = [\text{non-C4-intercalated phase}] \cdot P_{\text{EtOH}} + [\text{C4-intercalated phase}] \cdot (1 - P_{\text{C4}} - P_{\text{C4+EtOH}}) \quad \text{(Eq. 6.3)}$$

$$[\text{EtOH+C4-intercalation}]_{\text{total}} = [\text{C4-intercalated phase}] \cdot P_{\text{C4+EtOH}} \quad \text{(Eq. 6.4)}$$

$$[\text{C4-intercalation}]_{\text{total}} = [\text{C4-intercalated phase}] \cdot P_{\text{C4}} \quad \text{(Eq. 6.5)}$$

It should be noted that the applied model is an approximation of the microstructure of the intercalated thin film. The distance of ethanol and amine double intercalated layers (h4) could not be experimentally determined, as this distance is also correlated with the corresponding fault probability ($P_{C4+EtOH}$). Hence the relative trends in the evolution of the phase fractions should be interpreted, rather than the absolute values. In addition, we cannot exclude double intercalation of ethanol or further modulation of the interlayer distances by flexible ratios of intercalated ethanol : amine. However, more complex faulting models would lead to a further overextension of the parameter space and therefore to less reliable results.

At the start of the reaction, 39% of the layers show ethanol intercalation, most likely from spin-coating and 61% of the layers do not exhibit any intercalation. In the initial stage of the reaction, the ethanol content decreases first slowly, and 20 s after the start of the experiment (10 s after amine injection) rapidly (Fig. 6.5a, pink). This is most likely attributed to the dynamic He-atmosphere in the measurement chamber. As the atmosphere is initially ethanol-free during the mounting and alignment of the sample, it leads to ethanol evaporation (ESI Tab. S6.3; reaction [I]) from the thin film, causing a de-intercalation of ethanol (ESI Tab. S6.3; reaction [III]). As the atmosphere saturates with ethanol after the injection of the ethanolic amine solution, the solvent is slowly re-intercalated in-between the layers (ESI Tab. S6.3; reaction [IV]) starting at 33 s after the start of the experiment (23 s after amine injection), most likely because the partial pressure of ethanol exceeds the equilibrium pressure for intercalation.

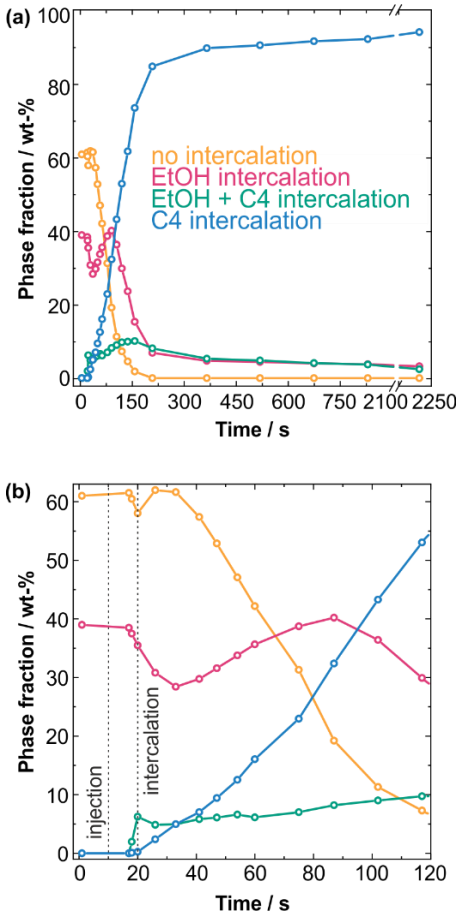

Fig. 6.5 Evolution of the relative amounts of $H_3Sb_3P_2O_{14}$-layers showing no- (orange), ethanol- (pink), ethanol + amine- (green) and amine-intercalation (blue) over the entire monitoring time (a) and during the initial stage of the reaction (b). The dashed lines show the gap between the injection of the amine and the intercalation of the amine.

For confirmation, we exposed a spin-coated $H_3Sb_3P_2O_{14}$-thin film to a He-gas flow in order to remove the intercalated ethanol and indeed the reflection shifted to higher diffraction angles (ESI Fig. S6.4). Afterwards the film was put into a chamber with a saturated ethanol atmosphere, and after 15 min the reflection shifted to lower diffraction angles towards the original position.

In addition to ethanol, amine also evaporates from the reservoir (ESI Tab. S6.3; reaction [II]). 18 s after the start of the experiment (8 s after amine injection), the beginning of amine intercalation in between the $H_3Sb_3P_2O_{14}$-layers can be observed. Interestingly, the amine uptake initially occurs by intercalation of both amine and ethanol (Fig. 6.5a, green). An exclusive intercalation of amine can be observed to a significant extent 26 s after the start of the experiment (16 s after amine injection; Fig. 6.5a, blue). Therefore, it can be concluded that the amine preferably enters the ethanol intercalated layers, as the interlayer distance is already

broadened and the interlayer space is therefore more accessible for the molecule. Intercalation of both ethanol and amine, however, leads to a huge separation of the $H_3Sb_3P_2O_{14}$-layers of at least 20 Å (ESI Tab. S6.1), which is apparently not stable. This is only an intermediate state and ethanol subsequently leaves the thin film. The amount of pure ethanol intercalated layers increases until 87 s after the start of the experiment (77 s after amine injection). At this point of the reaction, the amount of non-intercalated layers (Fig. 6.5a, orange) has already decreased that much that the re-intercalation of ethanol cannot compensate the consumption of purely ethanol intercalated layers by the amine uptake. The number of layers showing intercalation of both ethanol and amine increases until 154 s after the start of the experiment (144 s after amine injection; Fig. 6.5b, green), which means that the amine uptake into pure ethanol intercalated layers (ESI Tab. S6.3; reaction [V]) outweighs the extrusion of ethanol (ESI Tab. S6.3; reaction [III]). Finally, the number of layers showing intercalation of both molecules decreases due to a lack of ethanol intercalated layers serving as an acceptor for amine. 205 s after the start of the experiment (195 s after amine injection) all layers exhibit intercalation of either ethanol, amine, or both ethanol and amine (Fig. 6.5b). The increase of the amount of pure amine intercalated layers begins to flatten 205 s after the start of the experiment (195 s after amine injection; Fig. 6.5b, blue), as the system approaches a stationary state. At the end of the experiment, the amount of amine-intercalated layers only slowly increases by 0.6% during the last 155 s of the experiment. Finally, there are still significant amounts (3.7-3.8%) of pure ethanol or both ethanol and amine intercalated layers apparent, i.e. <96% amine intercalated layers, indicating that the system approaches an equilibrium state. However, since we are studying the intercalation in an open system due to the He-flow, we cannot observe the actual equilibrium state. The last data point, which was measured at the end of the monitoring time (2240 s after amine injection) was also refined for comparison and shows that only minor changes occur after the end of the experiment (816 s after amine injection) and EtOH is still present in the thin film to a small extent.

In consequence, we can draw the following conclusions on the amine intercalation process into the $H_3Sb_3P_2O_{14}$ interlayer space in the presence of ethanol. In the first reaction step, the dynamic atmosphere (He-gas flow) is saturated with the reactants (ESI Tab. S6.3, step 1; Fig. 6.6a-c), which can lead to a temporary decrease in the amount of intercalated ethanol. Afterwards both ethanol and amine are intercalated into $H_3Sb_3P_2O_{14}$. While ethanol also enters non-intercalated layers (ESI Tab. S6.3, step 2a; Fig. 6.6c), the larger amine molecule accesses layers that already have been pre-opened through ethanol intercalation (ESI Tab. S6.3, step

2b; Fig. 6.6d-e). This first leads to a double intercalation of ethanol and amine (Fig. 6.6e) and therefore to a comparatively large interlayer distance (ca. 20 Å). Such a large separation of the layers or the co-arrangement of EtOH and amine seems to be unstable and this finally leads to the extrusion of ethanol (ESI Tab. S6.3, step 3; Fig. 6.6e-f), as the amine shows a stronger bonding to the layers and likely a more efficient packing without EtOH.

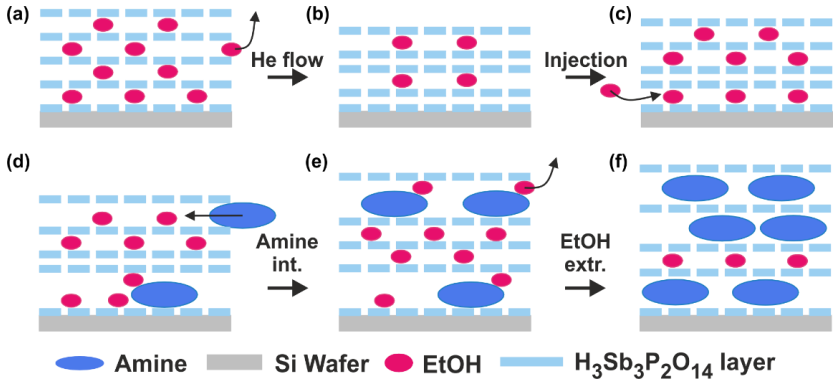

Fig. 6.6 Schematic description of the different stages during the amine intercalation experiment. (a) Pristine sample with EtOH intercalation from spin-coating. (b) Ethanol is partially removed in He-flow. (c) Re-intercalation of EtOH after injection of amine/EtOH solution. (d) Amines enter pre-widened ethanol containing layers. (e) Ethanol is extruded by amine intercalation. (f) Final amine-intercalated sample in equilibrium with minor ethanol remains.

Hence, the intercalation of ethanol and amine can be seen as competing processes. The amine is not capable of completely extruding ethanol, as ethanol intercalated layers are still apparent when the reaction reaches a stationary state, which means that ethanol also extrudes amine to a small degree. Therefore, there seems to be a chemical equilibrium between the ethanol and amine intercalation, which lies more on the latter side. However, due to the continuous He-flow leading to a constant extrusion of ethanol and to lesser extent of amine, the equilibrium state is never reached.

6.6 Conclusions

In summary, we presented a novel method for the analysis of peakshifts induced by intercalation in layered thin films determined by real-time XRD measurements, which is based on a quantitative refinement of the Bragg peak position and profile in the XRD pattern by a recursive approach. We exemplarily applied the method to analyze the (co-)intercalation mechanism of ethanolic butylamine solution into $H_3Sb_3P_2O_{14}$ thin films *via* the vapor phase in real-time. By extracting the interlayer distances as well as the fault probabilities based on two different faulting scenarios for non-amine- and amine-intercalated samples, Rietveld refinements could be performed for the real-time monitoring at different stages of the amine

intercalation experiment. Using this approach, details of the intercalation process such as the kinetics of amine uptake and the formation of intermediates could be extracted and the following stages of the intercalation process were identified: (1) Ethanol saturation of the gas phase; (2) Intercalation of ethanol; (3) Intercalation of C4 in EtOH intercalated layers; (4) Extrusion of intercalated EtOH. According to our results, the intercalation of EtOH and amine are competing processes with the chemical equilibrium lying strongly on the amine side.

Since the intercalation of guest species in layered materials has been intensely studied,[19,21,26,28,29,45] we believe that the analysis procedure developed in this work provides a new toolbox for generating mechanistic insights into the intercalation process, which will be instrumental for fine-tuning the properties of 2D layered materials.

6.7 Conflict of Interest

The authors declare no competing financial interest.

6.8 Acknowledgements

Financial support was granted by the Max Planck Society, the University of Munich (LMU), the Center for Nanoscience and the Cluster of Excellence e-conversion. The authors thank K. Pflaum and F. Adams for design and drawings of the measurement chamber and H. Nakamura and A. Mohammed for assistance regarding the Kapton dome fabrication procedure. A. Jiménez-Solano gratefully acknowledges a postdoctoral scholarship from the Max Planck Society. We acknowledge the KIT light source for provision of beamtime at the beamline MPI and we would like to thank the institute for Beam Physics and Technology (IBPT) for the operation of the storage ring, the Karlsruhe Research Accelerator (KARA).

6.9 References

1. A. K. Geim, K. S. Novoselov, *Nat. Mater.* **2007**, *6*, 183.
2. J. A. Wilson, A. D. Yoffe, *Adv. Phys.* **1969**, *18*, 193.
3. R. Ma, T. Sasaki, *Adv. Mater.* **2010**, *22*, 5082.
4. M. Q. Arguilla, J. Katoch, K. Krymowski, N. D. Cultrara, J. Xu, X. Xi, A. Hanks, S. Jiang, R. D. Ross, R. J. Koch, S. Ulstrup, A. Bostwick, C. Jozwiak, D. W. McComb, E. Rotenberg, J. Shan, W. Windl, R. K. Kawakami, J. E. Goldberger, *ACS Nano* **2016**, *10*, 9500.
5. M. Naguib, V. N. Mochalin, M. W. Barsoum, Y. Gogotsi, *Adv. Mater.* **2013**, *26*, 992.

6. K. Kalantar-zadeh, J. Z. Ou, T. Daeneke, A. Mitchell, T. Sasaki, M. S. Fuhrer, *Appl. Mater. Today* **2016**, *5*, 73.

7. J. N. Coleman, M. Lotya, A. O'Neill, S. D. Bergin, P. J. King, U. Khan, K. Young, A. Gaucher, S. De, R. J. Smith, I. V. Shvets, S. K. Arora, G. Stanton, H.-Y. Kim, K. Lee, G. T. Kim, G. S. Duesberg, T. Hallam, J. J. Boland, J. J. Wang, J. F. Donegan, J. C. Grunlan, G. Moriarty, A. Shmeliov, R. J. Nicholls, J. M. Perkins, E. M. Grieveson, K. Theuwissen, D. W. McComb, P. D. Nellist, V. Nicolosi, *Science* **2011**, *331*, 568.

8. V. Nicolosi, M. Chhowalla, M. G. Kanatzidis, M. S. Strano, J. N. Coleman, *Science* **2013**, *340*, 1226419.

9. Y. Ebina, T. Sasaki, M. Watanabe, *Solid State Ion.* **2002**, *151*, 177.

10. T. Sasaki, *J. Ceram. Soc. Japan* **2007**, *115*, 9.

11. L. M. Liz-Marzán, M. Giersig, *Low-Dimensional Systems: Theory, Preparation, and Some Applications*, Springer, Berlin, Germany, **2003**.

12. Z. Hennighausen, S. Kar, *Electron. Struct.* **2021**, *3*, 014004.

13. M. Rajapakse, B. Karki, U. O. Abu, S. Pishgar, M. R. K. Musa, S. M. S. Riyadh, M. Yu, G. Sumanasekera, J. B. Jasinski, *npj 2D Mater. Appl.* **2021**, *5*, 30.

14. M. A. Lukowski, A. S. Daniel, F. Meng, A. Forticaux, L. Li, S. Jin, *J. Am. Chem. Soc.* **2013**, *135*, 10274.

15. S.-L. Zhang, H.-H. Choi, H.-Y. Yue, W.-C. Yang, *Curr. Appl. Phys.* **2014**, *14*, 264.

16. J. Qin, G. Qiu, J. Jian, H. Zhou, L. Yang, A. Charnas, D. Y. Zemlyanov, C.-Y. Xu, X. Xu, W. Wu, H. Wang, P. D. Ye, *ACS Nano* **2017**, *11*, 10222.

17. C. Wang, Q. He, U. Halim, Y. Liu, E. Zhu, Z. Lin, H. Xiao, X. Duan, Z. Feng, R. Cheng, N. O. Weiss, G. Ye, Y.-C. Huang, H. Wu, H.-C. Cheng, I. Shakir, L. Liao, X. Chen, W. A. Goddard Iii, Y. Huang, X. Duan, *Nature* **2018**, *555*, 231.

18. F. R. Gamble, J. H. Osiecki, M. Cais, R. Pisharody, F. J. DiSalvo, T. H. Geballe, *Science* **1971**, *174*, 493.

19. G. Lagaly, *Solid State Ion.* **1986**, *22*, 43.

20. R. M. Tindwa, D. K. Ellis, G.-Z. Peng, A. Clearfield, *J. Chem. Soc., Faraday Trans. 1* **1985**, *81*, 545.

21. F. Menéndez, A. Espina, C. Trobajo, J. Rodríguez, *Mater. Res. Bull.* **1990**, *25*, 1531.

22. J. García-Glez, C. Trobajo, S. A. Khainakov, Z. Amghouz, *Arab. J. Chem.***2017**, *10*, 885.

23. S. Deniard-Courant, Y. Piffard, P. Barboux, J. Livage, *Solid State Ion.* **1988**, *27*, 189.

24. J. G. Decaillon, Y. Andres, J. C. Abbe, M. Tournoux, *Solid State Ion.* **1998**, *112*, 143.

25. C. S. Griffith, V. Luca, J. Cochrane, J. V. Hanna, *Microporous Mesoporous Mater.* **2008**, *111*, 387.

26. P. Ganter, L. M. Schoop, M. Däntl, B. V. Lotsch, *Chem. Mater.* **2018**, *30*, 2557.

27. K. Szendrei-Temesi, A. Jiménez-Solano, B. V. Lotsch, *Adv. Mater.* **2018**, *30*, 6289.

28. P. Ganter, L. M. Schoop, B. V. Lotsch, *Adv. Mater.* **2017**, *29*, 1604884.

29. M. Däntl, P. Ganter, K. Szendrei-Temesi, A. Jiménez-Solano, B. V. Lotsch, *Nanoscale Horiz.* **2020**, *5*, 74.

30. Q. Zhang, L. Mei, X. Cao, Y. Tang, Z. Zeng, *J. Mater. Chem. A* **2020**, *8*, 15417.

31. J. S. O. Evans, S. J. Price, H.-V. Wong, D. O'Hare, *J. Am. Chem. Soc.* **1998**, *120*, 10837.

32. S. Schorr, C. Weidenthaler, *Crystallography in Materials Science: From Structure-Property Relationships to Engineering*, De Gruyter, Berlin, Germany, **2021**.

33. S. Jeong, D. Yoo, M. Ahn, P. Miró, T. Heine, J. Cheon, *Nat. Commun.* **2015**, *6*, 5763.

34. M. Ghidiu, J. Halim, S. Kota, D. Bish, Y. Gogotsi, M. W. Barsoum, *Chem. Mater.* **2016**, *28*, 3507.

35. S. Célérier, S. Hurand, C. Garnero, S. Morisset, M. Benchakar, A. Habrioux, P. Chartier, V. Mauchamp, N. Findling, B. Lanson, E. Ferrage, *Chem. Mater.* **2019**, *31*, 454.

36. H. He, C. Huang, C.-W. Luo, J.-J. Liu, Z.-S. Chao, *Electrochim. Acta* **2013**, *92*, 148.

37. M. M. J. Treacy, J. M. Newsam, M. W. Deem, *Proc. Math. Phys. Eng. Sci.* **1991**, *433*, 499.

38. C. M. Ainsworth, J. W. Lewis, C.-H. Wang, A. A. Coelho, H. E. Johnston, H. E. A. Brand, J. S. O. Evans, *Chem. Mater.* **2016**, *28*, 3184.

39. A. A. Coelho, J. S. O. Evans, J. W. Lewis, *J. Appl. Crystallogr.* **2016**, *49*, 1740.

40. S. Bette, R. E. Dinnebier, D. Freyer, *J. Appl. Crystallogr.* **2015**, *48*, 1706.

41. S. Bette, T. Takayama, K. Kitagawa, R. Takano, H. Takagi, R. E. Dinnebier, *Dalton Trans.* **2017**, *46*, 15216.

42. L. Diehl, S. Bette, F. Pielnhofer, S. Betzler, I. Moudrakovski, G. A. Ozin, R. Dinnebier, B. V. Lotsch, *Chem. Mater.* **2018**, *30*, 8932.

43. S. Bette, T. Takayama, V. Duppel, A. Poulain, H. Takagi, R. Dinnebier, Ernst, *Dalton Trans.* **2019**, *48*, 9250.

44. S. Bette, B. Hinrichsen, D. Pfister, R. E. Dinnebier, *J. Appl. Crystallogr.* **2020**, *53*, 76.

45. M. Däntl, S. Guderley, K. Szendrei-Temesi, D. Chatzitheodoridou, P. Ganter, A. Jiménez-Solano, B. V. Lotsch, *Small* **2021**, *17*, 2007864.

7 Conclusions and Outlook

7.1 Conclusions

As the application of nanosheets as active sensing component has great potential for sensor miniaturization, this thesis aimed to increase the adaptability and versatility of photonic sensing devices to enable commercially successful applications in the near future. To address the obstacles that currently prevent real-world applications, the main goal was to develop advanced techniques for customizing the properties of nanosheet-based optical sensors, which include the shapes of the sensor and substrate, and the tuning of the sensor selectivity. For this purpose, sensors using $H_3Sb_3P_2O_{14}$ nanosheets as stimuli-responsive material were studied, because this material is well known for its applications as colorimetric vapor sensors (both thin films and 1DPCs).[1-4]

In Chapter 4 the enhancement of the versatility of $H_3Sb_3P_2O_{14}$ thin film sensors was addressed by applying a soft vapor-phase post-synthetic amine modification allowing for the facile, continuous and reversible tailoring of the properties. Specifically, it was found that when an amine-intercalated thin film is exposed to the vapor of another primary alkylamine, the second one continuously replaces the first one, until only the second one is present in the sample at the end of the process. The broad applicability of this two-step intercalation and exchange approach was demonstrated by intercalating and replacing a large variety of alklyamines ranging from ethylamine to dodecylamine. This method emphasizes the exquisite control over the thin film properties on demand, as the sub-Å continuous change in the mean *d*-spacing and polarity of the thin films could be controlled in a reversible manner. Hereby the facile, continuous and reversible tailoring of the properties of the photonic sensor, and the experimental ease are clear advantages over non-reversible covalent modification, or sophisticated electrochemical intercalation, which mostly requires inert gas conditions as well as an external power supply. Moreover, it was demonstrated that the discussed strategy could be applied in combination with masks of different sizes to pattern the thin films with a high level of spatial control by making use of the reversibility of the amine exchange process.

Due to the fact that 1DPC sensors comprised of $H_3Sb_3P_2O_{14}$ nanosheets and TiO_2 nanoparticles exhibit a much larger thickness and therefore stability when removed from the substrate, this multilayer system was chosen for the studies conducted with the aim of transferring the sensor to arbitrary substrates. Since in preceding research the amine intercalation has also been applied to this type of sensor, it was assumed that the amine

exchange and the patterning technique mentioned in Chapter 4 can be adapted for the 1DPC system. In Chapter 5, a facile (pattern) transfer method for hydrophobized 1DPCs based on the use of a water soluble sacrificial layer (LTS) was presented. The hydrophobization of the 1DPC, which prevents the sensor from damage during the transfer, was achieved through the intercalation of *n*-octylamine either for the whole sample or in a spatially resolved manner by using a mask. Therefore, the 1DPC or patterns thereof could be detached from their original substrate in a quick and facile way by immersion of the samples in DI water, whereby only the sacrificial layer was dissolved. This enabled the transfer to arbitrary substrates, including curved surfaces, on which the direct deposition of the 1DPC is impossible. Furthermore, the hydrophobicity and hence the sensing response of the transferred sample could be tailored flexibly and reversibly with the amine exchange approach demonstrated for antimony phosphate thin films (Chapter 4). Compared to peel-off after polymer infiltration (which often impairs the optical quality and stimuli-responsiveness), contact printing or wet etching of a sacrificial layer (which are both multistep processes), this method stands out for its experimental ease as well as the flexibility with respect to the shape and the properties of the transferred 1DPC and the shape of the substrate.

The work conducted in Chapter 4 and 5 contributed to the customization of $H_3Sb_3P_2O_{14}$-based sensors by applying amine intercalation. However, the intercalation process has not been understood on a fundamental level yet, especially when the intercalation is solvent-mediated and competing intercalation between the solvent and the intercalant may occur. Therefore, this issue was addressed in Chapter 6 by applying a novel approach for the quantitative analysis of changes in the peak profile and position observed in *in situ* XRD diffraction patterns induced by the intercalation of a guest species into a layered host. Specifically, the viability of this approach was demonstrated by using a dataset collected during the real time monitoring of the intercalation of *n*-butylamine (3M in ethanol) into an $H_3Sb_3P_2O_{14}$ thin film over the vapor phase. The peak broadening and shifting that occurs during the intercalation of the solvent, amine, and solvent-amine double intercalation was analyzed with a state-of-the-art recursive supercell approach. Based on these results, it was possible to perform quantitative Rietveld refinements for the XRD patterns that were meausured during the intercalation. Hereby the following stages were identified: (1) Ethanol saturation of the gas phase; (2) Re-intercalation of ethanol after amine injection; (3) Intercalation of *n*-butylamine in ethanol-intercalated layers; (4) Extrusion of intercalated ethanol. Based on the results above, it seems that the intercalation of ethanol and amine are competing processes, whereby the chemical equilibrium lies on the

amine side. This is most likely due to the fact that the basicity of the amine is much higher than the basicity of ethanol. Therefore, it is more likely that the amine is protonated by the H^+ located in the interlayer gallery and is thus trapped in the structure. Compared to other methods, this analysis protocol allowed monitoring the intercalation process in the thin film at greater depth than it has been done before. Overall, the insights gained in this project may contribute to the understanding of peak shifts observed during intercalation in layered host materials in general.

In conclusion, this thesis revealed different utilization possibilities of amine intercalation in $H_3Sb_3P_2O_{14}$-based photonic devices in order to enhance their versatility for future practical applications, especially in the field of miniaturized vapor sensors. The method of facile amine exchange enabled a tailored control over the properties of the photonic sensors, which is a powerful tool for improving multiple aspects that currently prevent the commercial application of nanosheet-based sensing devices. This allows an adaptable tuning of the selectivity of the sensor post-synthetically, along with the possibility of patterning and transfer. Additionally, the mechanism of the amine intercalation in the thin film sensors was understood on a fundamental level by applying a novel analysis approach. Generally, this lays the foundation for establishing a new method for the analysis of peak shifts in X-ray diffraction patterns.

7.2 Outlook

The results and advancements in the field of tailoring the properties of nanosheet-based photonic sensors presented in this thesis provide a sound and solid foundation for future investigations. Such investigations could further contribute to bridging the gap towards commercial applications and lead to a deeper fundamental understanding of the properties and processes of amine intercalated nanosheet-based devices. Thus, the results presented in this thesis can serve as a gate opener for stimulating future in-depth research on nanosheet-based sensors. In the following, some directions for future research are proposed.

One main point that would benefit from attention is the application of the analysis approach from Chapter 6 for *in situ* monitoring of the amine-amine exchange intercalation process. This would enable the elucidation of the mechanism of the amine exchange reported in Chapter 4 and the determination whether the properties of the amine (hydrophobic vs. hydrophilic or bulkiness of the molecule) have an influence on the intercalation mechanism.

Another aspect regarding the fundamental understanding of amine intercalation and exchange, that might be worthwhile to investigate, is the kinetics. To this end, time-of-flight secondary ion mass spectrometry (ToF-SIMS) measurements could provide helpful insights by characterizing the lateral diffusion behavior that occurs during the patterning of $H_3Sb_3P_2O_{14}$ thin films, which was applied in Chapter 4. Preliminary ToF-SIMS measurements showed that it is possible to detect the different quantities of amine present along a linescan taking into account the intercalated and the non-intercalated area of the sample. However, we noticed that inhomogenities of the sample tend to blur the results. Therefore, switching from spin-coating to dip-coating and optimizing the time the sample is exposed to the amine vapor will be necessary for future studies. Information gained on the amine-exchanged samples with ToF-SIMS measurements would help complementing and understanding the *in situ* XRD analysis discussed above.

Also in light of a fundamental understanding of the nanosheets studied in this thesis, it would be interesting to investigate the impact of the morphology (e.g. layered bulk material, nanosheet pellet and nanosheet-based thin film) on the sensing behavior. For example, this could be done by comparing real time XRD measurements at different relative humidities for each morphology as the disorder in the material as well as the grain size should have an impact on the intercalation capability during the sensing event.

Moreover, the routine presented in Chapter 6 can be applied to real time XRD measurements in different atmospheres, which potentially enables tracking the humidity in human breath in real time. As the antimony phosphate nanosheets exhibit rapid swelling properties, this material is a suitable candidate for such experiments.

If future experiments demonstrated an altered response of the sensor when exposed to analytes in "sick" breath, this would open up the possibility of applying this material in medical diagnostics or point-of-care sensors with the advantage of a quick and facile optical readout. So far, some examples in literature have demonstrated that acetone appears in the breath of patients with type 1 diabetes[5] and that lung diseases, such as asthma[6] and COVID-19,[7] can be diagnosed by measuring the amount of nitric oxide and ammonia in the patients' breath. Especially the latter application might be an interesting starting point to test the use of nanosheet-based photonic sensors for the detection of diseases. Responsiveness towards these analytes may be achieved by chemical modification of the nanosheets with functional groups that allow the selective adsorption of the desired gases or volatiles.

Taking into account the fact that the nanosheet-based photonic sensors discussed in this thesis can detect and differentiate amines, future research could be directed towards the detection of biologically relevant amines in order to increase their possible applications. First steps in this direction have already been discussed in Chapter 4, as it was demonstrated that trimethylamine and 1,5-diaminopentane (cadaverine), which are both produced through microbial spoilage of fish and meat, can be detected reliably. Other biogenic amines that could be studied and are relevant for the monitoring of food freshness include histamine, 2-phenylethylamine, putrescine, and tryptamine, among others.[8,9] Furthermore, the detection of *o*-toluidine and aniline,[10] as well as isobutylamine[11] would be relevant for medical diagnostics, and the detection of amphetamine[12] or methylhexanamine[13] could help to verify the abuse of performance enhancing drugs. Therefore, it should be tested if the nanosheet-based sensors discussed in this thesis exhibit responsiveness towards any of the analytes above and possibly can even undergo an amine exchange, which would render them a class of sensors with high adaptability.

Lastly and on a more general note, it is likely that the insights into amine intercalation in $H_3Sb_3P_2O_{14}$–based sensors gained in this thesis are generic and can be applied to other nanosheet-based systems, while being compatible with various types of applications. Since huge efforts are directed towards nanosheet-research it is likely that nanosheet-based technologies will be commercially available in a few years' time.

7.3 References

1. P. Ganter, L. M. Schoop, M. Däntl, B. V. Lotsch, *Chem. Mater.* **2018**, *30*, 2557.
2. P. Ganter, K. Szendrei, B. V. Lotsch, *Adv. Mater.* **2016**, *28*, 7436.
3. K. Szendrei, P. Ganter, O. Sànchez-Sobrado, R. Eger, A. Kuhn, B. V. Lotsch, *Adv. Mater.* **2015**, *27*, 6341.
4. K. Szendrei, A. Jiménez-Solano, G. Lozano, B. V. Lotsch, H. Míguez, *Adv. Opt. Mater.* **2017**, *5*, 1700663.
5. V. Ruzsányi, M. Péter Kalapos, *J. Breath Res.* **2017**, *11*, 024002.
6. J. A. Miskoff, A. Dewan, M. Chaudhri, *Cureus* **2019**, *11*, e4864.
7. M. C. Exline, M. Stanacevic, A. S. Bowman, P.-I. Gouma, *PLoS ONE* **2021**, *16*, e0257644.
8. A. Naila, S. Flint, G. Fletcher, P. Bremer, G. Meerdink, *J. Food Sci.* **2010**, *75*, R139.
9. J. Brockgreitens, A. Abbas, *Compr. Rev. Food Sci. Food Saf.* **2016**, *15*, 3.

10. G. Preti, J. N. Labows, J. G. Kostelc, S. Aldinger, R. Daniele, *J. Chromatogr. B* **1988**, *432*, 1.

11. H. Wolrath, U. Forsum, P. G. Larsson, H. Borén, *J. Clin. Microbiol.* **2001**, *39*, 4026.

12. Y. Jang, M. Jang, H. Kim, S. J. Lee, E. Jin, J. Y. Koo, I.-C. Hwang, Y. Kim, Y. H. Ko, I. Hwang, J. H. Oh, K. Kim *Chem* **2017**, *3*, 641.

13. Y. Zhang, R. M. Woods, Z. S. Breitbach, D. W. Armstrong, *Drug Test. Anal.* **2012**, *4*, 986.

8 Appendix

This Chapter gives a list of abbreviations, the supplementary information for Chapters 4 - 6 as well as a list of publications and scientific contributions.

8.1 Abbreviations

Abbreviation	
1D	One-dimensional
1DPC	One-Dimensional photonic crystal
2D	Two-dimensional
3D	Three-dimensional
Å	Angström
BS	Bragg stack
DBR	Distributed Bragg reflector
DI	De-ionized
DLS	Dynamic light scattering
EISA	Evaporation induced self-assembly
EtOH	Ethanol
FET	Field effect transistor
IoT	Internet of Things
LBL	Layer-by-layer
LCST	Lower critical solution temperature
LDH	Layered double hydroxide
LTS	Lithium tin sulfide
MOF	Metal-organic framework
MOS	Metal oxide semiconductor
NP	Nanoparticle
PBG	Photonic band gap
PC	Photonic crystal
PCA	Principal component analysis

PCGO	Physically confined graphene oxide
PDMS	Polydimethylsiloxane
PVDF	Polyvinylidene fluoride
RGO	Reduced graphene oxide
RH	Relative humidity
RI	Refractive index
rpm	Rounds per minute
SEM	Scanning electron microscopy
TBAOH	Tetra(*n*-butyl)ammonium hydroxide
TMAOH	Tetramethylammonium hydroxide
TMD	Transition metal dichalchogenide
TMM	Transfer matrix method
TMO	Transition metal oxide
TTIP	Titanium tetraisopropoxide
UV	Ultraviolet
VOC	Volatile organic compound
vol-%	Volume fraction
wt-%	Weight fraction
XRD	X-ray diffraction
XRPD	X-ray powder diffraction

8.2 Supporting Information for Chapter 4

Customizing $H_3Sb_3P_2O_{14}$ Nanosheet Sensors by Reversible Vapor-phase Amine Intercalation

*Marie Däntl, Pirmin Ganter, Katalin Szendrei-Temesi, Alberto Jiménez-Solano, Bettina V. Lotsch**

Experimental Section

Nanosheet Synthesis and Spin-coating

$K_3Sb_3P_2O_{14}$ was synthesized from KNO_3 (Merck, for analysis), $NH_4H_2PO_4$ (Acros Organics, >98%) and Sb_2O_3 (Alfa Aesar, 99.6%) as described elsewhere.[1-3]

As reported previously, $K_3Sb_3P_2O_{14}$ was protonated, exfoliated and dried.[1-3] Subsequently, the powder was dissolved in a water-ethanol mixture, ultrasonicated and spin-coated (WS-650MZ-23NPP, Laurell Technology Corporation) as thin films on Si-wafers (1.5 x 1.5 cm, 110 orientation).[1-3] Each wafer was spin-coated twice with 200 μL of the colloidal suspension for 1.5 min (Speed: 2000 rpm, acceleration: 10000 rpm). Prior to thin film deposition the Si-wafers were cleaned with oxygen plasma for 10 min.

Amine Intercalation

The $H_3Sb_3P_2O_{14}$ nanosheet-based thin films with a thickness of about 160 nm were intercalated with primary amines with an even number of C-atoms ($2 \leq n \leq 12$), over the vapor phase as reported elsewhere.[3] All amines were used as purchased without further dilution or as 3M dilutions in ethanol (ethylamine, Acros Organics, 70% in water; 1-butylamine, Alfa Aesar, 99%; hexylamine, Acros Organics, 99%; *n*-octylamine, Acros Organics, >99%; *n*-decylamine, Acros Organics, 99%, nitrogen flushed; dodecylamine, Aldrich, 98%). All experiments with $n \leq 8$ were performed at room temperature, whereas experiments with $n \geq 10$ were conducted at 80 °C, to evaporate the amine and enhance the intercalation speed. The intercalation process was considered as complete once the films showed a non-changing and uniform color. Subsequently the single step (step one) amine intercalated samples were exposed to a second, different amine (step two). For the gradual fine-tuning of the nanosheets using the two-step intercalation strategy, the samples were taken out of the intercalation chamber after a certain duration (between 1 and 25 min) and left to equilibrate under ambient conditions. After the equilibration step of the co-intercalated samples, they are stable over several months, as verified by out-of-plane X-ray powder diffraction (XRPD) measurements.

For the amine replacement, experiments the samples were kept in the intercalation chamber until a non-changing, uniform color was observed. This indicated that the replacement of the first intercalated amine was completed. All conducted two-step amine exchange experiments are given in Tab. S4.1.

Tab. S4.1 Conducted amine intercalation experiments. Intercalation step one is shown vertically while intercalation step two is shown horizontally. A blue X marks the intercalation of a longer amine in the second intercalation step ("upward intercalation"), whereas a green X marks the intercalation of a shorter amine in the second intercalation step ("downward intercalation").

↑ First Intercalation Step						
C12			X	X	X	
C10		X	X	X		
C8	X	X	X		X	X
C6	X	X		X	X	X
C4			X	X	X	
C2		X	X	X		
	C2	C4	C6	C8	C10	C12

→ **Second Intercalation Step**

Characterization

Out-of-plane XRPD patterns of all thin films were recorded at room temperature on a D8-Advance (Bruker) diffractometer working in Bragg-Brentano geometry with Ge(111) monochromated Cu-$K_{\alpha 1}$ radiation (λ = 1.5406 Å). The samples were rotated during the measurement and the scan range was 2 – 80 °2θ (step size: 0.01, time: 2.8 s).

The sample thicknesses and refractive indices (RI) of one- and two-step intercalated thin films were determined with an ellipsometer under ambient conditions (Sopra). Measurements were conducted at three different spots for each sample and the obtained data was fitted using the Cauchy and Lorentz model.

Reflectance measurements were acquired for amine replacement experiments after each intercalation step at two or more spots on two thin films each. After the second intercalation step, the samples were measured at the same spots as after the first step. All measurements were performed at room temperature with a fiber optic spectrometer (Ocean Optics Germany), which was attached to a microscope (Olympus).

The C-H vibrations of the alkylamines intercalated in the thin films were analyzed with a LabRAM single grating spectrometer (HORIBA JobinYvon GmbH) for some of the one- and two-step intercalated samples. The measurements were conducted in quasi-backscattering geometry, using the linearly polarized 632.8 nm (red) line of a He/Ne gas laser.

For the co-intercalated samples containing butylamine and hexylamine contact angle measurements were performed to track the change in polarity.

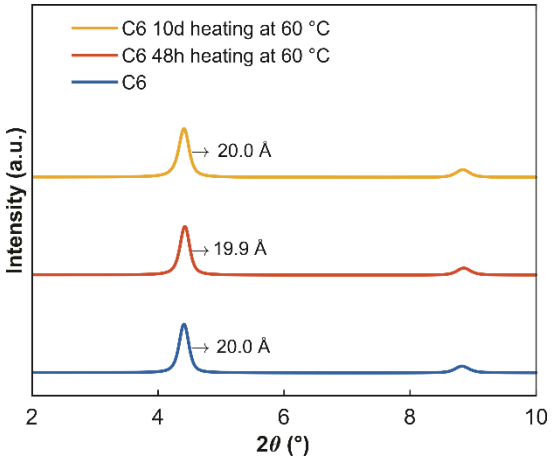

Fig. S4.1 Comparison of a C6 intercalated sample before heating, after heating for 48 h, and after heating for 10 days at 60 °C.

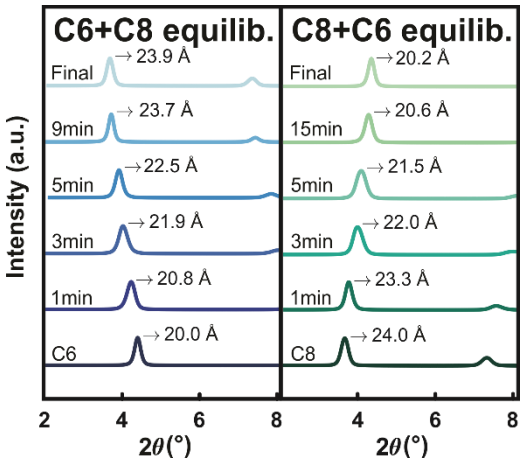

Fig. S4.2 Modification of primary alkylamine intercalated thin films with other primary alkylamines in a second intercalation step. Out-of-plane XRPD patterns (Cu-$K_{\alpha 1}$) at different intercalation times for upward and downward intercalation. Measurements were performed after equilibration under ambient conditions for two weeks. CX + CY corresponds to the amines used during the intercalation process (X = first step, Y = second step).

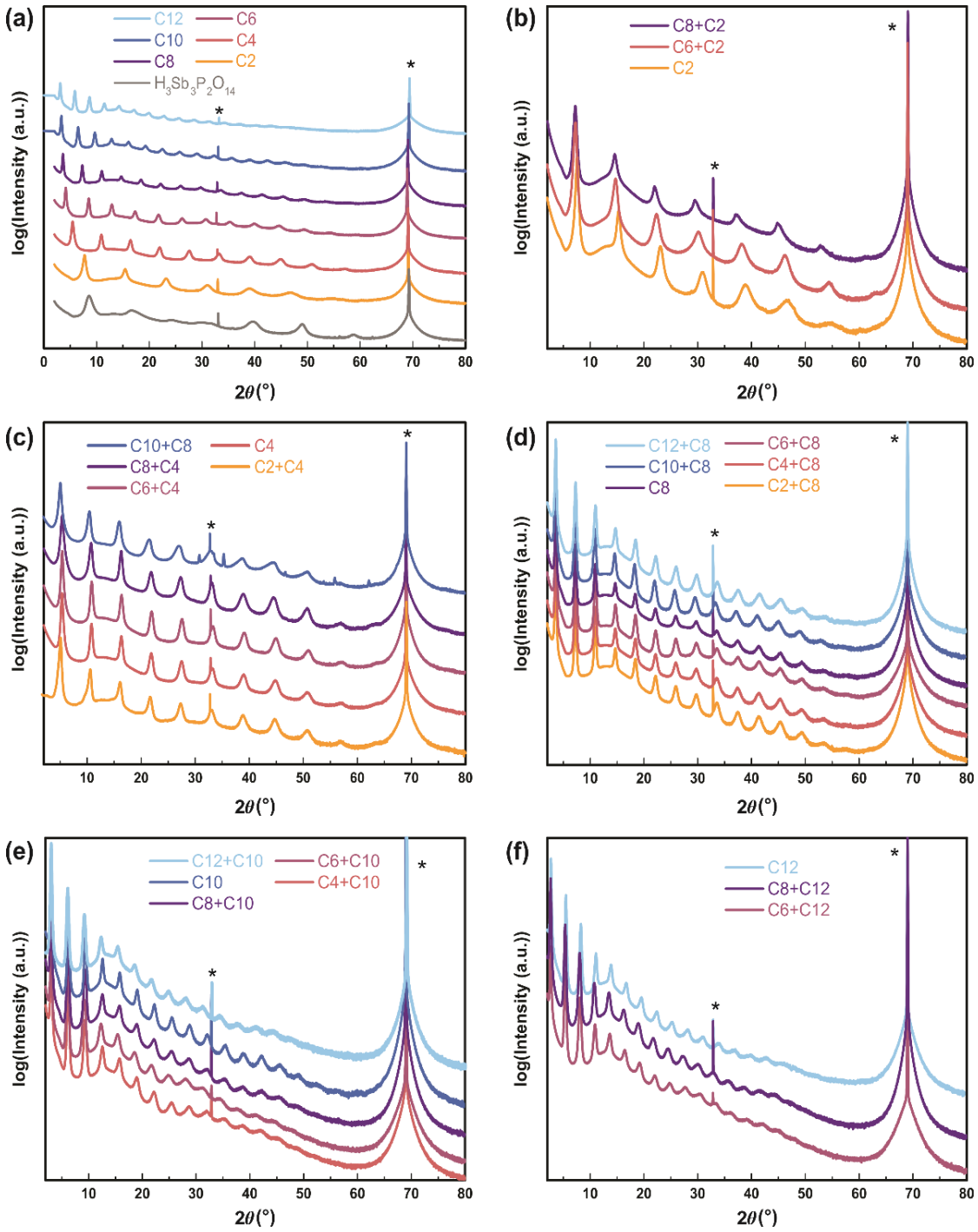

Fig. S4.3 (a) Out-of-plane XRPD patterns (Cu-$K_{\alpha 1}$) of singly intercalated samples plotted with a logarithmic y-axis for better visibility of the reflections. (b) – (f) Comparison of out-of-plane XRPD patterns of samples after first and second intercalation. CX + CY corresponds to the amines used during the intercalation process (X = first step, Y = second step). The reflections at 32.8 and 69.1° 2θ marked with the asterisks can be assigned to the Si-wafer and were utilized for pattern alignment.

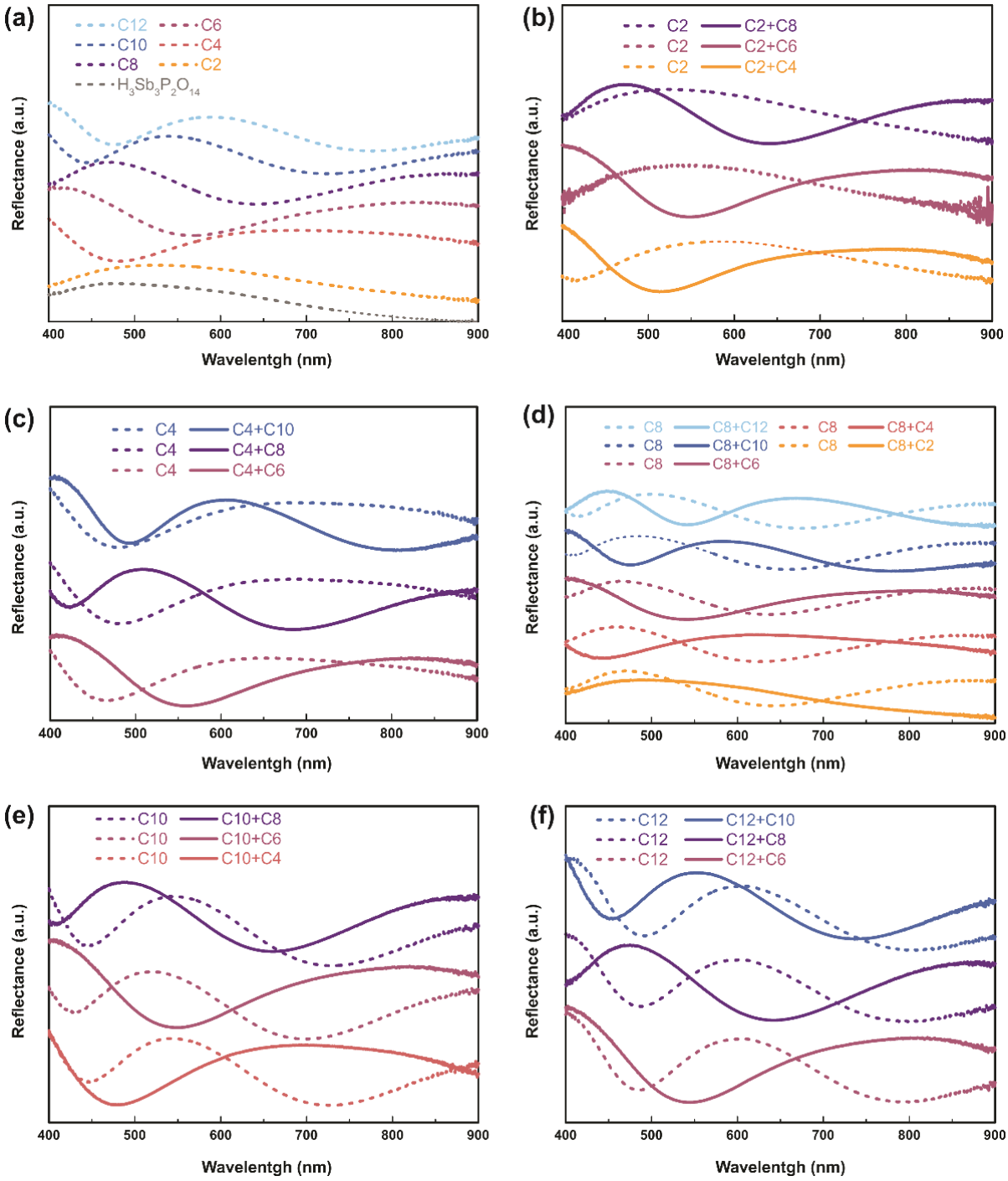

Fig. S4.4 (a) Reflectance spectra of singly intercalated samples. (b) – (f) Reflectance spectra of samples after the first and second intercalation step (dashed and solid graphs respectively) for all conducted series of experiments.

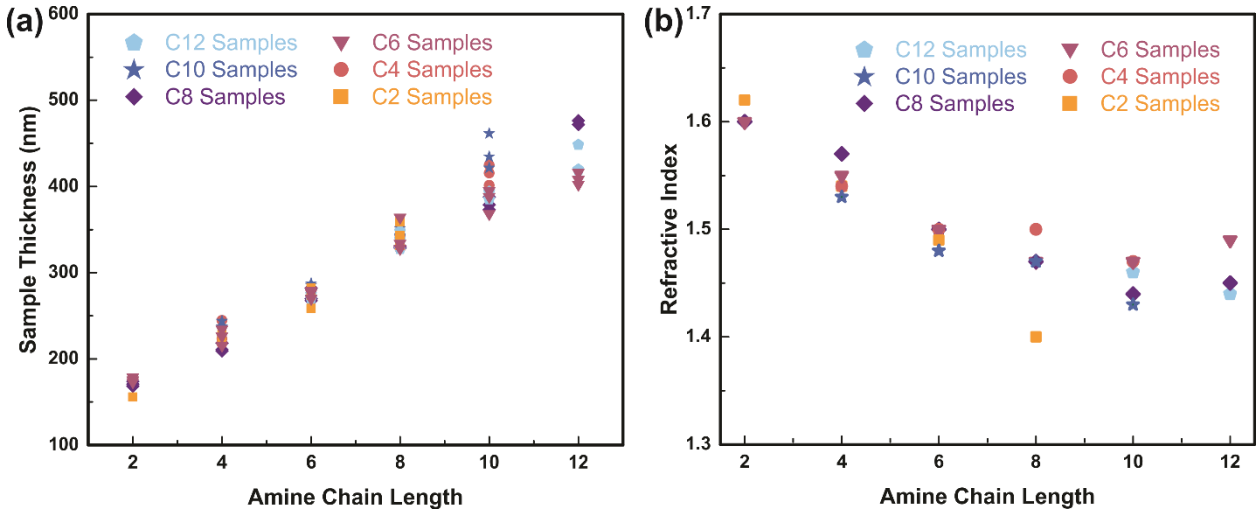

Fig. S4.5 (a) Sample thickness and (b) refractive indices of all prepared amine replacement samples determined with ellipsometry measurements at ambient conditions.

The C2 intercalated samples show a slightly higher RI than the pristine $H_3Sb_3P_2O_{14}$ thin films (1.61 and 1.59 respectively), which could be assigned to the replacement of the water in between the layers. With increased amine chain length a decrease in the effective RI can be observed, which is due to the fact that the amines have a lower RI than the antimony phosphate nanosheets, and with increasing alkyl chain length the amines' contribution to the effective RI grows. However, the RI of the pure amines increases with increased alkyl chain length. Therefore, the decrease of the RI of the amine intercalated samples is not linear.

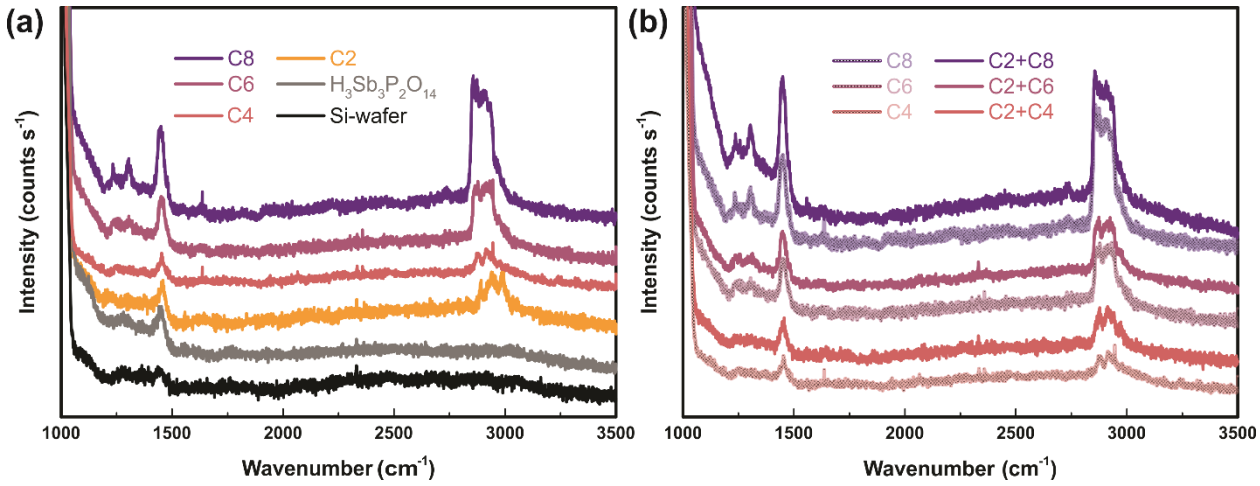

Fig. S4.6 (a) Raman spectra of singly intercalated samples. (b) Comparison of the Raman spectra of singly and doubly amine intercalated samples for replacement experiments.

The results of the singly intercalated samples are given in Fig. S4.6a along with the ones of the pristine Si-wafer and an $H_3Sb_3P_2O_{14}$ thin film as references. Comparing the amine containing samples with the reference, it can be observed that all measurements show a pronounced peak at about 1400 cm^{-1}. Furthermore, the amine intercalated samples exhibit peaks at about 1200, 1300 (both νC-C or δC-H), 2900 and 3000 cm^{-1} (νCH_2 and νCH_3), which are not present in the reference. It can be stated that the peak positions at around 2900 cm^{-1} are shifted to slightly smaller wavenumbers with increasing chain length. This might be due to the fact that the CH_3 stretching vibration appears at higher wavenumbers then the CH_2 stretching vibration and the longer the amine gets the smaller the impact of the CH_3 vibration is. Apart from that, the intensity of these peaks increases for longer amines. Regarding the peaks at around 1200 cm^{-1} it can be observed that they increase with the chain length. A comparison of the Raman spectra of singly (light graphs) and the corresponding doubly (solid graphs) intercalated samples (Fig. S4.6b) shows that they are in good agreement regarding the shape and the position of the peaks (at about 1200, 1300, 2900 and 3000 cm^{-1}), which confirms the replacement of the first intercalated amine.

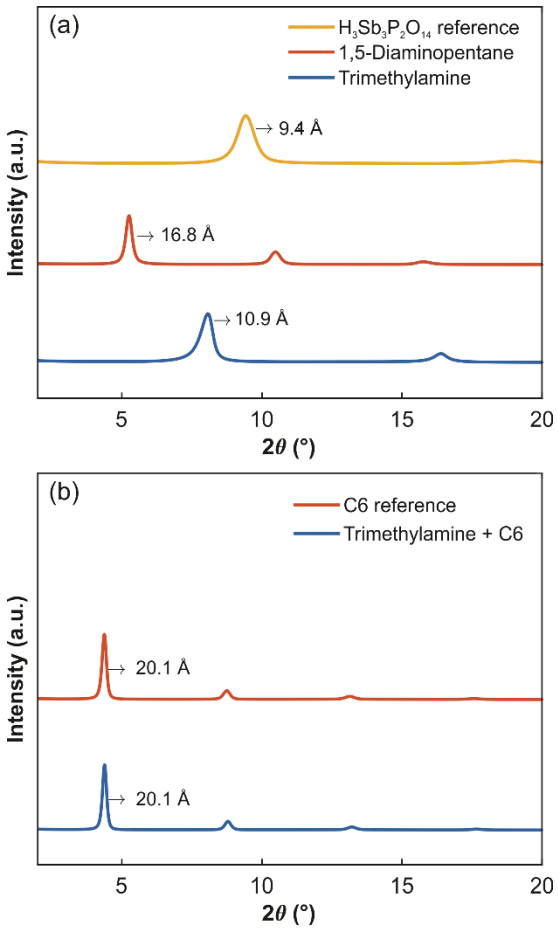

Fig. S4.7 Out-of-plane XRPD patterns (Cu-$K_{\alpha 1}$) of (a) the pristine sample (yellow) along with singly intercalated samples (red: 1,5-diaminopentane; blue: trimethylamine) and (b) the sample in which trimethylamine was exchanged for C6 (blue) along with a C6 singly intercalated sample as reference (red).

The out-of-plane XRPD patterns in Fig. S4.7a indicate that trimethylamine and 1,5-diaminopentane, which are both produced through the microbial spoilage of fish and meat, can be intercalated into the thin films in the same manner as the primary alkylamines. The out-of-plane XRPD pattern of the sample where trimethylamine was exchanged with C6 is given in Fig. S4.7b.

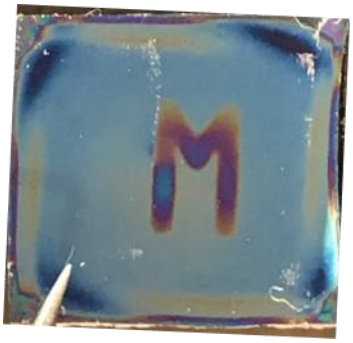

Fig. S4.8 Photograph of an $H_3Sb_3P_2O_{14}$ thin film intercalated with C10 using a mask.

References

1. K. Szendrei, P. Ganter, O. Sànchez-Sobrado, R. Eger, A. Kuhn, B. V. Lotsch, *Adv. Mater.* **2015**, *27*, 6341.
2. P. Ganter, L. M. Schoop, B. V. Lotsch, *Adv. Mater.* **2017**, *29*, 1604884.
3. P. Ganter, L. M. Schoop, M. Däntl, B. V. Lotsch, *Chem. Mater.* **2018**, *30*, 2557.

8.3 Supporting Information for Chapter 5

Transfer of 1D Photonic Crystals *via* spatially resolved Hydrophobization

*Marie Däntl, Susanna Guderley, Katalin Szendrei-Temesi, Dimitra Chatzitheodoridou, Pirmin Ganter, Alberto Jiménez-Solano, and Bettina V. Lotsch**

Experimental Section

Synthesis of Colloidal Suspensions for Spin-coating

Antimony Phosphate Nanosheets

$K_3Sb_3P_2O_{14}$ was synthesized by a solid-state reaction from Sb_2O_3 (Alfa Aesar, 99.6%), KNO_3 (Merck, for analysis) and $NH_4H_2PO_4$ (Acros Organics, >98%) as described previously.[1-5]

To obtain $H_3Sb_3P_2O_{14}$ nanosheets, $K_3Sb_3P_2O_{14}$ was protonated, exfoliated and dried according to the procedure reported elsewhere.[1-5] Subsequently, the obtained nanosheet pellet was re-suspended in a water-ethanol mixture and ultrasonicated.[1-5]

Titanium(IV)-oxide Nanoparticles

TiO_2 nanoparticles were synthesized by a literature procedure.[5,6] While stirring vigorously titanium tetraisopropoxide (TTIP) was added slowly to MilliQ water dropwise. After stirring the suspension for 90 min, it was filtered, washed with MilliQ water and dried. The remaining solid was re-suspended in a mixture of water and nitric acid. Finally, the mixture was heated to 120 °C for 18 h in an autoclave. The resulting suspension contained ca. 15 wt-% TiO_2 nanoparticles. For spin-coating, the colloidal suspension was further diluted to 3 wt-% with methanol. Prior to deposition the suspension was treated with ultrasonication for 30 minutes and filtered (PVDF 0.45 μm) to ensure that large particle agglomerations were removed. Fig. S5.1 shows the size distribution obtained by dynamic light scattering (DLS) measurements.

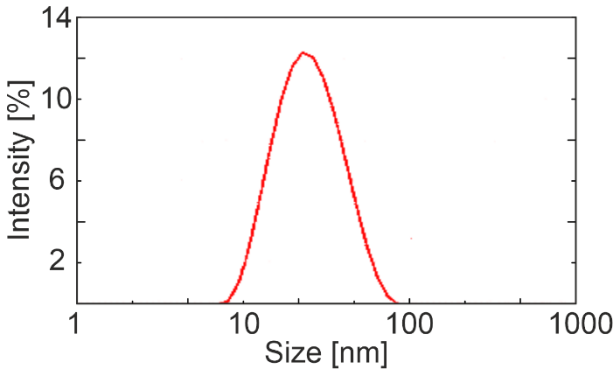

Fig. S5.1 Size distribution of TiO_2 nanoparticles obtained with DLS measurements. A low polydispersity index of 0.15 indicates a narrow particle size distribution. The average particle size was determined to be 25 nm.

Lithium Tin Sulfide Nanosheets

$Li_2Sn_2S_5$ (LTS) was obtained from a solid-state reaction according to a previously reported procedure.[7] The obtained solid was exfoliated, dried and re-suspended in a water-ethanol mixture with subsequent ultrasonication similar to a protocol reported elsewhere.[8]

Bragg Stack Fabrication

To achieve a high refractive index contrast, layers of $H_3Sb_3P_2O_{14}$ nanosheets (H_3) and TiO_2 nanoparticles were deposited alternatingly.[5] The highest optical response is achieved by starting and ending the BS with a TiO_2 layer due to the higher refractive index contrast between TiO_2 and the air/glass. However, the latter cannot be removed from the substrate easily by washing the BS with water. Therefore, the patterning experiment was conducted with a BS that started with a H_3 layer. In order to transfer the BS from one substrate to another, the entire BS had to be imparted with hydrophobicity by exposing the sample to *n*-octylamine (C8; 1M diluted in ethanol) vapor.[5] An LTS layer at the bottom of the BS, which is hydrophilic and can be removed selectively as it is not affected by the C8, acted as a sacrificial layer for the transfer experiments. One and two layers of LTS were proven to be sufficient and the transfer results do not differ. The optimized sequence of layers is summarized in Tab. S5.1. The three above-mentioned colloidal suspensions were spin-coated (WS-650MZ-23NPP, Laurell Technology Corporation) as thin films on glass-wafers (1.5 x 1.5 cm). In each case 150 µL colloidal suspension was spin-coated twice and dried at 90 °C for 10 min. The substrates were cleaned with oxygen plasma for 10 min prior to deposition. Tab. S5.2 gives an overview of the applied spin-coating conditions for each material.

Tab. S5.1 Sequences of layers of BS for different experiment types.

Experiment type	LTS	LTS	H_3	TiO_2	H_3	TiO_2	H_3	TiO_2	H_3	TiO_2	H_3	TiO_2
Patterning and Washing			x	x	x	x	x	x	x	x		
Transfer	x			x	x	x	x	x	x	x	x	x
Pattern transfer	x	x	x	x	x	x	x	x	x	x	x	x
Transfer curved	x	x	x	x	x	x	x	x	x	x		

Tab. S5.2 Colloidal suspensions used for BS fabrication including the corresponding spin-coating conditions and layer thicknesses.

Colloidal suspension	Speed [rpm]	Acceleration [$rpms^{-1}$]	Duration [min]	Thickness [nm]
TiO_2	3000-5000	7000	0.5	80-130
$H_3Sb_3P_2O_{14}$	3500	7000	1.0	35-45
LTS	4000	5000	1.0	20-50

Modification of Hydrophobicity of BSs

To impart the BSs with hydrophobicity for the patterning and transfer experiments they were exposed to C8 (1M in EtOH) vapor for 40 min.[3,4]

BS Transfer from one Substrate to Another

For the transfer of the BS from one substrate to another, samples with LTS as the bottom layer, the one closest to the substrate, were used. The whole sample was intercalated with *n*-octylamine over the vapor phase. Next, the sample was placed in a petri dish with DI water for 2 h to dissolve the LTS layer. By dipping the sample into the water perpendicularly the BS was removed from the substrate and was left swimming on the water surface. Subsequently, it was collected with a new substrate (plain glass or curved glass) and heated on a hotplate at 90 °C for 15 min to improve adhesion to the new substrate and remove residual water from the sample.

BS Patterning and Washing

Patterning of the BS was achieved with a procedure similar to a previously reported one by selectively intercalating parts of the sample without the LTS layer using a mask.[4] Therefore, the sample was attached to the mask with scotch tape and placed onto a glass vial filled with the amine solution in order to expose only a certain part of the sample towards the amine vapor. Subsequently, the mask was removed and the remaining hydrophilic part of the sample was washed away by repeatedly pipetting DI water onto it.

BS Pattern Transfer from one Substrate to Another

For the pattern transfer experiments, the LTS containing sample was intercalated using a mask following the procedure described in Section *BS Patterning and Washing*. The amine-modified BS was immersed in DI water and transferred onto a new glass substrate according to the method used in Section *BS Transfer from one Substrate to Another*.

Modification of Transferred BS *via* Amine Exchange and Heat Treatment

In order to show that the hydrophobicity and thus the sensing capability of the transferred *n*-octylamine intercalated BS can be changed, the sample was exposed to ethylamine (1M in ethanol) vapor for 40 min to exchange the *n*-octylamine with ethylamine. For elongated exposure times no change in the position of the Bragg peak was observed anymore and the exchange was assumed to be complete. This process was adapted from a method, which has been applied for flexible, post-synthetic exchange of primary alkylamines in $H_3Sb_3P_2O_{14}$-based thin films.[4] Furthermore, the ethylamine intercalated sample was re-modified by exposure of the sample to *n*-octylamine vapor for 40 min. Lastly, an ethylamine intercalated sample was kept at 70 °C for 24 h in order to remove the amines and thus regenerate the pristine sample.

Characterization

Water Contact Angle Measurements

Contact angle measurements were acquired for thin films of the pristine materials and the BS as well as the C8 intercalated counterparts under ambient conditions to analyze the hydrophobicity of the sample surface.

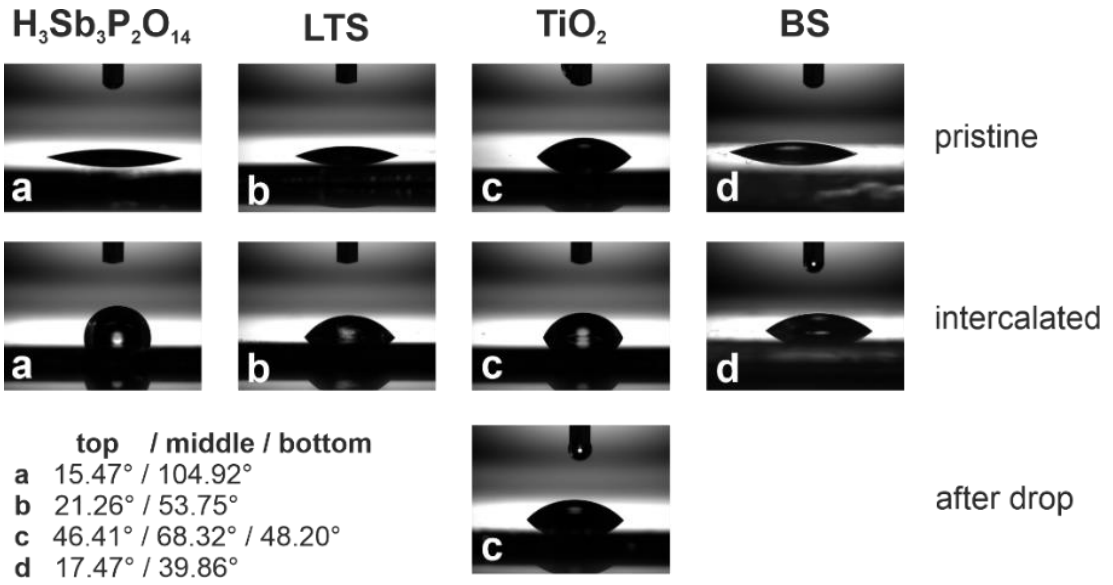

Fig. S5.2 Comparison of the photographs of water contact angle measurements of pristine and amine intercalated thin films of $H_3Sb_3P_2O_{14}$, LTS and TiO_2 as well as the pristine and intercalated BS along with the corresponding calculated angles. Note that the calculated contact angles are given below the photographs. In general, the exposure to amines leads to an increase in hydrophobicity, while only the $H_3Sb_3P_2O_{14}$ thin film turns completely hydrophobic. For TiO_2 a second measurement was performed that showed that the amines seem to be washed out by the water during the measurement. This is also the case for LTS during the transfer process.

XRPD Measurements

Out-of-plane XRPD patterns of the thin films with two layers of either H_3, LTS or TiO_2 were recorded on a D8-Advance (Bruker) diffractometer working in Bragg-Brentano geometry with Ge(111) monochromated Cu-$K_{\alpha 1}$ radiation (λ = 1.5406 Å). The samples were measured under ambient conditions and were rotated during the measurement. All diffraction patterns were recorded over the scan range of 2 – 80° 2θ (step size: 0.01, time: 2.8 s).

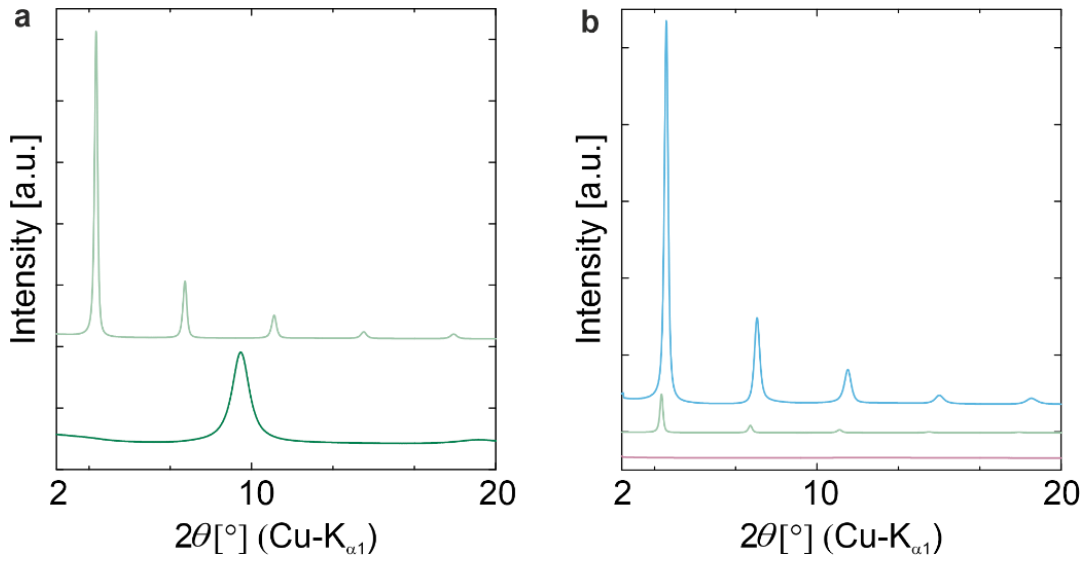

Fig. S5.3 (a) Comparison of diffraction patterns of a pristine $H_3Sb_3P_2O_{14}$ thin film (dark green, bottom) with an octylamine intercalated one (mint, top). The stacking reflection of $H_3Sb_3P_2O_{14}$ is shifted towards smaller 2θ values due to intercalation of the amines. (b) Comparison of diffraction patterns of an amine intercalated $H_3Sb_3P_2O_{14}4$ thin film (mint, middle) with the patterns of an amine intercalated Bragg stack (blue, top) and a TiO_2 thin film, which was exposed to octylamine (rose, bottom).Since the TiO_2 thin film does not show reflections in the recorded range, it is clear that this material does not influence or change the diffraction pattern of the BS. The reflections of the Bragg stack appear at the same 2θ values as the ones of the intercalated $H_3Sb_3P_2O_{14}$ thin film but exhibit much higher intensity as there is more material in the sample.

Reflectance Measurements

All BSs were analyzed with reflectance measurements using a fiber optic spectrophotometer (Ocean Optics Germany) attached to a microscope (Olympus). Additionally, the measurements were acquired for the intercalated/patterned samples as well as the transferred BSs. All measurements were performed at room temperature.

Sensing experiments

Sensing experiments were performed with a home-built chamber that can be mounted to the microscope. All measurements were acquired at room temperature. Exposure of the 1DPC towards vapors leads to thickness and refractive index changes in the sample (if the material-based sensor is responsive to the stimuli), which leads to a shift of the Bragg peak towards larger wavelengths. The normalized shifts (optical response) of the Bragg peak of a pristine BS, a transferred *n*-octylamine intercalated BS, a transferred ethylamine intercalated BS and a regenerated transferred BS upon exposure to ethanol are given in Fig. S5.4.

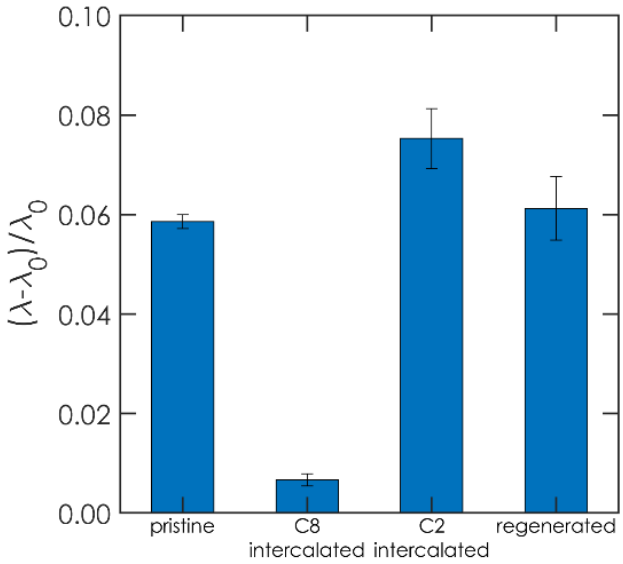

Fig. S5.4 Comparison of the normalized shift of the Bragg peak upon exposure to ethanol of a pristine sample, a transferred n-octylamine intercalated BS, a transferred ethylamine intercalated BS and a regenerated transferred BS.

By intercalating the sample with amines we alter the sensitivity towards vapors because the hydrophobicity is changed but nonetheless sensing is still possible. Upon ethylamine intercalation the response towards ethanol is increased because this sample is most compatible in polarity with the solvent vapor. The non-intercalated sample is too hydrophilic while the *n*-octylamine intercalated one is too hydrophobic to exhibit a large response. The comparison of the response of the regenerated transferred sample with the response of the pristine sample shows that the initial sensitivity towards ethanol is restored.

Scanning Electron Microscopy

Cross section images of a pristine BS, an *n*-octylamine intercalated BS and a transferred, regenerated BS were recorded on a scanning electron microscope (FE-SEM; Zeiss, Merlin) working with 1.5 kV collecting both secondary (In-lens detector) and backscattered electrons (EsB detector).

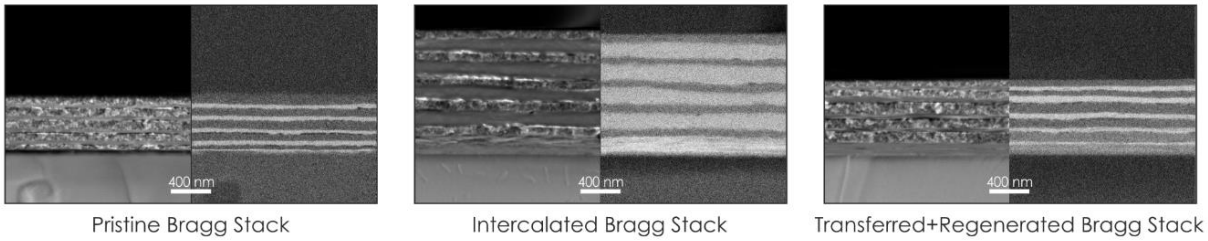

Fig. S5.5 SEM cross section images of three different samples. A pristine BS (left), a C8 intercalated BS (middle), and a transferred, regenerated BS (right).

In general, the multilayer structure is maintained throughout the different processes (intercalation, transfer and regeneration). Additionally, continuous and smooth interfaces between the different constituent layers can be seen. Please note that three different samples were used for this study due to the invasive preparation of the sample for obtaining SEM cross section images. Therefore, there may be slight thickness differences in the constituent layers in each image.

BS Transfer to Metal Substrate

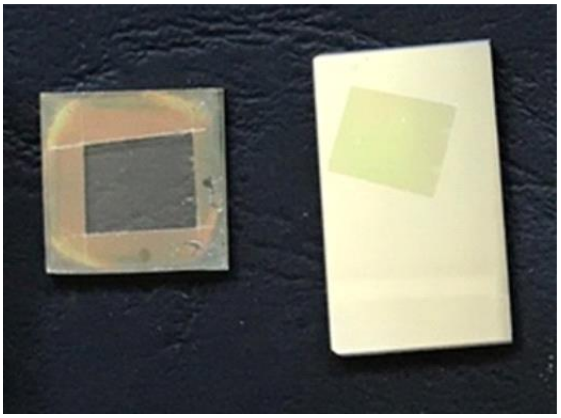

Fig. S5.6 Transfer of an *n*-octylamine intercalated BS from a glass substrate to an aluminum coated glass slide.

Regeneration of Pristine Bragg Stack

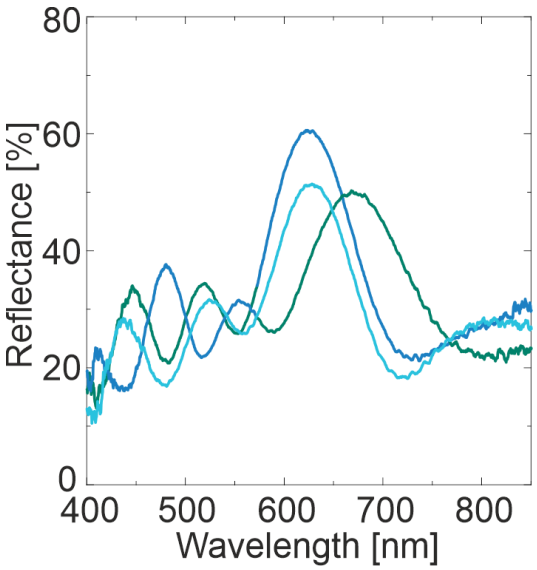

Fig. S5.7 Regeneration of a pristine sample through heat treatment (70 °C for 24 h) after ethylamine intercalation. The reflectance of the pristine sample (dark blue) is red-shifted upon ethylamine intercalation (green). After the heat treatment, the Bragg peak (light blue) appears at the same wavelength as for the pristine sample, which indicates that ethylamine was removed and the pristine sample was regenerated.

Lateral Diffusion in Patterning Experiments

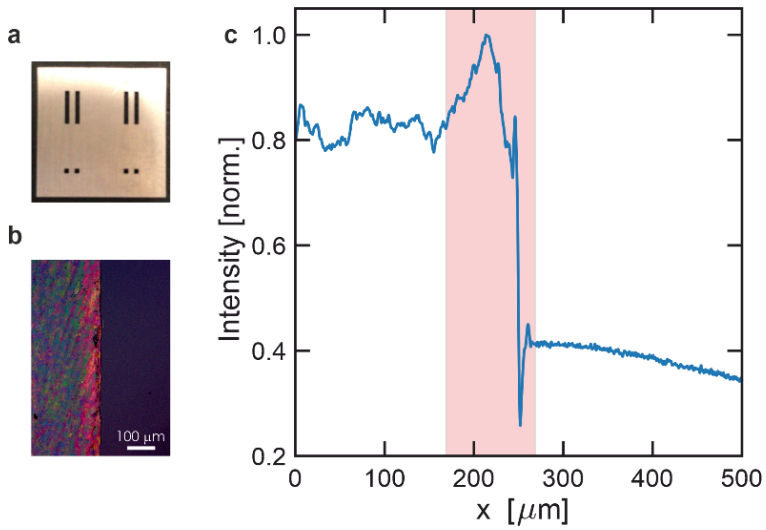

Fig. S5.8 Characterization of the lateral resolution (line edge roughness) of the patterning method. (a) Mask used for the lateral resolution study, the grooves have a width of 1 mm. (b) Digital photograph of the edge of the structure after the patterning process (amine intercalation and structure washing). (c) Average height profile along the edge shown in b. The shaded box has a width of 100 µm.

Calculations of Reflectance

The calculations of the reflectance (dashed lines in Fig. 5.1 of the manuscript) were obtained similar to a previously reported approach applying the transfer matrix method (TMM).[5] More specifically the modeling process simultaneously fits three reflectance spectra of the same sample, pristine ($\mathrm{R_p}(\lambda)$), intercalated ($\mathrm{R_i}(\lambda)$) and transferred multilayer ($\mathrm{R_t}(\lambda)$), minimizing the difference between the theoretical and experimental reflectance spectra:

$$\sum_{\lambda}\left(\mathrm{R_{p_{exp}}}(\lambda)-\mathrm{R_{p_{theo}}}(\lambda)\right)^2+\sum_{\lambda}\left(\mathrm{R_{i_{exp}}}(\lambda)-\mathrm{R_{i_{theo}}}(\lambda)\right)^2$$

$$+\sum_{\lambda}\left(\mathrm{R_{t_{exp}}}(\lambda)-\mathrm{R_{t_{theo}}}(\lambda)\right)^2$$

First, to fit $\mathrm{R_p}(\lambda)$, we assume a perfect periodic system (TiO_2/H_3, with thicknesses $d_{\mathrm{TiO_2}}$ and $d_{\mathrm{H_3}}$ respectively) on top of an LTS layer with thickness d_{LTS} deposited on a glass substrate. The TiO_2 layers show a porosity of $p_{\mathrm{TiO_2}}$. Second, the $\mathrm{R_i}(\lambda)$ fitting starts from the previous structure assuming an increase in the thickness of the H_3 layers (identical for all of them, $\Delta_{\mathrm{H_3}}$). This growth implies an increase in the porosity, which translates into a change in the refractive index perceivable by a redshift of the optical response.[5] Third, the LTS layer is removed from the model and finally fitting $\mathrm{R_t}(\lambda)$. In summary, this model assumes five fitting parameters for each set of three reflectance spectra. The refractive index of the TiO_2, H_3 and LTS were taken from literature.[5,8,9] The porosity of the layers was modelled with the Burggeman model for the TiO_2 case, while the H_3 layers were modelled using the volumetric average.[10]

References

1. K. Szendrei, P. Ganter, O. Sànchez-Sobrado, R. Eger, A. Kuhn, B. V. Lotsch, *Adv. Mater.* **2015**, *27*, 6341.
2. P. Ganter, L. M. Schoop, B. V. Lotsch, *Adv. Mater.* **2017**, *29*, 1604884.
3. P. Ganter, L. M. Schoop, M. Däntl, B. V. Lotsch, *Chem. Mater.* **2018**, *30*, 2557.
4. M. Däntl, P. Ganter, K. Szendrei-Temesi, A. Jiménez-Solano, B. V. Lotsch, *Nanoscale Horiz.* **2020**, *5*, 74.
5. K. Szendrei-Temesi, A. Jiménez-Solano, B. V. Lotsch, *Adv. Mater.* **2018**, *30*, 6289.
6. Y. Li, M. E. Calvo, H. Míguez, *Adv. Opt. Mater.* **2016**, *4*, 464.

7. A. Kuhn, T. Holzmann, J. Nuss, B. V. Lotsch, *J. Mater. Chem. A* **2014**, *2*, 6100.

8. K. Szendrei-Temesi, O. Sanchez-Sobrado, S. B. Betzler, K. M. Durner, T. Holzmann, B. V. Lotsch, *Adv. Funct. Mater.* **2018**, *28*, 1705740.

9. A. Jiménez-Solano, M. Anaya, M. E. Calvo, M. Alcon-Camas, C. Alcañiz, E. Guillén, N. Martínez, M. Gallas, T. Preussner, R. Escobar-Galindo, H. Míguez, *Adv. Opt. Mater.* **2017**, *5*, 1600833.

10. N. Nagy, A. Deák, Z. Hórvölgyi, M. Fried, A. Agod, I. Bársony, *Langmuir* **2006**, *22*, 8416.

8.4 Supporting Information for Chapter 6

Protocol for the Analysis of Real-Time XRD Data of Intercalation Processes in Thin Films Demonstrated for Amine Intercalation in $H_3Sb_3P_2O_{14}$ Thin Films

Marie Däntl, Johannes Maschita, Peter Wochner, Alberto Jiménez-Solano, Hugo A. Vignolo-González, D. Putzky, Robert E. Dinnebier, Sebastian Bette, Bettina V. Lotsch**

Experimental Section

Nanosheet Synthesis and Sample Fabrication

$K_3Sb_3P_2O_{14}$ was synthesized following a procedure described elsewhere from $NH_4H_2PO_4$ (Acros Organics, >98%), KNO_3 (Merck, for analysis), and Sb_2O_3 (Alfa Aesar, 99.6%).[1-3]

Subsequently, $K_3Sb_3P_2O_{14}$ was protonated, exfoliated and dried according to literature.[1-3]

The obtained powder was dissolved (34 mmol/L) in a water-ethanol (40:60 vol-%) mixture, ultrasonicated and spin-coated (WS-650MZ-23NPP, Laurell Technology Corporation) as thin films on Si-wafers (1.5 x 1.5 cm, 110 orientation).[1-3] The Si-wafers were cleaned with oxygen plasma for 10 min prior to deposition of the thin film. Spin-coating was conducted twice for each wafer with 200 µL of the colloidal suspension for 1.5 min (Speed: 2000 rpm, acceleration: 10000 rpm).

In situ X-ray Diffraction Measurements

In previous work we have shown that primary alkylamines can be intercalated in layered $H_3Sb_3P_2O_{14}$ thin films over the vapor phase, leading to a clear change of the interlayer distance.[3,4] In order to gain a better understanding of the intercalation, we applied *in situ* X-ray diffraction to determine the intercalation mechanism of ethylamine (C4) in $H_3Sb_3P_2O_{14}$ thin films. The measurements were carried out at the synchrotron beamline MPI at the light source ANKA of the Karlsruhe Institute of Technology under constant He-flow. The diffractometer was operated in six-circle geometry, the wavelength was λ = 1.2398 Å, and a 1D detector (Dectris Mythen; 1280 channels) covering the range of 2 – 12° 2θ was applied. Diffraction patterns probed in focused beam geometry with a focal spot of ~ 0.25 mm normal and ~ 0.35 mm parallel to the sample surface exhibit only 00*l* reflections due to the preferred orientation of the nanosheets parallel to the substrate.[5] Therefore, the observed reflection corresponds to the basal plane, i.e. the mean interlayer distance between the nanosheets. Scans were taken continuously approximately every second to closely monitor the intercalation

process. During the intercalation of C4 (1 mL, 3M, diluted in ethanol (EtOH)) in between the layers of $H_3Sb_3P_2O_{14}$, the interlayer distance is enlarged and therefore the intercalation can be followed by analyzing the shift of the diffraction peak.[3,4] Note that the C4 was diluted in EtOH to avoid condensation of the amine in the measurement chamber and on the Kapton dome and therefore interference with the measurement. The intercalation was considered to be complete as soon as the diffraction peak did not change its position and intensity anymore. However, due to the large amount of data, only the most important and characteristic 20 measurements were fitted for detailed analysis.

The chamber used for the measurements (see Fig. S6.1) was custom-built and consisted of an in- and outlet for He-gas, a height adjustable table to mount the sample, a valve for the injection of the amine solution with the aid of a syringe, a reservoir for the injected solution, and a Kapton dome.

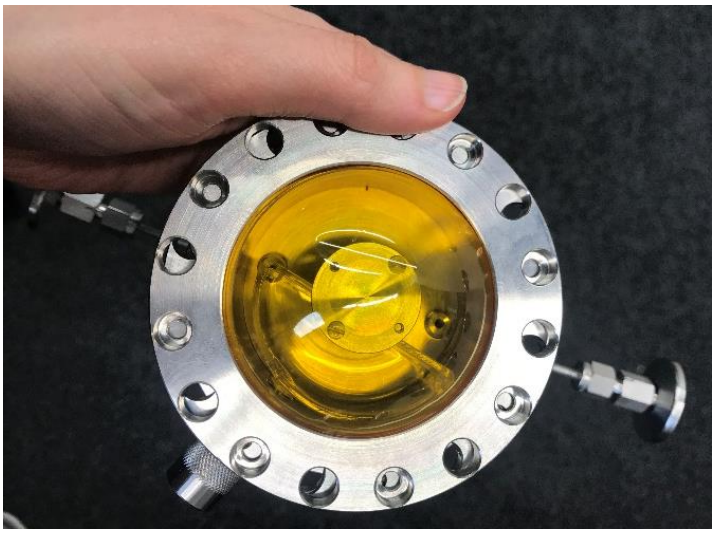

Fig. S6.1 Photograph of the homebuilt measurement chamber.

The syringe was operated with a small motor that could be operated remotely from outside the measurement hutch. Note that the amine solution was injected in the chamber into the reservoir next to the sample holder after alignment of the sample and after the first ten scans were measured. At the end of the measurement, there was still a residue of the amine solution in the container, so that continuous evaporation could be ensured throughout the experiment.

Data Analysis

The program TOPAS 6.0[6] was used to analyze and refine the X-ray diffraction (XRD) data. The random intercalation of molecules in-between the layers was modeled by a recursive

supercell approach[7,8] that creates supercells based on stacking vectors and transition probabilities using a large number of layers and subsequently averages the diffraction effects of many of these supercells. For all refinements, 300 supercells consisting of 100 layers were averaged. As the XRD data only contained reflections related to lattice planes perpendicular to the stacking direction, they are not sensitive to the layer constitution. Hence, we decided to model each layer by one antimony atom. In consequence, the only quantitative information that can be derived from the diffraction data is the distribution of different interlayer distances. Note that the substrate peak was removed from the graphs in the main text and ESI in order to ensure readability of the graphs.

Additional Figures and Tables

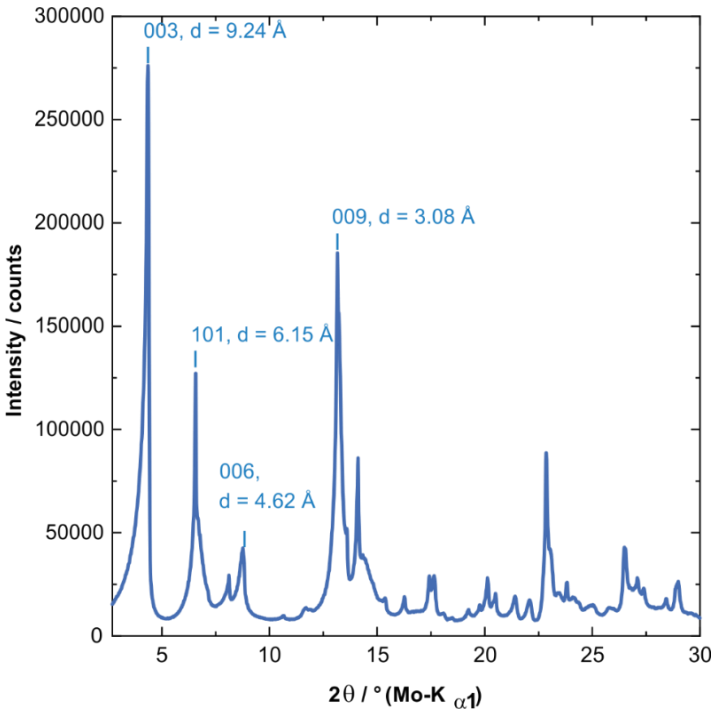

Fig. S6.2 XRPD pattern of $H_3Sb_3P_2O_{14}$ bulk powder including selected reflection indices and related *d*-spacings derived from the trigonal unit cell of the structural analogue $K_3Sb_2P_3O_{14}$.[9]

The X-ray powder diffraction (XRPD) pattern of bulk $H_3Sb_3P_2O_{14}$ shows 00*l* basal reflections corresponding to an interlayer distance of 9.24 Å (Fig. S6.2) and resembles strong similarities to the pattern of $K_3Sb_3P_2O_{14}$.[9] Hence it can be concluded that both compounds exhibit very similar crystal structures. Strong anisotropic peak broadening, visible as triangular peak shapes (Fig. S6.2) indicates strong structural disorder in form of stacking faults in the bulk $H_3Sb_3P_2O_{14}$, which prevents a detailed structural characterization.

Tab. S6.1 Overview on the transition matrices used for describing the faulting scenarios shown in Fig. 6.2 with h1, h2, h3, and h4 being the related interlayer distances and P_{EtOH}, P_{C4}, $P_{C4+EtOH}$ the related fault probabilities.

Faulting Scenario I			
from↓ to→	**Empty-interlayer**	**EtOH-interlayer**	
Empty-interlayer	1-P_{EtOH}, h1	P_{EtOH}, h1	
EtOH-interlayer	1-P_{EtOH}, h2	P_{EtOH}, h2	
Faulting Scenario II			
from↓ to→	**EtOH-interlayer**	**C4-interlayer**	**C4+EtOH-interlayer**
EtOH-interlayer	1-P_{C4}-$P_{C4+EtOH}$, h2	P_{C4}, h2	$P_{C4+EtOH}$, h2
C4-interlayer	1-P_{C4}-$P_{C4+EtOH}$, h3	P_{C4}, h3	$P_{C4+EtOH}$, h3
C4+EtOH-interlayer	1-P_{C4}-$P_{C4+EtOH}$, h4	P_{C4}, h4	$P_{C4+EtOH}$, h4
Interlayer Distances			
Parameter	**Distance/ Å**	**Derived from**	
h1	9.24	XRPD of pristine $H_3Sb_3P_2O_{14}$ powder (Fig. S6.1)	
h2	11.51	2D-grid search optimization of initial XRD data (Fig. 6.3))	
h3	17.72	2D-grid search optimization of final XRD data	
h4	19.99	calculated as: h4 = h3 + (h2 – h1)	

Tab. S6.2 Phase fractions and fault probabilities extracted from Rietveld refinements shown in Fig. 6.4.

Graph	**(a)**	**(b)**	**(c)**
Time Pattern was measured [s]	1	75	826
Phase fraction non-C4-int. [wt-%]	100	66.6	0
Phase fraction C4-int. [wt-%]	0	33.4	100
Fault probability P_{EtOH}	0.390	0.530	-
Fault probability $P_{C4+EtOH}$	-	0.210	0.037
Fault probability P_{C4}	-	0.687	0.925
R-wp [%]	6.9	4.4	7.0

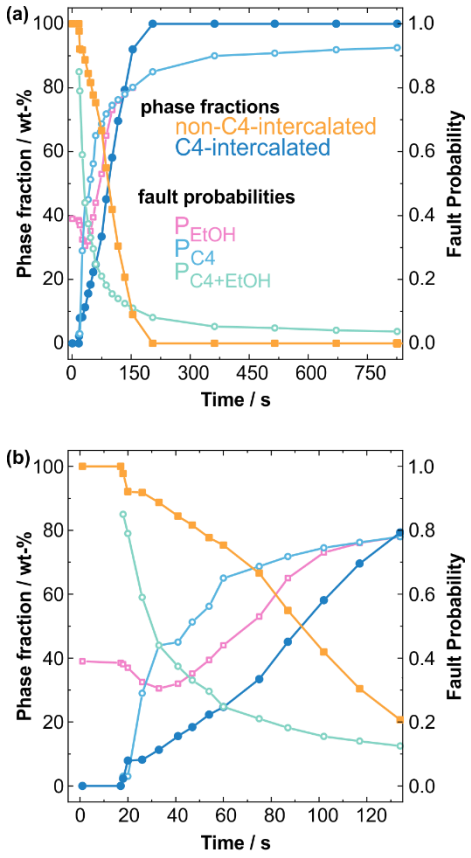

Fig. S6.3 Evolution of the phase fractions (closed symbols) and the fault probabilities (open symbols) of the C4- (circles) and non-C4-intercalated (squares) phases over the entire reaction (a) and during the initial stage of the reaction (b).

The refinement of the recorded XRD patterns enabled us to monitor the evolution of the phase fractions (Fig. S6.3, closed symbols) and the fault probabilities (open symbols) during the amine intercalation process. Note that the amine solution was injected after the first 10 seconds of the measurement. Significant amounts (> 5 wt-%) of the C4-intercalated phase (Fig. S6.3, filled blue circles) appear 20 s after the start of the intercalation experiment (10 s after amine injection). Then the amount of this phase rapidly increases until it reaches 100% 205 s after the start of the experiment (195 s after amine injection). The non-C4-intercalated phase initially exhibits an ethanol interstratification probability (P_{EtOH}) of 0.39, meaning that on average almost 2 out of 5 layers show an ethanol intercalation. During the initial stage of the reaction, this fault probability decreases until it reaches a minimum of P_{EtOH} = 0.305 (Fig. S6.3, open pink squares) 33 s after the start of the experiment (23 s after amine injection). Subsequently P_{EtOH} strongly increases up to 0.80 after 154 s (144 s after amine injection) when the non-C4-intercalated phase starts to disappear (Fig. S6.3, filled orange squares). The microstructure of the C4-intercalated phase is governed by interstratification of both amine and ethanol in-between the layers, with the fault probability $P_{C4+EtOH}$ being 0.85 (Fig. S6.3,

open green circles) 18 s after the start of the experiment (8 s after amine injection). As the reaction proceeds this fault probability strongly decreases, whereas the probability of pure amine intercalation, P_{C4} (Fig. S6.3, open blue circles), increases. At the end of the monitoring, 826 s after the start of the experiment (816 s after amine injection), P_{C4}, is neither constant nor reaches 1.0.

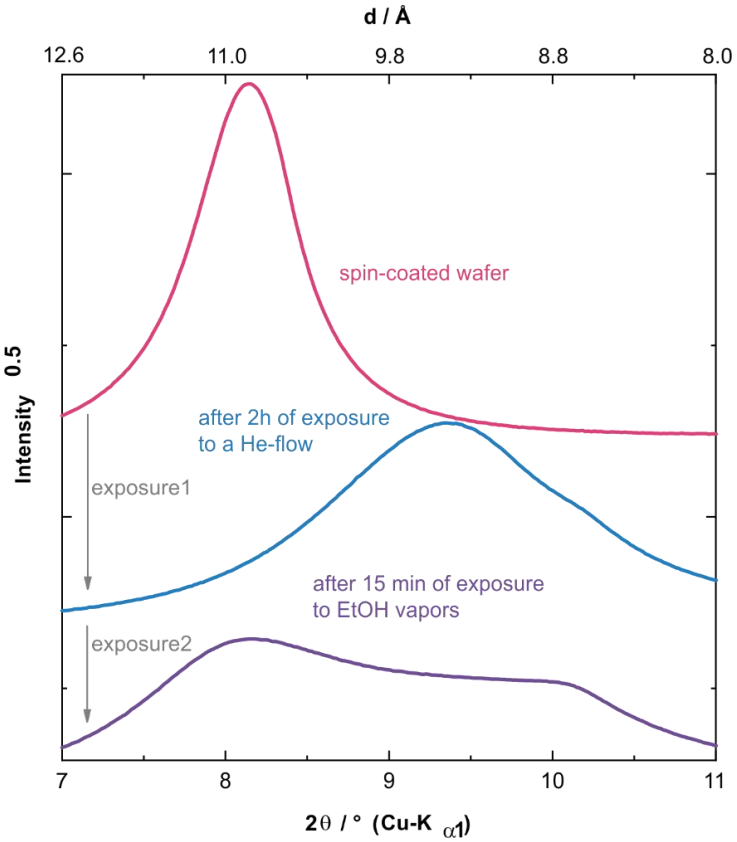

Fig. S6.4 *Ex-situ* XRD patterns of a spin-coated $H_3Sb_3P_2O_{14}$ thin film (black pattern), that was subsequently exposed to a He-gas flow for 2 hours to remove the intercalated ethanol (red pattern) and afterwards exposed to ethanol vapor (blue pattern) in order to re-intercalate the alcohol.

Tab. S6.3 Processes occurring during the competing intercalation processes of amine and ethanol in-between $H_3Sb_3P_2O_{14}$-layers of a spin-coated thin film and proposed reaction mechanism.

Processes Occurring during the Intercalation Experiment		
No.	**Process**	**Reaction**
[I]	Evaporation of ethanol	$CH_3CH_2OH_{(l)} \rightarrow CH_3CH_2OH_{(g)}$
[II]	Evaporation of C4	$C4_{(l)} \rightarrow C4_{(g)}$
[III]	De-intercalation of ethanol	$H_3Sb_3P_2O_{14} \cdot n(CH_3CH_2OH)_{(s)} \rightarrow H_3Sb_3P_2O_{14(s)} + n(CH_3CH_2OH)_{(g)}$
[IV]	Intercalation of ethanol	$H_3Sb_3P_2O_{14(s)} + n(CH_3CH_2OH)_{(g)} \rightarrow H_3Sb_3P_2O_{14} \cdot n(CH_3CH_2OH)_{(s)}$
[V]	Intercalation of C4	$H_3Sb_3P_2O_{14(s)} + mC4_{(g)} \rightarrow H_3Sb_3P_2O_{14} \cdot mC4_{(s)}$
Proposed Reaction Sequence during the Intercalation Experiment		
Step	**Processes**	**Reaction**
1	Ethanol saturation of the gas phase	$CH_3CH_2OH_{(l)} \rightarrow CH_3CH_2OH_{(g)}$ [I] $H_3Sb_3P_2O_{14} \cdot n(CH_3CH_2OH)_{(s)} \rightarrow H_3Sb_3P_2O_{14(s)} + n(CH_3CH_2OH)_{(g)}$ [III]
2a	Intercalation of ethanol	$H_3Sb_3P_2O_{14(s)} + n(CH_3CH_2OH)_{(g)} \rightarrow H_3Sb_3P_2O_{14} \cdot n(CH_3CH_2OH)_{(s)}$ [IV]
2b	Intercalation of C4 in EtOH intercalated layers	$H_3Sb_3P_2O_{14} \cdot n(CH_3CH_2OH)_{(s)} + mC4_{(g)} \rightarrow$ $H_3Sb_3P_2O_{14} \cdot n(CH_3CH_2OH) \cdot mC4_{(s)}$ [V]
3	Extrusion of intercalated EtOH	$H_3Sb_3P_2O_{14} \cdot n(CH_3CH_2OH) \cdot mC4_{(s)} \rightarrow$ $H_3Sb_3P_2O_{14} \cdot mC4_{(s)} + n(CH_3CH_2OH)_{(g)}$ [III]

References

1. K. Szendrei, P. Ganter, O. Sànchez-Sobrado, R. Eger, A. Kuhn, B. V. Lotsch, *Adv. Mater.* **2015**, *27*, 6341.
2. P. Ganter, L. M. Schoop, B. V. Lotsch, *Adv. Mater.* **2017**, *29*, 1604884.
3. P. Ganter, L. M. Schoop, M. Däntl, B. V. Lotsch, *Chem. Mater.* **2018**, *30*, 2557.
4. M. Däntl, P. Ganter, K. Szendrei-Temesi, A. Jiménez-Solano, B. V. Lotsch, *Nanoscale Horiz.* **2020**, *5*, 74.
5. P. Ganter, K. Szendrei, B. V. Lotsch, *Adv. Mater.* **2016**, *28*, 7436.
6. A. A. Coelho, *J. Appl. Crystallogr.* **2018**, *51*, 210.
7. C. M. Ainsworth, J. W. Lewis, C.-H. Wang, A. A. Coelho, H. E. Johnston, H. E. A. Brand, J. S. O. Evans, *Chem. Mater.* **2016**, *28*, 3184.
8. A. A. Coelho, J. S. O. Evans, J. W. Lewis, *J. Appl. Crystallogr.* **2016**, *49*, 1740.
9. Y. Piffard, A. Lachgar, M. Tournoux, *J. Solid State Chem.* **1985**, *58*, 253.

8.5 List of Publications

Published as part of this thesis:

Protocol for the Analysis of Real-Time XRD Data of Intercalation Processes in Thin Films Demonstrated for Amine Intercalation in $H_3Sb_3P_2O_{14}$ Thin Films

M. Däntl, J. Maschita, P. Wochner, A. Jiménez-Solano, H. A. Vignolo-González, D. Putzky, R. E. Dinnebier, S. Bette, B. V. Lotsch, *Chem. Mater.* **2022**, submitted.

Stimuli-Responsive One-Dimensional Photonic Crystals: Design, Fabrication and Sensing

M. Däntl, A. Jiménez-Solano, B. V. Lotsch, *Mater. Adv.* **2022**, Advance Article.

Customizing $H_3Sb_3P_2O_{14}$ Nanosheet Sensors by Reversible Vapor-phase Amine Intercalation

M. Däntl, P. Ganter, K. Szendrei-Temesi, A. Jiménez-Solano, B. V. Lotsch, *Nanoscale Horiz.* **2020**, *5*, 74.

Transfer of 1D Photonic Crystals via Spatially Resolved Hydrophobization

M. Däntl, S. Guderley, K. Szendrei-Temesi, D. Chatzitheodoridou, P. Ganter, A. Jiménez-Solano, *Small* **2021**, *17*, 2007864.

Not part of this thesis:

Vapor-Phase Amine Intercalation for the Rational Design of Photonic Nanosheet Sensors

P. Ganter, L. M. Schoop, M. Däntl, B. V. Lotsch, *Chem. Mater.* **2018**, *30*, 2557.

8.6 Contribution to Conferences

ISRS (poster presentation)

M. Däntl, P. Ganter, L. M. Schoop, B. V. Lotsch, Vapor-Phase Amine Intercalation for the Rational Design of Photonic Nanosheet Sensor, Bayreuth **2018**.

STOE User Meeting (participation)

Darmstadt **2018**.

Hemdsärmelkolloqium (participation)

Kiel **2019**.

CeNS Summer Retreat (flash talk and poster presentation)

M. Däntl, P. Ganter, K. Szendrei-Temesi, A. Jiménez-Solano, B. V. Lotsch, Customizing Nanosheet-based Fabry-Pérot Sensors by Interlayer Modification, Venice **2019**.

CeNS Winter Retreat (flash talk and poster presentation)

M. Däntl, P. Ganter, K. Szendrei-Temesi, A. Jiménez-Solano, B. V. Lotsch, Customizing Nanosheet-based Fabry-Pérot Sensors by Interlayer Modification, Hirschegg **2022**.

“Experience is what you get when you didn't get what you wanted. And experience is often the most valuable thing you have to offer.”

— Randy Pausch